DISTRIBUTED TIME-CONSTANT IMPEDANCE RESPONSES INTERPRETED IN TERMS OF PHYSICALLY MEANINGFUL PROPERTIES

By

BRYAN D. HIRSCHORN

A DISSERTATION PRESENTED TO THE GRADUATE SCHOOL
OF THE UNIVERSITY OF FLORIDA IN PARTIAL FULFILLMENT
OF THE REQUIREMENTS FOR THE DEGREE OF
DOCTOR OF PHILOSOPHY

UNIVERSITY OF FLORIDA

2010

To my wife, Erin Hirschorn, and my daughter, Sienna Hirschorn

ACKNOWLEDGMENTS

I thank my advisor, Professor Mark E. Orazem, for his expertise, insight, and support in this work. His patience with students is unmatched and he always takes the time to listen and offer his assistance. His interest, thoroughness, and attention to detail has significantly improved my study and has helped push me to realize my capabilities and to improve my weaknesses.

I thank Dr. Bernard Tribollet, Dr. Isabelle Frateur, Dr. Marco Musiani, and Dr. Vincent Vivier for their help developing and improving this study. The extension of their areas of research broadened the scope of this work. I also thank my committee members Professor Jason Weaver, Professor Anuj Chauhan, and Professor Juan Nino.

I thank my wife, my mother, and my father for their love and encouragement during my studies.

TABLE OF CONTENTS

LIST OF TABLES

LIST OF FIGURES

LIST OF SYMBOLS

$\hat{A}$	normalized area
b_a	anodic coefficient, V^{-1}
b_c	cathodic coefficient, V^{-1}
C	capacitance, F/cm^2
C_0	uniform capacitance associated with a surface distribution, F/cm^2
C_B	capacitance-CPE relation derived by Brug *et al.*,[3] F/cm^2
C_d	diffuse layer capacitance, F/cm^2
C_di	dielectric layer capacitance, F/cm^2
C_dl	double layer capacitance, F/cm^2
C_eff	effective capacitance of a system, F/cm^2
$C_\mathrm{eff,f}$	effective capacitance of a dielectric film, F/cm^2
$C_\mathrm{eff,n}$	effective capacitance associated with a normal distribution, F/cm^2
$C_\mathrm{eff,s}$	effective capacitance associated with a surface distribution, F/cm^2
C_HM	capacitance-CPE relation derived by Hsu and Mansfeld,[6] F/cm^2
C_{RC}	capacitance associated with a single time-constant, F/cm^2
F	Faraday's constant, 96,487 C/equiv
f_0	characteristic frequency associated with resistivity ρ_0, $f_0 = (2\pi\rho_0\epsilon\epsilon_0)^{-1}$, Hz
f	frequency, $f = \omega/2\pi$, Hz
f_δ	characteristic frequency associated with resistivity ρ_δ, $f_\delta = (2\pi\rho_\delta\epsilon\epsilon_0)^{-1}$, Hz
f_max	frequency corresponding to largest measured frequency, Hz
f_peak	frequency corresponding to the peak of the imaginary impedance, Hz
f_t	characteristic transitional frequency, Hz
g	tabulated function, see equation (8–23)
i_0	exchange current density, A/cm^2
i_C	capacitive current density, A/cm^2
i_f	faradaic current density, A/cm^2

j imaginary number, $j = \sqrt{-1}$

Q CPE coefficient, $\mathrm{s}^{\alpha}/\Omega\mathrm{cm}^2$

R_b largest value of resistance in a surface distribution , $\Omega\mathrm{cm}^2$

R_e Ohmic resistance, $\Omega\mathrm{cm}^2$

R_f resistance of a film, $\Omega\mathrm{cm}^2$

R_p polarization resistance, $\Omega\mathrm{cm}^2$

R_s smallest value of resistance in a surface distribution , $\Omega\mathrm{cm}^2$

R_t charge-transfer resistance, $\Omega\mathrm{cm}^2$

$R_{\mathrm{t},0}$ linear value of charge-transfer resistance, $\Omega\mathrm{cm}^2$

$R_{\mathrm{t,obs}}$ observed value of charge-transfer resistance, $\Omega\mathrm{cm}^2$

U applied cell potential, V

V interfacial potential, V

Y admittance, $\Omega^{-1}\mathrm{cm}^{-2}$

Z impedance, $\Omega\mathrm{cm}^2$

Z_CPE impedance response that exhibits constant-phase element behavior, $\Omega\mathrm{cm}^2$

$Z_{\mathrm{CPE},R}$ impedance response that exhibits symmetric constant-phase element behavior, $\Omega\mathrm{cm}^2$

Z_j pertaining to the imaginary part of the impedance, $\Omega\mathrm{cm}^2$

Z_r pertaining to the real part of the impedance, $\Omega\mathrm{cm}^2$

α CPE exponent

δ film thickness, cm

ϵ dielectric constant

ϵ_0 permittivity of vacuum, $8.8541 \times 10^{-14}\ F/\mathrm{cm}$

γ power-law exponent

λ Debye length or characteristic length of an exponential function

ρ resistivity, $\Omega\mathrm{cm}$

ρ_0 interfacial resistivity at position 0, $\Omega\mathrm{cm}$

ρ_δ interfacial resistivity at position δ, $\Omega\mathrm{cm}$

τ time-constant, s

ω angular frequency, s^{-1}

ξ normalized distance

Abstract of Dissertation Presented to the Graduate School
of the University of Florida in Partial Fulfillment of the
Requirements for the Degree of Doctor of Philosophy

DISTRIBUTED TIME-CONSTANT IMPEDANCE RESPONSES INTERPRETED IN TERMS OF PHYSICALLY MEANINGFUL PROPERTIES

By

Bryan D. Hirschorn

August 2010

Chair: Mark E. Orazem
Major: Chemical Engineering

Models invoking Constant-Phase Elements (CPE) are often used to fit impedance data arising from a broad range of experimental systems. The physical origins of the CPE remain controversial. CPE parameters are considered to arise from a distribution of time-constants that may be distributed along the surface of an electrode or in the direction normal to the electrode. The capacitance of electrochemical systems is used to calculate properties, such as permittivity, layer thickness, and active surface area. The determination of capacitance from CPE data is often inadequate, leading to erroneous prediction of physical properties.

In the present work, two different mathematical formulas for estimating effective capacitance from CPE parameters, taken from the literature, are associated unambiguously with either surface or normal time-constant distributions. However, these equations were not developed from a physical model and do not properly account for characteristic frequencies outside the measured frequency range. For a broad class of systems, these formulations for capacitance are insufficient, which illustrates the need to develop mechanisms to account for the CPE.

CPE behavior may be attributed to the distribution of physical properties in films, in the direction normal to the electrode surface. Numerical simulations were used to show that, under assumption that the dielectric constant is independent of position, a normal power-law distribution of local resistivity is consistent with the CPE. An analytic

expression, based on the power-law resistivity distribution, was found that relates CPE parameters to the physical properties of a film. This expression yielded physical properties, such as film thickness and resistivity, that were in good agreement with expected or independently measured values for such diverse systems as aluminum oxides, oxides on stainless steel, and human skin.

The agreement obtained using the power-law model can be explained by the fact that it is based on formal solution for the impedance associated with a specified resistivity distribution, rather than using formulations for capacitance that do not take any physical model into account. The power-law model yields a CPE impedance behavior in an appropriate frequency range, defined by two characteristic frequencies. Ideal capacitive behavior is seen above the upper characteristic frequency and below the lower characteristic frequency. A symmetric CPE response at both high and low frequencies can be obtained by adding a parallel resistive pathway.

CPE behavior may also be attributed to the distribution of physical properties along the surface of an electrode. Numerical simulations were used to show that a power-law distribution of Ohmic resistance along a blocking surface with uniform capacitance yielded an impedance response that was consistent with the CPE. The broad distribution necessary suggested that observed CPE behavior cannot be considered to arise from a distribution of Ohmic resistance alone. Nevertheless, the developed relationship between capacitance and CPE parameters for a surface distribution was shown to be different than the relationship developed for a normal distribution indicating that the physical origin of the CPE needs to be considered when assessing capacitance from impedance spectra.

Analysis of systems exhibiting the CPE requires accurate estimates of model parameters. In support of the mechanistic development of the CPE, a generalized method was developed for identifying and minimizing nonlinear distortions in impedance spectra

for increased confidence in model development and parameter estimation. A characteristic transition frequency was defined that can be used to tailor a frequency-dependent input signal to optimize signal-to-noise levels while maintaining a linear response. The Kramers-Kronig relations, which provide an essential tool for assessing the internal consistency of impedance data, are understood to be sensitive to failures of causality, but insensitive to failures of linearity. Numerical simulations showed that the Kramers-Kronig relations are not satisfied for measurements which include the characteristic transition frequency. However, the relations were satisfied for measurements taken below the characteristic frequency, even for very nonlinear systems.

CHAPTER 1
INTRODUCTION

Electrochemical impedance spectroscopy (EIS) is an in-situ, non-invasive technique widely utilized for characterizing electrochemical systems. EIS has been used to investigate a broad range of experimental systems with very different electrochemical properties and is used to advance many areas of science and engineering including product development, diagnostic testing, materials analysis, and mechanistic studies. The scope of EIS is broad, including optics, wet and dry chemistry, solid-state applications, and biochemical processes.

While it can be considered a generalized transfer function approach, EIS usually involves a measured current response to a potential input, where the impedance spectra are generated by changing the frequency of the input signal. Advances in electrical equipment and digital technology have allowed impedance spectra to be collected quickly and accurately. It is the interpretation of results that poses the challenge and the focus of a broad range of research in the field. In general, if impedance techniques are not properly implemented or assessment of the data are unsound, then conclusions drawn from the analysis may be erroneous.

EIS is an appealing technique for electrochemical studies because it allows for the separation of system components, which cannot be achieved through steady-state measurements. For instance, impedance spectra yields information on solution resistance, charge-transfer resistance, and system capacitance. The characteristics of the impedance response provides information on diffusion, convection, kinetics, and reaction mechanisms. Important parameters and physical properties, such as diffusion coefficients, exchange current densities, anodic and cathodic transfer coefficients, permittivity, active surface area, and film and coating thicknesses can be obtained from impedance analysis.

The determination of system capacitance is important for many science and engineering applications because its value provides information regarding active

surface area, layer thickness, and material permittivity. The area-scaled capacitance of electrode/electrolyte interfaces does not vary significantly, and, therefore, the unscaled capacitance value extracted from impedance measurements can be used to estimate active surface area using typical double-layer capacitance values. The determination of reactive area is critical for chemical synthesis applications and energy technologies such as batteries and fuel cells.

For dielectric materials the capacitance is used to obtain permittivity and layer thickness. The determination of capacitance is important, for instance, for the characterization of oxide films. Oxides passivate metals by providing a resistive boundary to corrosion allowing them to be used as building materials. In a similar manner, organic coatings are often used to prevent corrosion. The dielectric properties of oxides are used in the design and fabrication of semiconductors and integrated circuits. The growth of films on catalytic surfaces, such as the electrodes of batteries and fuel cells, can act to both promote and inhibit mass transfer and therefore significantly influence performance. The characterization of human skin is important for the design of electric field driven drug delivery systems. EIS is widely used for the the study of oxides, organic coatings, biological membranes, and even human skin.

Analysis of impedance spectra requires developing models that account for the physical processes of a system such that the desired information can be obtained. It is insufficient to simply fit impedance spectra to a mathematical model or to a collection of passive circuit elements, as such an approach provides little insight into the physical processes that are occurring. Impedance spectra cannot be analyzed from examination of raw data alone. The integrated approach provided by Orazem and Tribollet[7] is to propose a physical model to account for the impedance response of an electrochemical system. Confirmation of a model requires supporting experimental evidence.

Models invoking constant-phase elements (CPE) are often used to fit impedance data arising from a broad range of experimental systems. The CPE is expressed in

terms of model parameters α and Q as

$$Z_{\mathrm{CPE}} = \frac{1}{(j\omega)^{\alpha}Q} \tag{1–1}$$

where ω is the angular frequency of the input signal and $j = \sqrt{-1}$. Equation (1–1) is representative of a blocking system with an infinite low-frequency impedance. When $\alpha = 1$ the system is described by a single time-constant and the parameter Q has units of capacitance, otherwise Q has units of $\mathrm{s}^{\alpha}/\Omega\mathrm{cm}^2$ or $\mathrm{Fs}^{(\alpha-1)}/\mathrm{cm}^2$.[7] Generally, α ranges between 0.5 and 1. For reactive systems

$$Z_{\mathrm{CPE},R} = \frac{R}{1 + (j\omega)^{\alpha}QR} \tag{1–2}$$

where R is a finite low-frequency impedance. The CPE may be included in impedance models incorporating mass-transport effects and/or complicated reaction mechanisms.

Surprisingly, the CPE, which requires only two adjustable parameters, accurately fits the impedance responses of a broad range of experimental systems. The physical origins of the CPE are controversial. Generally, the CPE is considered to arise from a distribution of capacitance. A historical review of the CPE is provided in Chapter 2. In spite of some experimental and theoretical success, the proposed physical models from the literature yield pseudo-CPE behavior, in which α and Q are frequency dependent and are roughly constant only in a small frequency range. In contrast, the CPE behavior for experimental systems generally applies over a large range of frequency in which α and Q are independent of frequency.

The CPE, which is purely a mathematical description, may accurately represent impedance data, but it gives no insight into the physical processes that yield such a response. Nevertheless, capacitance is often extracted from CPE data using expressions provided by Brug *et al.*[3] or by Hsu and Mansfeld[6] that are derived independent of physical models. Application of these expressions to experimental systems, presented

in Chapter 7, often leads to assessment of capacitance that does not agree with independent measurements. In many cases, capacitance is obtained using single-frequency measurements, and therefore, the presence of the CPE is not even taken into consideration. Single frequency approaches can lead to misinterpretation of results. Following the approach taken by Orazem and Tribollet,[7] the interpretation of impedance spectra, and therefore the determination of system capacitance, requires the development of physical models.

The motivation for the present work arises from the fact that, in general, the physical origins of CPE behavior are not well understood. Without the aid of physical models the determination of physical parameters from impedance spectra is ambiguous. The objective is to develop mechanisms that account for the CPE and to provide relationships between the measured CPE parameters and the physical properties of a system.

The development of mechanistic models requires proper implementation of EIS. Model development is enhanced when experimental techniques are optimized and data is verified for consistency. Although the requirement of linearity and the errors that result when linearity is violated are well established, a generalized system-dependent procedure for optimizing experimental techniques is lacking. In Chapters 3 and 4, a generalized method is developed for identifying and minimizing nonlinear distortions in impedance spectra for increased confidence in model development and parameter estimation.

The mathematical characteristics of the CPE are provided in Chapter 5. In Chapter 6, different capacitance-CPE relations, originally derived by Brug *et al.* and Hsu and Mansfeld, are associated unambiguously with either surface or normal time-constant distributions. The formulas for capacitance are applied to different experimental systems in Chapter 7 and the limitations are discussed. The development of resistivity distributions in films that account for the CPE is presented in Chapter 8. An analytic expression

is developed, based on the resistivity distributions, that relates CPE parameters to the physical properties. In Chapter 9, this expression is applied to such diverse systems as aluminum oxides, oxides on stainless steel, and human skin yielding physical properties, such as film thickness and resistivity, that were in good agreement with expected or independently measured values. Surface distributions of Ohmic resistance that result in CPE behavior are derived in Chapter 10. An overview of the relationship between capacitance and CPE parameters is provided in Chapter 11. In Chapter 13, preliminary work for CPE behavior caused by surface distributions of reactivity is provided.

CHAPTER 2
LITERATURE REVIEW

The present chapter provides the origins of the empirical Constant-Phase Element model, proposed physical explanations of the CPE, and derived capacitance-CPE relationships. A historical perspective is also provided on the influence of nonlinearity on impedance spectra and the utility of the Kramers-Kronig relations for validating impedance data.

2.1 The Constant-Phase Element

The CPE has been considered to arise from either a distribution of properties along the surface of an electrode or in the direction normal to the electrode.

2.1.1 Surface Distributions

In 1941, Cole and Cole introduced an empirical formula, now known as a Constant-Phase Element, that accounted for the dielectric response of a broad range of liquids.[8] The dielectric response was characterized as a depressed semicircle in a complex admittance plane plot. Cole and Cole noted that, although the dispersion and absorption of the dielectrics differed, the generalized behavior could be attributed to a single parameter α (see equation (1–2)). Cole and Cole attributed the cause of this behavior to a distribution of relaxation times, or time-constants, and were able to calculate the necessary distributions of time-constants following the methods of Fuoss and Kirkwood.[9] Cole and Cole were unable to provide physical significance to the distribution of time-constants and considered the distribution function as simply a mathematical means of representing the experimental results. Noting that the same characteristic formula could account for otherwise dissimilar dielectrics, Cole and Cole suggested that a more fundamental mechanism must be involved.

Since the 1940s, a broad range of researchers have investigated the possible physical and geometric origins of CPE behavior. In the literature, the origin of CPE behavior has been attributed to porosity, surface roughness, fractal geometry, non-uniform current distributions, and the presence of grain boundaries. The amount of

work on the origins of CPE behavior is extensive and a thorough review is not intended. Rather, a general outline highlighting some of the research is intended to illustrate the ambiguity associated with the CPE.

Brug *et al.* have developed mathematical distributions of time-constants that result in impedance responses that can be expressed in terms of CPE models. In their work, the time-constants were considered to be distributed radially along the electrode surface (2D) and the impedance was obtained from a sum of the admittance of the individual elements.[3] The mathematical development of the distribution functions using the methods of Fuoss and Kirkwood was possible only when the Ohmic and kinetic resistances were held constant and capacitive elements were allowed to be distributed.[3,9] The time-constant distributions that lead to CPE behavior for such a model required that the capacitance vary over many orders of magnitude. Therefore, the models, although mathematically sound, were physically unreasonable as capacitance is not known to have such a broad range of values.

The impedance of porous electrodes has been analytically calculated by de Levie.[10,11] The impedance of a single pore was derived and the overall impedance of the porous electrode was obtained by accounting for an ensemble of individual pores. The impedance response of the overall system led to distortion of the impedance in the high-frequency region such that an α parameter of less than unity was observed.[12,13] However, the calculated value of α for the porous electrode model was frequency-dependent and therefore not characteristic of true CPE behavior.

CPE behavior has been attributed to heterogeneity of electrode surfaces. The experimental work of de Levie showed a relationship between electrode surface roughness and the phase-angle associated with CPE behavior.[14] Scheider used a branched-ladder network of resistors and capacitors to account for CPE behavior of rough or uneven surfaces.[15] The ladder-network was intended to relate microscopic heterogeneities with the macroscopic response. Le Mehaute and Crepy connected fractal geometry of electrode

surfaces with CPE behavior.[16] Nyikos and Pajkossy showed that the CPE parameter α could be expressed as a function of fractal dimension, and interpreted α as a measure of surface irregularity regardless of the shape and structure of the irregularities.[17] Huang *et al.* have shown that pseudo-CPE behavior, where α and Q are frequency dependent, can arise from geometrical effects due to current and potential distributions on electrode surfaces.[18,19,2]

In spite of some experimental and theoretical success, the physical phenomena that cause CPE behavior remain controversial. Keddam and Takenouti[20] and Wang[21] have questioned the validity of the relationship between the CPE parameter α and fractal dimension. Bates *et al.* experimentally showed no correlation between α and fractal dimension.[22] Arguments that the source of CPE behavior is purely an interfacial phenomenon or due to interfacial and bulk property coupling were summarized by Pajkossy.[23] Another comprehensive review of fractals and rough electrodes as they pertain to impedance measurements was provided by de Levie.[24]

2.1.2 Normal Distributions

Jorcin *et al.*[5] have used Local Electrochemical Impedance Spectroscopy (LEIS) to attribute CPE behavior seen in the global measurements to either surface or normal time-constant distributions. Normal distributions of time-constants can be expected in systems such as oxide films, organic coatings, and human skin. Such normal time-constant distributions may be caused by distributions of resistivity and/or dielectric constant. The range of values expected for a dielectric constant, however, should be much narrower than that expected for resistivity.

Yamamoto and Yamamoto[25] have used a rectangular probability function to model resistivity distributions. The Young model, developed for niobium oxide, assumes an exponential distribution of resistivity within a material.[26] Yamamoto and Yamamoto[27] and Poon and Choy[28] used exponential resistivity profiles to model the impedance of human stratum corneum. Bojinov *et al.*[29] and Schiller and Strunz[30] used the Young

model to fit electrochemical impedance data and predict physical properties, including film thickness. Bojinov *et al.* summarized the justification of an exponential decay of resistivity by using point-defect conduction theory in passive films.[31] Schiller and Strunz[30] derived an approximate relationship between the Young model parameter, λ, and the CPE parameter, α.

An exponential decay of resistivity is a good first approximation of a physical model that results in an impedance response that can be expressed in terms of a CPE. However, the model is insufficient in the sense that it results in pseudo-CPE behavior; specifically, the α and Q values that are extracted from the EIS response are functions of frequency. In addition, only a limited range of α values are possible from such a model, and thus a broad class of systems cannot be attributed to an exponential resistivity decay. The characteristics of the Young model are provided in Chapter 8.

2.2 Determination of Capacitance from the CPE

In Chapter 1, the importance of determining the capacitance of electrochemical systems was discussed. As shown by equations (1–1) and (1–2), when an electrochemical system is described by a single time-constant $\alpha = 1$ and Q has units of capacitance. When $\alpha < 1$, the relationship between the impedance response and the value of the interfacial capacitance is ambiguous. It is clear that the CPE parameter Q cannot represent the capacitance when $\alpha < 1$. A number of researchers have explored the relationship between CPE parameters and the interfacial capacitance. By treating a surface distribution of time constants, Brug *et al.*[3] developed a relationship between interfacial capacitance and CPE parameters for both blocking and Faradaic systems. Hsu and Mansfeld[6] proposed a different relationship for capacitance in terms of the CPE parameters. These expressions are presented with derivation in Chapter 6.

The formulas yield different results for the effective capacitance. Using numerical simulations for the influence of geometry-induced current distributions, Huang *et al.*[18]

have shown that current and potential distributions induce a high-frequency pseudo-CPE behavior in the global impedance response of a disk electrode with a Faradaic reaction.[2] Their work demonstrated that the Brug formula for effective capacitance yielded a more accurate estimate than did the Hsu and Mansfeld equation.

Both the Brug formulas and the Hsu and Mansfeld formula have been widely used to extract effective capacitance values from CPE parameters. The Brug formulas have been used to extract capacitance values from CPE parameters for studies on double layers,[32–36] hydrogen sorption in metals,[37,38] hydrogen evolution,[39–44] oxygen evolution,[45] porous electrodes,[46] self-assembled monolayers,[47,48] polymer films,[49] and passive films.[50,51] Similarly, the Hsu and Mansfeld formula has been used to extract capacitance values from CPE parameters for studies on passive films,[50–52] protective coatings,[53–56] and corrosion inhibitors.[57] For a given set of CPE parameters, the Brug formulas and the Hsu and Mansfeld formula yield different values; yet, in some cases, both sets of equations have been applied to similar systems.

2.3 Errors Associated with Nonlinearity

Model development and parameter estimation requires that EIS is properly implemented. While it can be considered a generalized transfer function approach, electrochemical impedance spectroscopy usually involves a measured current response to a potential input. In its common application, the technique relies on use of a small input signal amplitude to ensure a linear response which can be interpreted using theories of linear transfer functions. In general, there is a trade-off between implementing a signal that is large enough to achieve an adequate signal-to-noise ratio, while at the same time ensuring that the signal is not too large such that linearity is violated. Most experimentalists employ a 10 mV input signal amplitude, but there is reason to expect, given the wide range of electrochemical properties investigated with this technique, that this amplitude may not be optimal for many experimental systems.

Orazem and co-authors have investigated the error structure of impedance measurements, using a measurement model approach to quantify both stochastic and bias errors in replicated spectra.[58–61] Minimization of stochastic errors serves to improve the regression analysis for interpretation of spectra. A large input amplitude generally reduces the stochastic errors, but an amplitude that is too large results in errors associated with the nonlinear response.

The selection of appropriate input amplitudes has drawn interest in the literature. Use of an input perturbation that is too large yields an incorrect value for the charge-transfer resistance. Darowicki investigated the effect of the input amplitude on the error of charge-transfer resistance obtained from impedance measurements.[62] He showed that the impedance spectrum of a nonlinear electrical system depends on both the frequency and amplitude of the input signal. He demonstrated that the polarization resistance uncorrupted by nonlinear effects can be determined by extrapolating to the zero value of the amplitude of the input signal. Diard *et al.* studied the dependence of impedance measurement error on the electrode potential and the sinusoidal voltage amplitude for a nernstian redox system.[63] He showed that for his given system the impedance measurement error was independent of frequency in the low frequency range.

In a separate work, Darowicki showed that, for systems with a non-negligible Ohmic resistance, the interfacial potential differs from the applied potential signal.[64] He derived an expression for the interfacial potential using a series expansion approach that relates the interfacial potential to the amplitude of the input signal, the input frequency, the electrolyte resistance, the double layer capacitance, and the kinetic parameters. Darowicki found that, for all input amplitudes, the effective interfacial potential changes with frequency due to the frequency dependence of the charging current, having a maximum amplitude at low frequency and tending toward zero at high frequency. As a result of this effect, the influence of a large input amplitude changes with frequency.

Darowicki provided a method for determining the frequency for which impedance measurements will be linear in character.[64] Darowicki's observations were supported by the modeling work of Popkirov and Schindler who developed synthetic data for a charge-transfer resistor obeying Butler-Volmer kinetics in parallel with a double layer capacitance.[65] Their results showed that the perturbation amplitude had no effect on the impedance values in the high-frequency range where the charging current dominates. Alternatively, in the low-frequency range, a decrease of the impedance values was observed with increasing input signal amplitude.

There has been significant effort to determine the linear impedance values when nonlinear errors are not negligible. Diard *et al.* quantified the deviation of the measured polarization resistance due to nonlinearity using a successive derivative approach.[66–68] Diard *et al.* developed expressions for the electrochemical response of a two-step reaction to a sinusoidal perturbation that results in nonlinear impedance.[69] He used numerical methods to show that deviation from the linearized system depended on the kinetic parameters, the electrode potential, the input amplitude, and the frequency. Milocco used a Taylor series method to determine the linear impedance response when the perturbation caused a nonlinear response.[70]

From an experimental perspective, Van Gheem *et al.*[71] and Blajiev *et al.*[72] used multisine broadband signals to detect nonlinearities in electrochemical systems. These groups were able to distinguish measurement errors caused by stochastic noise and errors caused by nonlinear distortions.

As mentioned previously, the effect of frequency, kinetic parameters, and Ohmic resistance on linear responses in EIS is well documented. However, kinetic coefficients are often not known or not easily obtained, therefore, it would be beneficial to relate the conditions necessary for linearity to global system parameters that can be obtained directly from EIS. In addition, the effect of frequency is generally discussed qualitatively, specifically, that at limiting low-frequencies the greatest degree of nonlinearity is

observed and at limiting high-frequencies the response is linear. It would be beneficial to quantitatively relate the measurement frequency to the degree of nonlinearity using global system parameters such that an optimized signal-to-noise ratio can be achieved during EIS. Based on numerical simulations, a generalized method for optimizing signal-to-noise levels while maintaining a linear response is provided in Chapter 3.

2.4 Linearity and the Kramers-Kronig Relations

When developing physical models from EIS it is critical that the experimental data is reliable and useful. The Kramers-Kronig relations, derived for systems that can be assumed to be linear, stable, and causal, have proven useful for confirming the self-consistency of electrochemical impedance data. Failure of impedance data to satisfy the Kramers-Kronig relations at high frequencies can generally be attributed to instrumental artifacts, and low-frequency deviations can be attributed to nonstationary behavior. Instrumental artifacts and nonstationary behavior represent violations of causality.

While assumption of linearity is essential for the derivation of the Kramers-Kronig relations, the Kramers-Kronig relations are generally considered to be insensitive to nonlinear behavior in electrochemical systems.[73] Urquidi-Macdonald *et al.*[74] used experimental data to show that the Kramers-Kronig transforms are highly sensitive to the condition of causality and are insensitive to the condition of linearity. Their evaluation of the effect of the linearity condition on the Kramers-Kronig transforms was accomplished by varying the amplitude of the input potential perturbation signal during subsequent impedance scans for the corrosion of iron in a 1 M $\mathrm{H_2SO_4}$ solution. For the largest amplitudes, the magnitude of the impedance decreased significantly from the small amplitude case, indicating violation of the linearity condition for their system. The data were nevertheless shown to remain consistent with Kramers-Kronig transforms for all input amplitudes tested. The result showed that the Kramers-Kronig relations were insensitive to the condition of linearity which was clearly violated for large perturbation inputs. Urquidi-Macdonald *et al.* attributed the cause of this insensitivity to an equal

decrease in the real and imaginary components of the impedance when the perturbation amplitude was increased and to the ability of the frequency response analyzer to reject harmonics.

The issue of nonlinearity in impedance measurements is important. While the Kramers-Kronig relations have not been found useful for assessing the appearance of nonlinearity, experimental methods, such as examination of low-frequency Lissajous plots, can be used to identify nonlinear responses.[7,75] Application of a random phase multisine input can be used to resolve nonlinear contributions to the error structure of impedance measurements.[76–78]

In support of model development, numerical simulations were used to identify the conditions under which the Kramers-Kronig relations are sensitive to nonlinear behavior. The utility of the Kramers-Kronig relations for identifying nonlinear distortions and an explanation for the lack of sensitivity of the Kramers-Kronig relations to nonlinear behavior reported by Urquidi-Macdonald *et al.*[74] is provided in Chapter 4.

CHAPTER 3
OPTIMIZATION OF SIGNAL-TO-NOISE RATIO UNDER A LINEAR RESPONSE

Developing physical models that account for impedance spectra first requires that experimental techniques are properly implemented and fully optimized. In the present chapter, numerical simulations of electrochemical systems were used to explore the influence of large-amplitude potential perturbations on the measured impedance response. The amplitude of the input potential perturbation used for impedance measurements, normally fixed at a value of 10 mV for all systems, should instead be adjusted for each experimental system. Guidelines are developed for selection of appropriate perturbation amplitudes. A characteristic transition frequency is defined that can be used to tailor a frequency-dependent input signal to optimize signal-to-noise levels while maintaining a linear response.

3.1 Circuit Models Incorporating Faradaic Reactions

The nonlinear response in electrochemical systems typically results from the potential dependence of Faradaic reactions. For example, both Tafel and Butler-Volmer reaction kinetics display an exponential dependence on the interfacial potential. The total current passed through the electrode contributes to charging the interface and to the Faradiac reaction. These contributions are presented in parallel in the circuit presented in Figure 3-1(a), where the use of a box for the Faradaic reaction is intended to emphasize the complicated and nonlinear potential dependence. Addition of an Ohmic character of the electrolyte causes the interfacial potential V to differ from the applied potential U. This effect is illustrated in Figure 3-1(b).

The applied potential U can be expressed as a sinusoidal perturbation about a steady value $\overline{U}$ as

$$U = \overline{U} + \Delta U \cos(\omega t) \tag{3–1}$$

where ΔU is the input amplitude, ω is the input angular frequency, and t is time. In the absence of an Ohmic resistance, as shown in Figure 3-1(a), the applied cell potential U

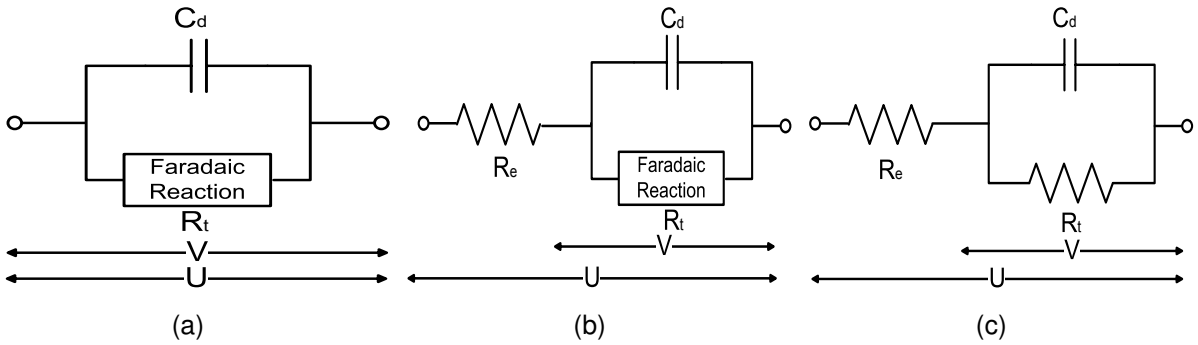

Figure 3-1. Circuit models with Faradaic reaction: a) non-Ohmic Faradaic system; b) Ohmic Faradaic system; and c) Ohmic constant charge-transfer resistance system.

and the interfacial potential V are equal. In the presence of an Ohmic resistance R_{e} the applied cell potential is related to the interfacial potential by

$$U = V + (i_f + i_C)R_{\mathrm{e}} \tag{3–2}$$

The Faradaic current density can be expressed as

$$i_f = i_0[\exp(b_a(V - V_0)) - \exp(-b_c(V - V_0))] \tag{3–3}$$

or equivalently,

$$i_f = K_a \exp(b_a V) - K_c \exp(-b_c V) \tag{3–4}$$

where b_a and b_c are the anodic and cathodic coefficients with units of inverse potential and K includes the the exchange current i_0 and the equilibrium potential difference V_0 as $K_a = i_0 \exp(-b_a V_0)$ and $K_c = i_0 \exp(b_c V_0)$. When b_a and b_c are related through the symmetry factor, the general form of Equation (3–4) for independent reactions simplifies to that of Butler-Volmer kinetics. The capacitive current is expressed as

$$i_C = C_{\mathrm{dl}} \frac{dV}{dt} \tag{3–5}$$

where C_{dl} is the double layer capacitance. The total current passing through the cell is the sum of the Faradaic and capacitive contributions, *i.e.,*

$$i = i_f + i_C \tag{3–6}$$

In the absence of an Ohmic resistance, *i.e.,* as shown in Figure 3-1(a), equations (3–1)-(3–6) can yield an analytic expression for current density as a function of applied potential $U = V$;

$$i = -\omega C_{\mathrm{dl}} \Delta V \sin(\omega t) + K_a \exp(b_a(\overline{V} + \Delta V \cos(\omega t)) - K_c \exp(-b_c(\overline{V} + \Delta V \cos(\omega t)) \tag{3–7}$$

The current and potential terms cannot be separated in the more general case given in Figure 3-1(b), and a numerical method must be employed.

3.2 Numerical Solution of Nonlinear Circuit Models

A numerical method was used to estimate the time-dependent current response to a sinusoidal potential input using the electrical circuit presented as Figure 3-1(b) for which the charge-transfer resistance R_{t} is a nonlinear function of potential. The relationship between current and potential can be expressed in the form of a single differential equation,

$$\frac{dV}{dt} C_{\mathrm{dl}} R_{\mathrm{e}} + V\left(1 + \frac{R_{\mathrm{e}}}{R_{\mathrm{t}}(t)}\right) = \overline{U} + \Delta U \cos(\omega t) \tag{3–8}$$

in which $R_{\mathrm{t}}(t)$ is a function of potential and, therefore, a function of time. Equation (3–8) can be solved analytically for fixed R_{t} using the integrating factor approach. The equivalent circuit of such a system is shown in Figure 3-1(c). The solution of equation (3–8) for fixed R_{t} can be expressed as

$$V(t) = A\left(\cos(\omega t) + \frac{\omega C_{\mathrm{dl}} R_{\mathrm{e}} R_{\mathrm{t}}}{(R_{\mathrm{t}} + R_{\mathrm{e}})} \sin(\omega t)\right) + V^* \tag{3–9}$$

where

$$A = \frac{\Delta U (R_{\mathrm{t}} + R_{\mathrm{e}})}{R_{\mathrm{t}} (C_{\mathrm{dl}} R_{\mathrm{e}})^2} \left[\frac{(R_{\mathrm{t}} + R_{\mathrm{e}})^2}{(R_{\mathrm{t}} C_{\mathrm{dl}} R_{\mathrm{e}})^2} + \omega^2\right]^{-1} \tag{3–10}$$

and V^* is a constant of integration. A similar approach was taken by Xiao and Lalvani, who solved a linearized form of the Tafel equation to develop expressions for potential and current in a corrosion system.[79]

The value of the charge-transfer resistance at a given potential $V(t)$ can be calculated from the slope of the interfacial polarization curve, *i.e.,*

$$R_{\mathrm{t}}(t) = (K_a b_a \exp(b_a V(t)) + K_c b_c \exp(-b_c V(t)))^{-1} \tag{3–11}$$

Under the assumption that, for short time periods, *i.e.,* small movements on the polarization curve, the charge-transfer resistance is constant, an iterative procedure using equations (3–9) and (3–11) was used to calculate the development of V and i as functions of time. This procedure allowed for the complete determination of the system described by a potential-dependent charge-transfer resistance. The analytic equations derived for a fixed charge-transfer resistance can be used to approximate the solution to Figure 3-1(b) for which the charge transfer resistance varies with interfacial potential. The rationale for this approximation is developed in Section 3.3.4.

The impedance response was calculated directly for each frequency using Fourier integral analysis.[80] The fundamental of the real and imaginary components of the current signal, for example, can be expressed as

$$I_r(\omega) = \frac{1}{T}\int_0^T I(t)\cos(\omega t)dt \tag{3–12}$$

and

$$I_j(\omega) = -\frac{1}{T}\int_0^T I(t)\sin(\omega t)dt \tag{3–13}$$

respectively, where $I(t)$ is the current signal, ω is the input frequency, and T is the period of oscillation. Similar expressions can be found for real and imaginary components of the potential signal. The real and imaginary components of the impedance can be found from

$$Z_r(\omega) = \mathrm{Re}\left\{\frac{U_r + jU_j}{I_r + jI_j}\right\} \tag{3–14}$$

and

$$Z_j(\omega) = \mathrm{Im}\left\{\frac{U_r + jU_j}{I_r + jI_j}\right\} \tag{3–15}$$

respectively, where j represents the imaginary number. The advantage of the numerical approach employed here was that it could be applied to general forms of nonlinear behavior, including consideration of a potential-dependent capacitance. Details of algorithm used for the numerical method is provided in Appendix A.

3.3 Simulation Results

The objective of this presentation is to make the analysis of system nonlinearity useful to the experimentalist. To that end, guidelines are provided to assess appropriate perturbation amplitudes as functions of kinetic and Ohmic parameters, and experimental methods are discussed for assessing the condition of linearity. The frequency dependence of the interfacial potential can be exploited to tailor input signals.

3.3.1 Errors in Assessment of Charge-Transfer Resistance

In the limit that the perturbation amplitude tends toward zero, the polarization resistance can be expressed as

$$R_{p,0} = \lim_{\Delta U \to 0}\left(\frac{\partial U}{\partial i_f}\right)_{c_i(0),\gamma_k} \tag{3–16}$$

where U is the cell potential, ΔU is the amplitude of the input cell potential signal, i_f is the Faradaic current density, $c_i(0)$ is the concentration of species i evaluated at the electrode surface, and γ_k is the fractional surface coverage of adsorbed species k. Equation (3–16) can be expressed in terms of an effective charge-transfer resistance as

$$R_{\mathrm{t},0} = \lim_{\Delta U \to 0}\left(\frac{\partial V}{\partial i_f}\right)_{c_i(0),\gamma_k} \tag{3–17}$$

where V is the interfacial potential. For the kinetics described in the previous sections, the linear value of the charge-transfer resistance is given as

$$R_{\mathrm{t},0} = (K_a b_a \exp(b_a \overline{V}) + K_c b_c \exp(-b_c \overline{V}))^{-1} \tag{3–18}$$

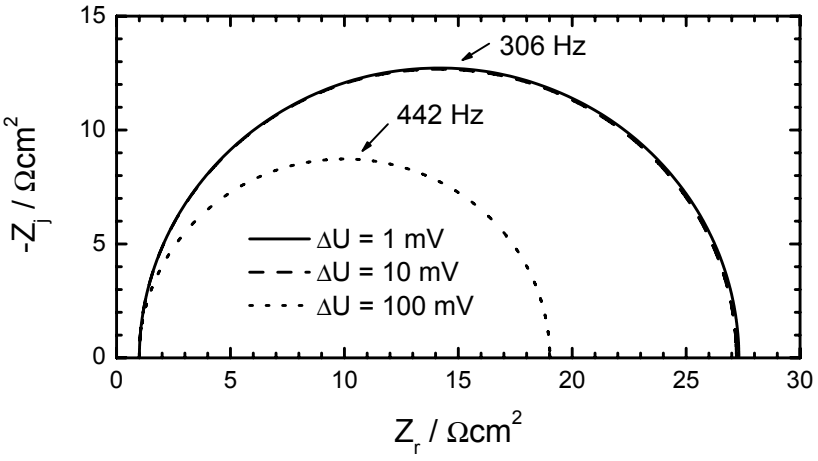

Figure 3-2. Calculated impedance response with applied perturbation amplitude as a parameter. The system parameters were $R_{\mathrm{e}} = 1\ \Omega\mathrm{cm}^2$, $K_a = K_c = 1$ mA/cm^2, $b_a = b_c = 19\ \mathrm{V}^{-1}$, $C_{\mathrm{dl}} = 20\ \mu$F/cm^2, and $\overline{V} = 0$ V, giving rise to a linear charge-transfer resistance $R_{\mathrm{t},0} = 26\ \Omega\mathrm{cm}^2$.

where $\overline{V}$ represents the potential at which the impedance measurement is made.

The calculated impedance response is given in Figure 3-2 with applied perturbation amplitude as a parameter. The system parameters were $R_{\mathrm{e}} = 1\ \Omega\mathrm{cm}^2$, $K_a = K_c = 1$ mA/cm^2, $b_a = b_c = 19\ \mathrm{V}^{-1}$, $C_{\mathrm{dl}} = 20\ \mu$F/cm^2, and $\overline{V} = 0$ V, giving rise to a linear charge-transfer resistance $R_{\mathrm{t},0} = 26\ \Omega\mathrm{cm}^2$. The results presented in Figure 3-2 are consistent with the observation of Darowicki that the measured charge-transfer resistance decreases with increased amplitude of the perturbation signal.[62] As suggested by equation (3–16), the decrease in the measured charge-transfer resistance with increased amplitude is not a general result and depends on the polarization behavior.[66]

3.3.2 Optimal Perturbation Amplitude

A guideline for selection of the perturbation amplitude needed to maintain linearity under potentiostatic regulation can be obtained by using a series expansion for the current density. Similar series-expansion approaches that express deviations from linearity in electrochemical systems have been provided by Diard *et al.* , Kooyman *et al.* , and Gabrielli *et al.*[66,67,69,81,82] For a system that follows a Faradaic reaction, the current

density response to an interfacial potential perturbation

$$V(t) = \overline{V} + \Delta V \cos(\omega t) \tag{3–19}$$

is given by

$$i_f(t) = K_a \exp(b_a V) - K_c \exp(-b_c V) \tag{3–20}$$

Thus,

$$i_f(t) = K_a \exp\left(b_a(\overline{V} + \Delta V \cos \omega t)\right) - K_c \exp\left(-b_c(\overline{V} + \Delta V \cos \omega t)\right) \tag{3–21}$$

or

$$i_f(t) = \overline{K}_a \exp(b_a \Delta V \cos \omega t) - \overline{K}_c \exp(-b_c \Delta V \cos \omega t) \tag{3–22}$$

where

$$\overline{K}_a = K_a \exp(b_a \overline{V}) \tag{3–23}$$

and

$$\overline{K}_c = K_c \exp(-b_c \overline{V}) \tag{3–24}$$

A Taylor series expansion yields

$$\begin{aligned} i_f(t) = \overline{K}_a(1 + b_a \Delta V \cos \omega t + \frac{b_a^2 \Delta V^2 \cos^2 \omega t}{2!} \\ + \frac{b_a^3 \Delta V^3 \cos^3 \omega t}{3!} + \ldots\ldots + \frac{b_a^n \Delta V^n \cos^n \omega t}{n!} + \ldots) \\ - \overline{K}_c(1 - b_c \Delta V \cos \omega t + \frac{b_c^2 \Delta V^2 \cos^2 \omega t}{2!} \\ - \frac{b_c^3 \Delta V^3 \cos^3 \omega t}{3!} + \ldots + \frac{b_c^n \Delta V^n \cos^n \omega t}{n!} + \ldots) \end{aligned} \tag{3–25}$$

The mean value of the current $i_f(t)$ is, for T equal to an integer number of cycles,

$$\bar{i}_f = \frac{1}{T} \int_0^T i_f(t) dt \tag{3–26}$$

By taking into account the formula

$$\int \cos^n x dx = \frac{1}{n} \cos^{n-1} x \sin x + \frac{n-1}{n} \int \cos^{n-2} x dx \tag{3–27}$$

and observing that $\sin T = 0$,

$$\int_0^T \cos^n x dx = \frac{n-1}{n} \int_0^T \cos^{n-2} x dx \tag{3–28}$$

If n is an even number,

$$\int_0^T \cos^n x dx = \frac{n-1}{n} \frac{n-3}{n-2} \dots \frac{1}{2} T \tag{3–29}$$

and if n is an odd number, the value of the integral is equal to zero. Thus, the mean value of $i_f(t)$ is

$$\bar{i}_f = \overline{K}_a \left(1 + \sum_{n=1}^{\infty} \frac{b_a^{2n} \Delta V^{2n}}{(2^n n!)^2} \right) - \overline{K}_c \left(1 + \sum_{n=1}^{\infty} \frac{b_c^{2n} \Delta V^{2n}}{(2^n n!)^2} \right) \tag{3–30}$$

Evaluation of the harmonics of the nonlinear current response can be achieved by introduction of the trigonometric expressions

$$\cos 2x = 2 \cos^2 x - 1 \tag{3–31}$$

and

$$\cos 3x = 4 \cos^3 x - 3 \cos x \tag{3–32}$$

By considering only the three first terms of the Taylor series, $i_f(t)$ becomes

$$\begin{aligned} i_f(t) = \overline{K}_a ((1 + \frac{b_a^2 \Delta V^2}{4}) + (b_a \Delta V + \frac{3 b_a^3 \Delta V^3}{24}) \cos(\omega t) \\ + \frac{b_a^2 \Delta V^2}{4} \cos(2\omega t) + \frac{b_a^3 \Delta V^3}{24} \cos(3\omega t)) \\ - \overline{K}_c ((1 + \frac{b_c^2 \Delta V^2}{4}) - (b_c \Delta V + \frac{3 b_c^3 \Delta V^3}{24}) \cos(\omega t) \\ + \frac{b_c^2 \Delta V^2}{4} \cos(2\omega t) - \frac{b_c^3 \Delta V^3}{24} \cos(3\omega t)) \end{aligned} \tag{3–33}$$

The limitation to the first three terms of the Taylor series gives for the mean value only the first term of the series (see equation (3–30)).

Equation (3–33) can be written as

$$i_f(t) = \bar{i}_f + i_{f,1} \cos(\omega t) + i_{f,2} \cos(2\omega t) + i_{f,3} \cos(3\omega t) \dots \tag{3–34}$$

where the dc current is given by

$$\bar{i}_f = \overline{K}_a \left(1 + \frac{b_a^2 \Delta V^2}{4}\right) - \overline{K}_c \left(1 + \frac{b_c^2 \Delta V^2}{4}\right) \tag{3–35}$$

and the first harmonic or fundamental is given by

$$i_{f,1} = \overline{K}_a \left(b_a \Delta V + \frac{3 b_a^3 \Delta V^3}{24}\right) + \overline{K}_c \left(b_c \Delta V + \frac{3 b_c^3 \Delta V^3}{24}\right) \tag{3–36}$$

For ΔV smaller than $0.2\sqrt{\frac{\overline{K}_a - \overline{K}_c}{\overline{K}_a b_a^2 - \overline{K}_c b_c^2}}$, the variation of the dc current is smaller than 1 percent. For ΔV smaller than $0.2\sqrt{\frac{\overline{K}_a b_a + \overline{K}_c b_c}{\overline{K}_a b_a^3 + \overline{K}_c b_c^3}}$, the variation of the fundamental is smaller than 0.5 percent.

Application of a large-amplitude potential perturbation to a nonlinear system results in harmonics that appear at frequencies corresponding to multiples of the fundamental or applied frequency. Observation that application of a large-amplitude potential perturbation to a nonlinear system changes both the steady-state current density and the fundamental current response. The implication of this result is that the impedance response will also be distorted by application of a large-amplitude potential perturbation.

In the presence of a significant Ohmic resistance, the guideline for the low-frequency perturbation amplitude is

$$\Delta U = 0.2\sqrt{\frac{\overline{K}_a b_a + \overline{K}_c b_c}{\overline{K}_a b_a^3 + \overline{K}_c b_c^3}} \left(1 + \frac{R_\mathrm{e}}{R_{\mathrm{t,obs}}}\right) \tag{3–37}$$

where $R_{\mathrm{t,obs}}$ is the effective charge-transfer resistance measured at the given perturbation amplitude. Thus, a larger perturbation amplitude should be applied for systems where $(1 + R_\mathrm{e}/R_{\mathrm{t,obs}})$ is much larger than unity. The rationale for equation (3–37) is developed in Section 3.3.4.

The percent error in the low-frequency impedance asymptote associated with use of a large-amplitude potential perturbation is given in Figure 3-3 under the assumption of Tafel kinetics with $b\Delta V$ as a parameter. At a value of $b\Delta V = 0.2$, the error in the

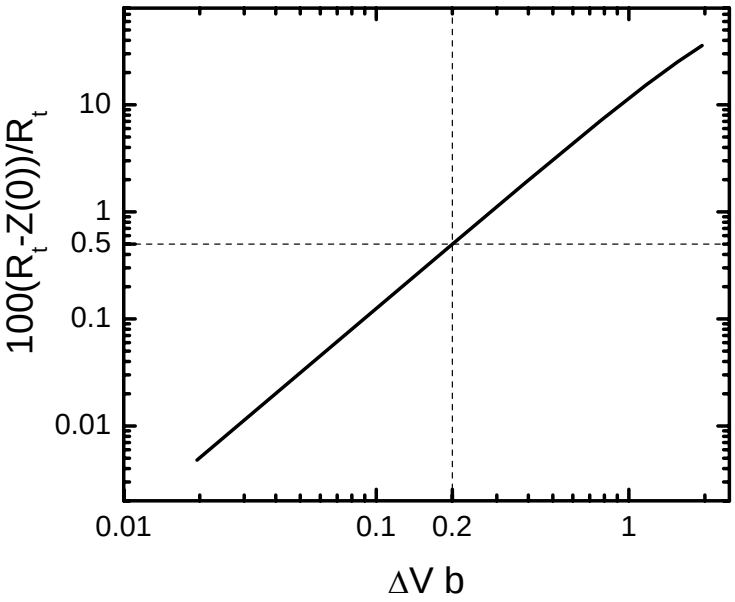

Figure 3-3. The error in the low-frequency impedance asymptote associated with use of a large amplitude potential perturbation.

low-frequency impedance asymptote is 0.5 percent. The corresponding perturbation amplitude is 10.4 mV for a Tafel slope of 120 mV/decade, and 5.2 mV for a Tafel slope of 60 mV/decade.

3.3.3 Experimental Assessment of Linearity

As indicated by Urquidi-Macdonald *et al.* ,[74] the Kramers-Kronig relations do not provide a useful tool for identifying errors associated with a nonlinear response to a large perturbation amplitude. The general utility of Kramers-Kronig relations for identifying errors associated with nonlinearity is provided in Chapter 4. Sequential impedance measurements conducted with different perturbation amplitudes can be used to find the optimal input perturbation, but this process is time consuming.

A more rapid assessment of a nonlinear system response can be obtained by observing distortions in Lissajous plots at low frequency. Lissajous plots are presented in Figure 3-4 with perturbation amplitude and frequency as parameters. The system parameters were $R_{\mathrm{e}} = 0\ \Omega\mathrm{cm}^2$, $K_a = K_c = 1$ mA/cm^2, $b_a = b_c = 19\ \mathrm{V}^{-1}$, $C_{\mathrm{dl}} = 20\ \mu$F/cm^2, and $\overline{V} = 0$ V, giving rise to a linear charge-transfer resistance $R_{\mathrm{t},0} = 26\ \Omega\mathrm{cm}^2$. At the

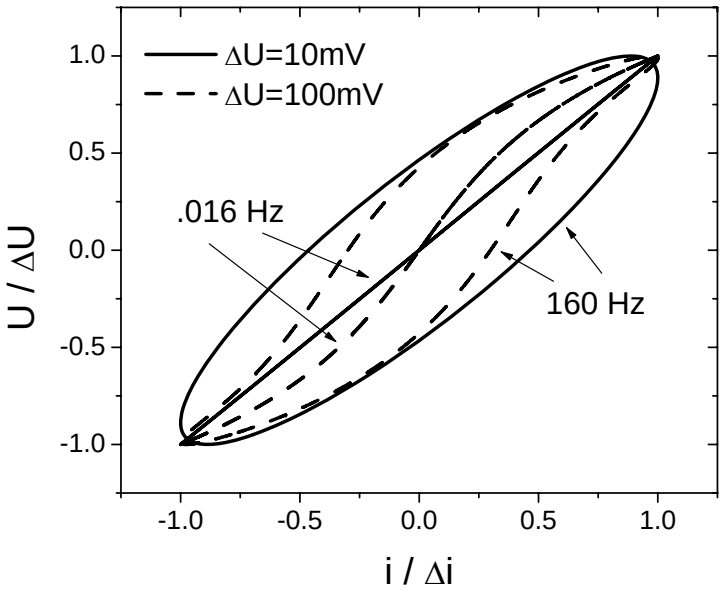

Figure 3-4. Lissajous plots with perturbation amplitude and frequency as parameters. The system parameters were $R_{\mathrm{e}} = 0\ \Omega\mathrm{cm}^2$, $K_a = K_c = 1$ mA/cm^2, $b_a = b_c = 19\ \mathrm{V}^{-1}$, $C_{\mathrm{dl}} = 20\ \mu$F/cm^2, and $\overline{V} = 0$ V, giving rise to a linear charge-transfer resistance $R_{\mathrm{t},0} = 26\ \Omega\mathrm{cm}^2$.

low frequency of 0.016 Hz, a straight line is observed for a perturbation amplitude of 10 mV; whereas, a sigmoidal shape is evident for a perturbation amplitude of 100 mV. The sigmoidal shape is seen because the calculations were performed at $\overline{V} = 0$ V. A deviation from a straight line will be seen for large amplitudes at larger or smaller applied potentials, but the shape will be altered. At the larger frequency of 160 Hz, the differences between the smaller and larger perturbation amplitudes becomes less apparent, and the two curves superimpose as a perfect circle at large frequencies due to the domination of the capacitive current. Similar results are seen for the case where $R_{\mathrm{e}} \neq 0$, with the exception that the Lissajous plot appears as a straight line at both low and high frequencies. The influence of nonlinearities is seen at low frequency.

3.3.4 Frequency Dependence of the Interfacial Potential

In the absence of Ohmic resistance or when a linear approximation is sufficient, the interfacial potential is a sinusoidal quantity and ΔV represents the amplitude of

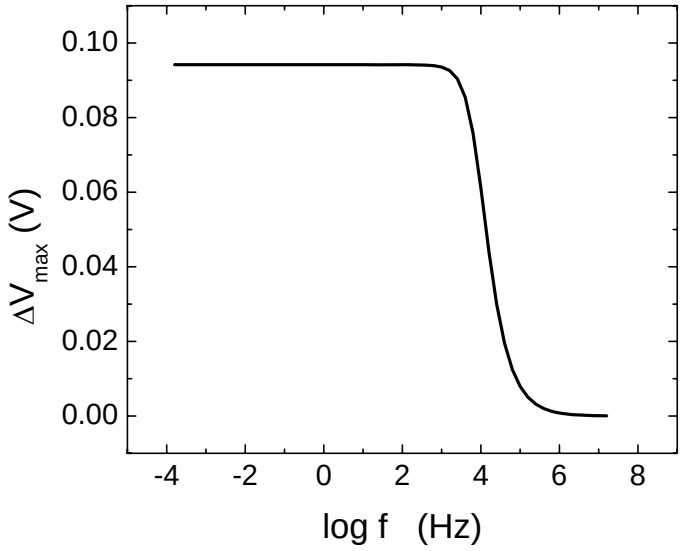

Figure 3-5. Maximum variation of the interfacial potential signal as a function of frequency for parameters $\Delta U = 100$ mV, $R_{\mathrm{e}} = 1\ \Omega\mathrm{cm}^2$, $C_{\mathrm{dl}} = 20\ \mu\mathrm{F/cm}^2$, and $R_{\mathrm{t},0} = 26\ \Omega\mathrm{cm}^2$.

the interfacial potential. For large perturbations the interfacial potential signal contains nonlinear distortions, thus, in the following discussion $\Delta V_{\max}$ represents the maximum variation of the interfacial potential signal. The calculated $\Delta V_{\max}$ is presented in Figure 3-5 as a function of frequency for a system with parameters $\Delta U = 100$ mV, $R_{\mathrm{e}} = 1\ \Omega\mathrm{cm}^2$, $C_{\mathrm{dl}} = 20\ \mu\mathrm{F/cm}^2$, and $R_{\mathrm{t},0} = 26\ \Omega\mathrm{cm}^2$. At high frequencies $\Delta V_{\max}$ is damped and tends toward zero.

Equation (3–9), although derived for a constant charge-transfer resistance, can be used to approximate the interfacial potential of a nonlinear system if the charge-transfer observed at low frequency, $R_{\mathrm{t,obs}}$, is used in the equation. As shown in Figure 3-6, $\Delta V_{\max}$ resulting from the numeric calculation is compared to ΔV calculated from equation (3–9). The agreement shown between the numerical solution and the solution obtained using equation (3–9) confirms that equation (3–9) is useful for approximating the behavior of the interfacial potential, even though it is derived from a constant charge-transfer resistance. It should be noted that the sinusoidal time-domain approximation will not contain the nonlinear distortions and will have maximum error at low frequency.

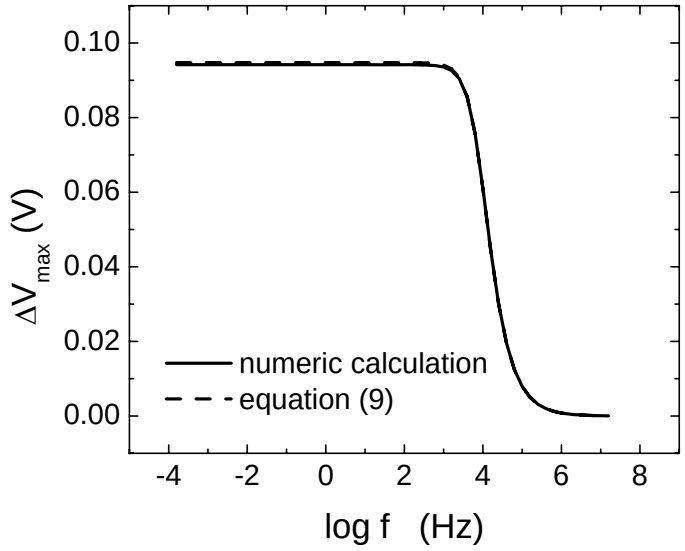

Figure 3-6. Maximum variation of the interfacial potential signal as a function of frequency for parameters $\Delta U = 100$ mV, $R_{\mathrm{e}} = 1\ \Omega\mathrm{cm}^2$, $C_{\mathrm{dl}} = 20\ \mu\mathrm{F/cm}^2$, $R_{\mathrm{t},0} = 26\ \Omega\mathrm{cm}^2$. The solid curve is $\Delta V_{\max}$ resulting from the numeric simulation. The dashed curve is ΔV predicted from equation (3–9) using $R_{\mathrm{t,obs}} = 19\ \Omega\mathrm{cm}^2$, which decreases from the linear value, $R_{\mathrm{t},0} = 26\ \Omega\mathrm{cm}^2$, due to the large input perturbation.

Inspection of the low-frequency and high-frequency limits of equation (3–9) provides insight into the conditions at which ideal linearity are approached, *i.e.,*

$$\lim_{\omega \to 0} \Delta V = \frac{\Delta U R_{\mathrm{t,obs}}}{R_{\mathrm{t,obs}} + R_{\mathrm{e}}} \tag{3–38}$$

and

$$\lim_{\omega \to \infty} \Delta V = \frac{\Delta U}{\omega C_{\mathrm{dl}} R_{\mathrm{e}}} \tag{3–39}$$

respectively, where $R_{\mathrm{t,obs}}$ is the observed charge-transfer resistance at the given perturbation amplitude. Although equations (3–38) and (3–39) are derived for the linear system, the results shown in Figure 3-6 confirms that these equations are useful for approximating $\Delta V_{\max}$, as long as the charge-transfer resistance R_{t} is replaced by the charge-transfer resistance influenced by a nonlinear response $R_{\mathrm{t,obs}}$. As shown in equation (3–38), $\Delta V_{\max}$ decreases in the low-frequency range with increasing Ohmic resistance. As shown in equation (3–39), $\Delta V_{\max}$ decreases in the high-frequency range

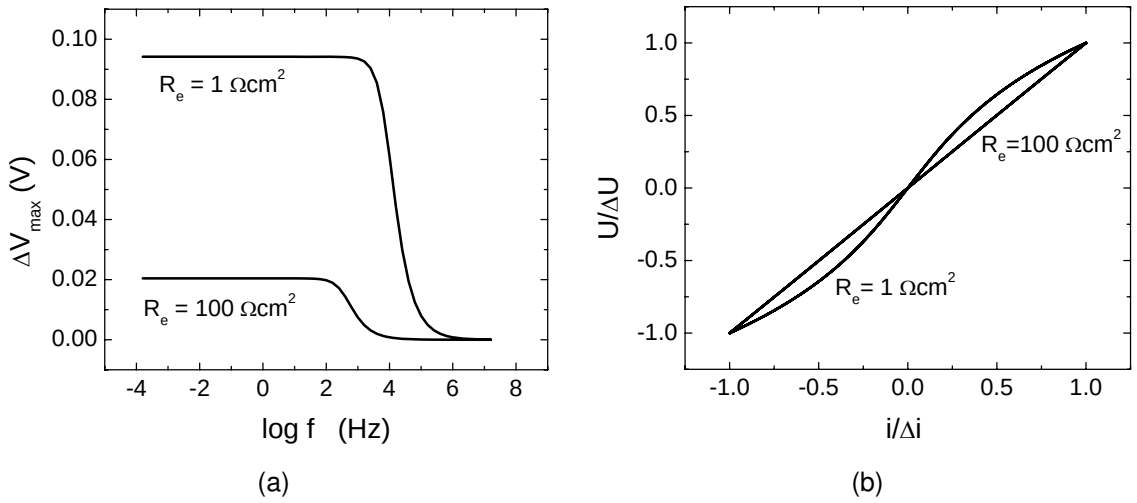

Figure 3-7. Calculated results for parameters $\Delta U = 100$ mV, $C_{\rm dl} = 20\ \mu$F/cm^2, and $R_{\rm t,0} = 26\ \Omega$cm^2 with Ohmic resistance as a parameter. a) Maximum variation of the interfacial potential signal as a function of frequency; and b) the corresponding Lissajous plots at a frequency of 0.016 Hz.

with increasing frequency. Both the limits of high Ohmic resistance and high frequency approach the condition of ideal linearity.

The frequency dependence of $\Delta V_{\rm max}$ and the corresponding Lissajous plots are shown in Figures 3-7(a) and 3-7(b), respectively. As shown in the Figures 3-7(a) and 3-7(b), a linear response is obtained for a 100 mV input amplitude when the Ohmic resistance is large; whereas, a nonlinear response is seen for the same perturbation amplitude when the Ohmic resistance is small. This result is consistent with equation (3–37). The linearity of the system response is governed by the value of $\Delta V_{\rm max}$.

A characteristic frequency for the transition from the low-frequency behavior to the high-frequency behavior was obtained as

$$f_t = \frac{1}{2\pi R_{\rm t,obs} C_{\rm dl}} + \frac{1}{2\pi R_{\rm e} C_{\rm dl}} = \frac{1}{2\pi R_{\rm t,obs} C_{\rm dl}} \left[1 + \frac{R_{\rm t,obs}}{R_{\rm e}} \right] \tag{3–40}$$

where f_t is the inflection point of $\Delta V_{\rm max}$ versus frequency, as shown in Figure 3-8. This frequency marks the transition from low-frequency nonlinear behavior to high-frequency linear behavior.

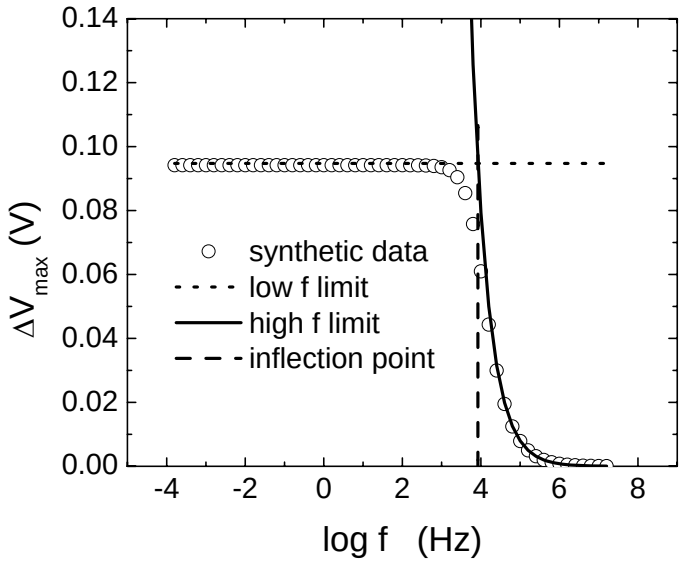

Figure 3-8. Inflection point of $\Delta V_{\max}$ is located at the transitional frequency defined by equation (3–40) ($\Delta U = 100$ mV, $R_{\mathrm{e}} = 1\ \Omega\mathrm{cm}^2$, $C_{\mathrm{dl}} = 20\ \mu\mathrm{F/cm}^2$, and $R_{\mathrm{t},0} = 26\ \Omega\mathrm{cm}^2$).

The low-frequency limit given by equation (3–38) is equivalent to that derived by Darowicki (see *e.g.,* equation (16) in Darowicki[83]). The advantage of using equation (3–9) is that it approximates the interfacial potential across all frequencies while providing a much simpler expression than those derived by the series expansion approach used by Darowicki.

The charge-transfer resistance was calculated using equation (3–11) for each time-dependent value of V generated during the development of synthetic data. At each frequency, the charge-transfer resistance was averaged over a complete sinusoidal cycle yielding the effective charge-transfer resistance, which at low frequency is approximately the observed charge-transfer resistance $R_{\mathrm{t,obs}}$. The consequence of the change in interfacial potential with frequency is illustrated in Figures 3-9(a) and 3-9(b) for parameters $R_{\mathrm{e}} = 1\ \Omega\mathrm{cm}^2$, $C_{\mathrm{dl}} = 20\ \mu\mathrm{F/cm}^2$, and $R_{\mathrm{t},0} = 26\ \Omega\mathrm{cm}^2$ with applied perturbation amplitude as a parameter. At low frequencies, the effective charge-transfer resistance decreases with increased input amplitude as expected. At higher frequencies, however, the effective charge-transfer resistance approaches the expected value. As described by

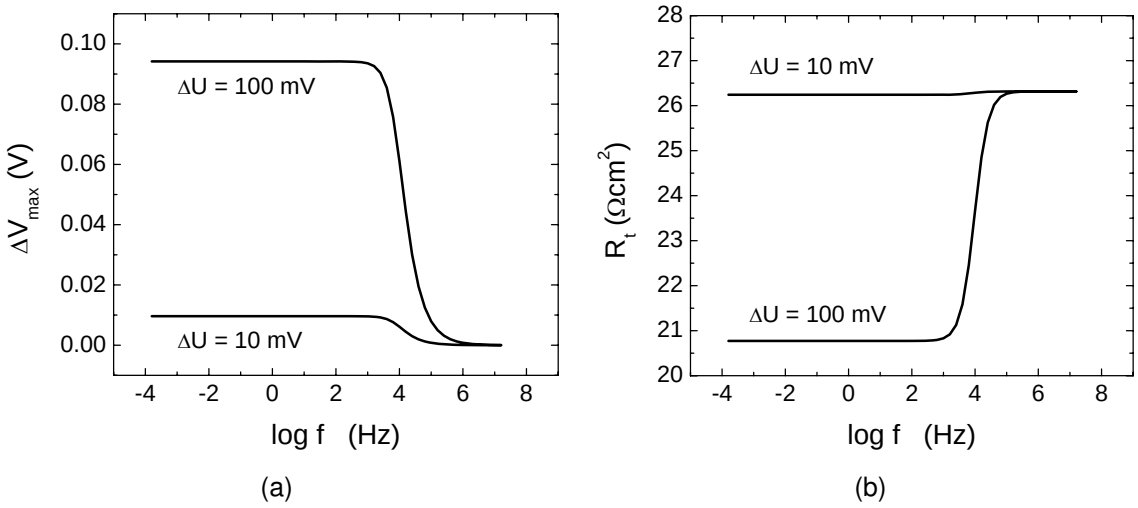

Figure 3-9. Calculated results for parameters $R_{\mathrm{e}} = 1\ \Omega\mathrm{cm}^2$, $C_{\mathrm{dl}} = 20\ \mu\mathrm{F/cm}^2$, and $R_{\mathrm{t},0} = 26\ \Omega\mathrm{cm}^2$ with applied perturbation amplitude as a parameter: a) Maximum variation of the interfacial potential signal as a function of frequency; and b) The effective charge-transfer resistance as a function of frequency.

equation (3–40), $\Delta V_{\max}$ changes value at the transition frequency. Correspondingly, the effective charge-transfer resistance changes value at this transitional frequency. For the 100 mV perturbation the variation in the charge-transfer resistance is significant. For the 10 mV perturbation the variation is negligible. In the presence of an Ohmic resistance $\Delta V_{\max}$ is damped in the limit of high frequency and the values for the charge-transfer resistance will be superimposed.

The effective charge-transfer resistance is given in Figure 3-10(a) as a function of frequency for different values of Ohmic resistance and input amplitudes. The validity of equation (3–40) is confirmed by the superposition of the curves presented in Figure 3-10(b) where the normalized effective charge-transfer resistance is presented as functions of normalized frequency.

3.3.5 Optimization of the Input Signal

The results presented in Figure 3-10(b) suggest that an optimized protocol can be established for systems with Ohmic resistance. A smaller perturbation amplitude can be

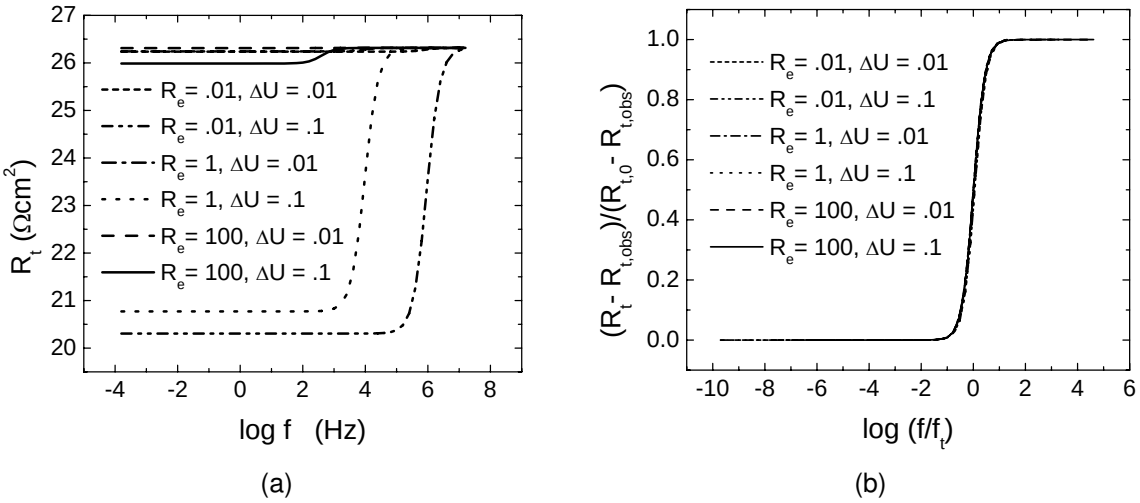

Figure 3-10. Effective charge-transfer resistance as a function of frequency: a) the effective charge-transfer resistance for different Ohmic resistances and input amplitudes; and b) the dimensionless form of the effective charge-transfer resistance versus dimensionless frequency.

employed at frequencies below the transition frequency defined by equation (3–40), and a larger amplitude can be employed at frequencies above the transition frequency.

As shown in Figure 3-10(a), at moderate to large values of Ohmic resistance the transition frequency defined by equation (3–40) is well within the experimentally assessable range. Large amplitude inputs can be employed at frequencies above the transition frequency due to the dampening of the interfacial potential. For large values of Ohmic resistance the second term in equation (3–37) becomes significant and influences selection of the appropriate input potential amplitude.

To illustrate the concept, an electrochemical system was modeled for which the electrolytic resistance was twice the value of the charge-transfer resistance. A constant baseline noise of 20 percent of the low-frequency current signal was added to the current signal. The resulting impedance response to the 10 mV input perturbation employed in common practice is presented in Figure 3-11(a). Substantial scatter is observed at all frequencies.

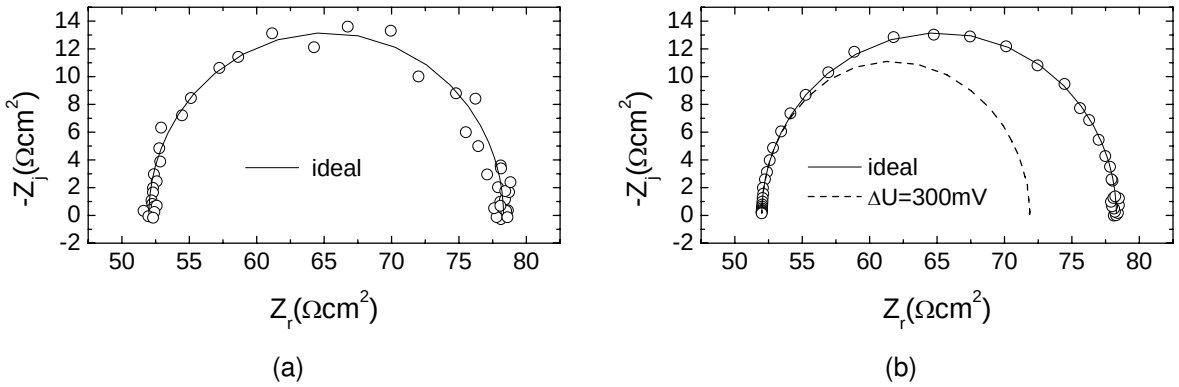

Figure 3-11. System with $R_{\mathrm{e}} = 2R_{\mathrm{t}}$ and baseline noise that is constant at 20 percent of low frequency current signal. a) $\Delta U = 10$ mV for all ω. b) $\Delta U = 30$ mV for $\omega < 10\omega_t$ and $\Delta U = 300$ mV for $\omega > 10\omega_t$.

The input signal can be modified in two ways. In the low-frequency limit (equation (3–38)), when $R_{\mathrm{e}} = 2R_{\mathrm{t}}$, the experimentalist can use three times the input amplitude signal and still achieve an adequate linear response. In the high-frequency limit (equation (3–39)), $\Delta V_{\max}$ is damped to zero and, accordingly, a much higher input amplitude signal can be used. The impedance response given in Figure 3-11(b) was obtained when a 30 mV voltage perturbation was introduced into the system for frequencies less than ten times the transitional frequency and a 300 mV perturbation was introduced for frequencies greater than 10 times the transitional frequency. The dashed line shows the impedance response that would have resulted if the 300 mV perturbation amplitude was employed for all frequencies. The scatter was significantly reduced using the input signal employed for Figure 3-11(b). The variable-amplitude method yields more accurate results and provides a higher confidence for the extraction of system parameters.

3.3.6 Potential-Dependent Capacitance

A constant double layer capacitance was used for the purposes of this work. In general, the capacitance is a function of potential. In the presence of a significant Ohmic resistance, the dampening of the interfacial potential above the transition frequency defined by equation (3–40) allows for adequate linearization of capacitance when the

capacitive current dominates. For sufficiently low Ohmic resistance, the interfacial potential will not be damped and extraction of capacitance values may be compromised due to nonlinear effects.

3.4 Conclusions

The amplitude of the input potential perturbation used for impedance measurements, normally fixed at a value of 10 mV for all systems, should instead be adjusted for each experimental system. If system parameters such as Tafel slope, charge transfer resistance, and Ohmic resistance are known, equation (3–37) provides a useful guide for selection of perturbation amplitude at low frequencies. The transition frequency defined by equation (3–40) can be used to tailor a frequency-dependent input signal. When these parameters are unknown, distortions of low-frequency Lissajous plots are associated with perturbation amplitudes that are too large to ensure a linear response. Assessment of data that may be influenced by nonlinear effects is discussed in Chapter 4.

CHAPTER 4
THE SENSITIVITY OF THE KRAMERS-KRONIG RELATIONS TO NONLINEAR RESPONSES

Prior to interpreting impedance data for model development it is critical that the obtained data is representative of the system that was intended for investigation. Due to the transient and nonlinear nature of electrochemical systems impedance data must be verified for consistency. A system that is changing within the time frame of an experiment, for example due to the growth of a surface film, will yield inconsistent results. For such a system, interpretation of the results will be misleading and conclusions drawn from the data may be erroneous.

In addition to transient behavior, the inherent nonlinear nature of electrochemical systems may also lead to erroneous evaluation of impedance spectra. The current and potential signals obtained from an EIS experiment are interpreted in terms of linear transfer-function theory. Therefore, a response distorted due to the inherent nonlinear nature of a system results in an error induced impedance spectra when linear transfer-function theory is applied. In Chapter 3, the optimization of experimental design for maximizing signal-to-noise ratio while maintaining a linear response was discussed. However, impedance data still demands verification for conformity with the linearity requirement prior to model development. In the present chapter, an evaluation of the tools available to the experimentalist for assessing the linearity requirement is provided.

The Kramers-Kronig relations, which apply strictly for systems that are linear, stable, and causal, provide an essential tool for assessing the internal consistency of impedance data. The Kramers-Kronig relations are understood to be sensitive to failures of causality, but insensitive to failures of linearity. Numerical simulations were performed to explore the conditions under which the Kramers-Kronig relations are sensitive to nonlinear behavior of electrochemical systems. The characteristic transition frequency, identified in Section 3.3.4 as a useful guide for tailoring a frequency-dependent input signal, also has utility for determining the sensitivity of the Kramers-Kronig relations

to nonlinear behavior. Below the transition frequency the Kramers-Kronig relations are satisfied, even for very nonlinear systems. This result is observed for systems with a small Ohmic resistance. The Kramers-Kronig relations are not satisfied for measurements which include the transition frequency. For systems with a large Ohmic resistance, the Kramers-Kronig relations may provide a better tool for assessing the presence of nonlinear behavior as compared to analysis of low-frequency Lissajous plots.

4.1 Application of the Kramers-Kronig Relations

The development of the impedance responses from the nonlinear systems shown in Figures 3-1(a) and 3-1(b) is described in Section 3.1. The simulated impedance data was tested for compliance with the Kramers-Kronig relations using measurement model analysis. The procedure for determination of Kramers-Kronig consistency recommended by Agarwal *et al.* is to fit the imaginary component of impedance data to a measurement model of sequential Voigt elements and then predict the real component of impedance from the extracted parameters.[58–61,84] In the present work, the frequency-dependent charge-transfer resistance that results from the influence of nonlinearity prevented accurate regression of the data to the imaginary-only component. As a result of this limitation, the analysis in Section 4.2 is based on best-fit complex regression of simulated impedance data to a measurement model. Sequential Voigt elements are added to the measurement model until the addition of an element does not result in an improvement of the fit within a 95 percent confidence. Since the measurement model is inherently consistent with the Kramers-Kronig transforms, data that fall within the confidence interval of a regressed model have transformed successfully. Nonconformity with the measurement model indicates noncompliance and, therefore, violation of linearity.

In addition to the measurement model analysis, the simulated impedance data was tested for compliance with the Kramers-Kronig transformations directly. The form of the

Table 4-1. Simulation results used to explore the role of the Kramers-Kronig relations for nonlinear systems with parameters: $\Delta U = 100$ mV, $C_{\rm dl} = 20$ μF/cm^2, $K_a = K_c = 1$ mA/cm^2, $b_a = b_c = 19$ V^{-1}, and $\overline{V} = 0$ V.

$R_{\rm e}$ Ωcm^2	$R_{\rm t,0}$ Ωcm^2	ΔU^*	$R_{\rm t,obs}$ Ωcm^2	$R_{\rm t,obs}/R_{\rm t,0}$	$R_{\rm e}/R_{\rm t,obs}$
0	26.3	9.50	17.3	0.658	0
.01	26.3	9.50	17.3	0.658	5.8×10^{-4}
1	26.3	9.15	18.0	0.684	5.6×10^{-2}
100	26.3	1.98	25.8	0.981	3.9

Kramers-Kronig integrals used is given by

$$Z_r(\omega) = Z_{r,\infty} - \frac{2}{\pi}\int_0^\infty \frac{xZ_j(x) - \omega Z_j(\omega)}{x^2 - \omega^2}dx \tag{4–1}$$

where $Z_j(\omega)$ is an analytic function of the imaginary component of impedance and $Z_{r,\infty}$ is an adjustable parameter representing the value of the Ohmic resistance. The utility of equation (4–1) is that the real component of impedance $Z_r(\omega)$ can be predicted from an analytical function of the imaginary component if the conditions of linearity, stability, and causality are not violated. The integral expressed in equation (4–1) was evaluated by inserting the imaginary component $Z_j(x)$ of the simulated nonlinear impedance data into the integrand and then performing a numerical integration at each frequency. This allowed for the prediction of the real component $Z_r(\omega)$. The test for data compliance was achieved by comparing the predicted value from equation (4–1) to the real component of the simulated data.

4.2 Simulation Results

The simulation results used to explore the role of the Kramers-Kronig relations for nonlinear systems are summarized in Table 4-1. For each simulation, the system parameters gave rise to a linear charge-transfer resistance $R_{\rm t,0} = 26.3$ Ωcm^2. The Ohmic resistance $R_{\rm e}$ was varied from 0 to 100 Ωcm^2. Equation (3–37) can be used to define a scaled potential perturbation as

$$\Delta U^* = \frac{\Delta U}{0.2\sqrt{\frac{K_a b_a + K_c b_c}{K_a b_a^3 + K_c b_c^3}}\,(1 + R_{\rm e}/R_{\rm t,obs})} \tag{4–2}$$

where a value $\Delta U^* = 1$ yields an almost linear response, resulting in an error of less than 0.5 percent in the measured charge transfer resistance, and $R_{\mathrm{t,obs}}$ is the observed charge-transfer resistance measured at low frequency. The values of the scaled potential perturbation given in Table 4-1 reflect the influence of Ohmic resistance on the interfacial potential $\Delta V_{\max}$ resulting from an applied potential ΔU. As discussed extensively in the literature,[75,65,62,64,66–70] the large potential perturbation causes an error in the observed charge-transfer resistance. The magnitude of the effect can be assessed by using the dimensionless ratio $R_{\mathrm{t,obs}}/R_{\mathrm{t},0}$. The magnitude of the induced errors depends on the Ohmic resistance,[75] *i.e.,* the ratio $R_{\mathrm{t,obs}}/R_{\mathrm{t},0}$ approaches unity as $R_{\mathrm{e}}/R_{\mathrm{t,obs}}$ increases. The error in the impedance response caused by a large input signal is shown in Figure 3-2 for the simulations with $R_{\mathrm{e}} = 1\ \Omega\mathrm{cm}^2$.

Simulated data generated from the systems presented in Table 4-1 were analyzed for consistency with the Kramers-Kronig relations. Under these conditions, the introduced input amplitude of $\Delta U = 100$ mV caused significant errors in the impedance response. The simulated data were analyzed using both the measurement model approach and direct evaluation of the Kramers-Kronig integrals, as described in Section 4.1.

The residual errors resulting from a measurement model fit to simulated impedance data generated from the system with no Ohmic resistance $R_{\mathrm{e}} = 0$ are shown in Figures 4-1(a) and 4-1(b) for the real and imaginary parts, respectively. The dashed line represents the confidence interval for the regressed model. All of the residual errors fell within the confidence interval, suggesting that the Kramers-Kronig relations were satisfied. The magnitude of the residuals, on the order of 10^{-13}, show that the measurement model could fit the data to within 12 significant digits. The data were shown to satisfy the Kramers-Kronig relations, even though the errors due to a nonlinear response were very large, *i.e.,* $R_{\mathrm{t,obs}}/R_{\mathrm{t},0}$ = 0.658.

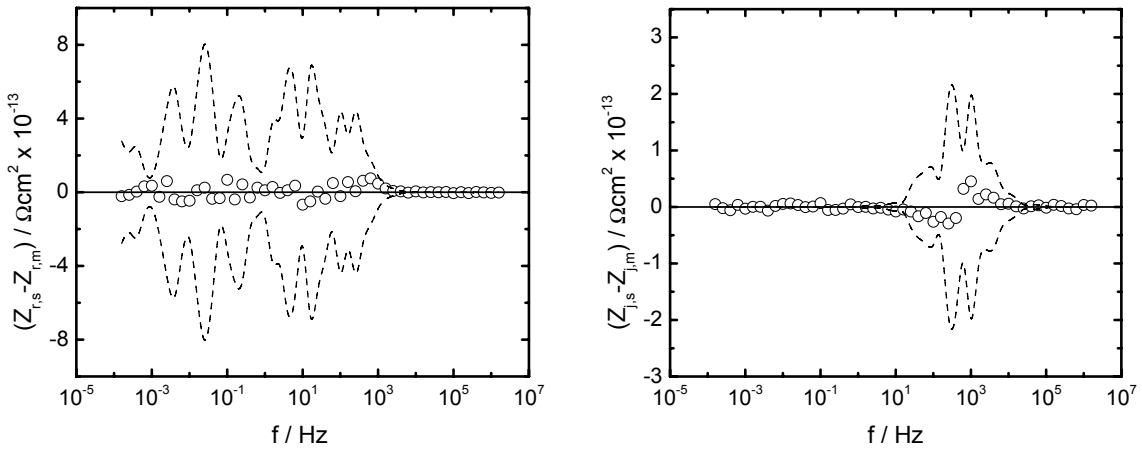

Figure 4-1. Residuals errors resulting from a measurement model fit $Z_{\rm m}$ to simulated data $Z_{\rm s}$ for the system with $R_{\rm e} = 0\ \Omega$cm^2: a) real part; and b) imaginary part. The lines correspond to the 95.4% **(2σ)** confidence interval for the regression. The system parameters presented in Table 4-1 give rise to $R_{\rm t,obs}/R_{\rm t,0}$ = 0.658 and $R_{\rm e}/R_{\rm t,obs}$ = 0.

The real and imaginary parts of the normalized residual errors resulting from a measurement model fit to simulated impedance data generated from the system with $R_{\rm e} = .01\ \Omega$cm^2 are shown in Figures 4-2(a) and 4-2(b), respectively. The residual errors fell outside the confidence interval at frequencies greater than 10^5 Hz. The scaled values of 10^{-4} at high frequencies shows that the deviations from Kramers-Kronig relations are in the fourth significant digit, which may not be visible for experimental data. Nevertheless, the simulation results do not conform to the Kramers-Kronig transforms.

The real and imaginary parts of the normalized residual errors resulting from a measurement model fit to simulated impedance data generated from the system with $R_{\rm e} = 1\ \Omega$cm^2 are shown in Figures 4-3(a) and 4-3(b), respectively. The deviation from consistency with the Kramers-Kronig relations, marked by residual errors that fall outside the confident interval for the regressed model, are evident for frequencies greater than 10^3 Hz. The magnitude of the scaled residual errors is larger than seen in

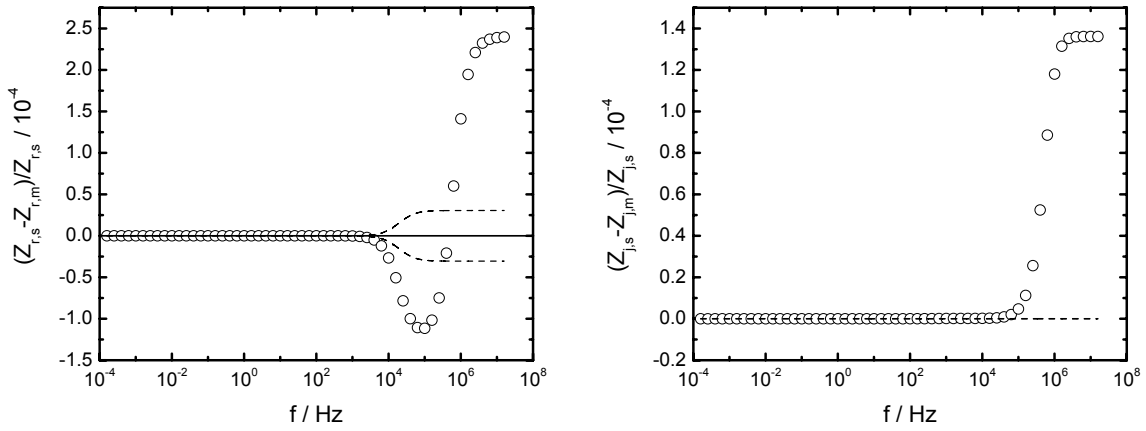

Figure 4-2. Normalized residual errors resulting from a measurement model fit $Z_{\rm m}$ to simulated impedance data $Z_{\rm s}$ for the system with $R_{\rm e} = .01\ \Omega$cm^2: a) real part; and b) imaginary part. The lines correspond to the 95.4% confidence interval for the regression. The system parameters presented in Table 4-1 give rise to $R_{\rm t,obs}/R_{\rm t,0}$ = 0.658 and $R_{\rm e}/R_{\rm t,obs} = 5.8 \times 10^{-4}$.

Figure 4-2. In addition, the residual errors fall outside the confidence interval at a lower frequency as compared to Figure 4-2.

The residual errors resulting from a measurement model fit to simulated impedance data generated from the system with $R_{\rm e} = 100\ \Omega$cm^2 are shown in Figures 4-4(a) and 4-4(b). Due to the large Ohmic resistance, the error due to nonlinearity was small, *i.e.,* $R_{\rm t,obs}/R_{\rm t,0}$ = 0.981. Nevertheless, the normalized residual errors fell outside the confidence interval for all frequencies.

The measurement model analysis of consistency with the Kramers-Kronig relations presented in Figures 4-1, 4-2, 4-3, and 4-4 was complemented by an independent analysis using direct evaluation of the Kramers-Kronig integral equation (4–1). As shown in Figure 4-5, the real part of the impedance predicted from equation (4–1) was in perfect agreement with the simulation value for the system with no Ohmic resistance $R_{\rm e} = 0\ \Omega$cm^2. This result is in agreement with the result presented in Figure 4-1, showing that even a very nonlinear impedance response yielding $R_{\rm t,obs}/R_{\rm t,0}$ = 0.658 is consistent with the Kramers-Kronig relations for an Ohmic resistance equal to zero.

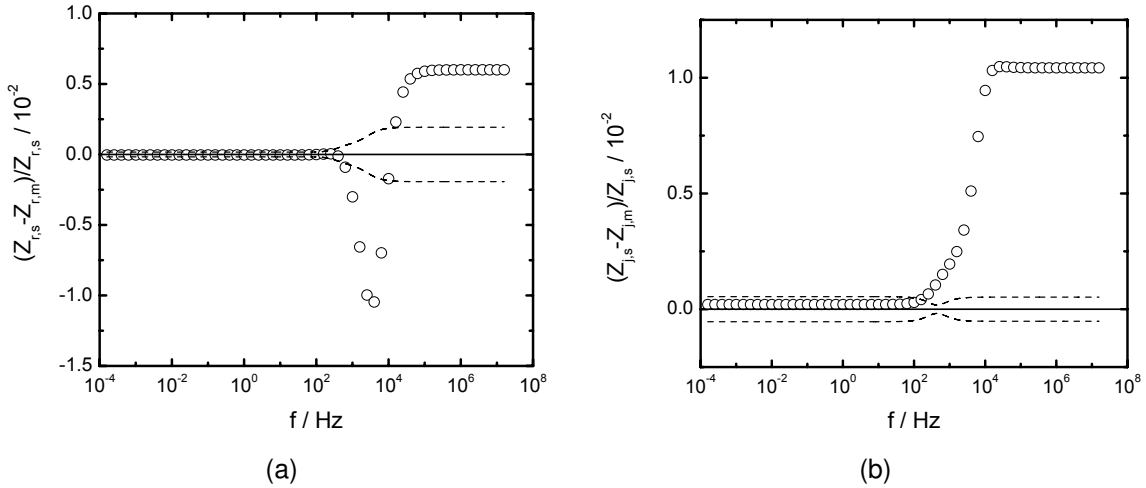

Figure 4-3. Normalized residual errors resulting from a measurement model fit Z_{m} to simulated impedance data Z_{s} for the system with $R_{\mathrm{e}} = 1\ \Omega\mathrm{cm}^2$: a) real part; and b) imaginary part. The lines correspond to the 95.4% confidence interval for the regression. The system parameters presented in Table 4-1 give rise to $R_{\mathrm{t,obs}}/R_{\mathrm{t},0}$ = 0.684 and $R_{\mathrm{e}}/R_{\mathrm{t,obs}} = 5.6 \times 10^{-2}$.

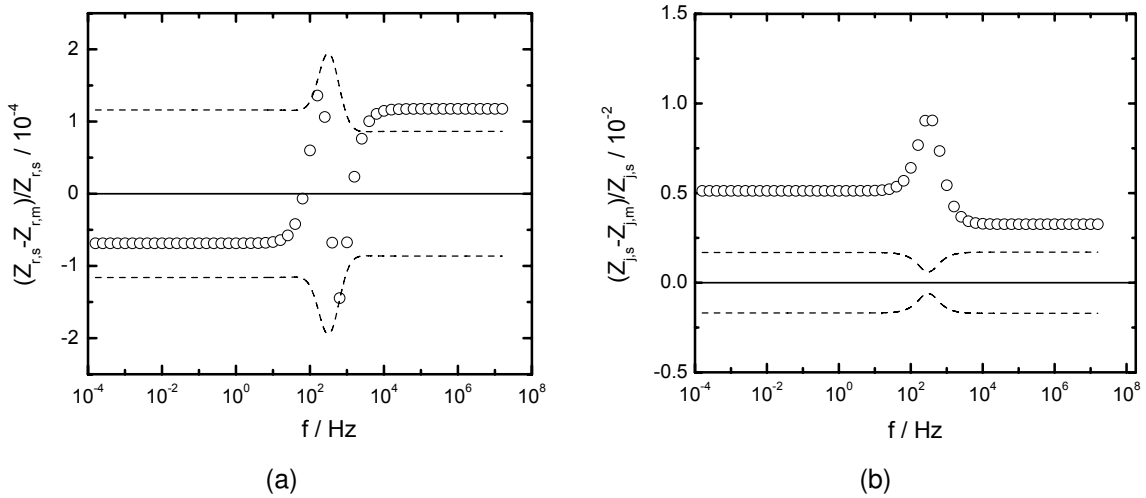

Figure 4-4. Normalized residual errors resulting from a measurement model fit Z_{m} to simulated impedance data Z_{s} for the system with $R_{\mathrm{e}} = 100\ \Omega\mathrm{cm}^2$: a) real part; and b) imaginary part. The lines correspond to the 95.4% confidence interval for the regression. The system parameters presented in Table 4-1 give rise to $R_{\mathrm{t,obs}}/R_{\mathrm{t},0}$ = 0.981 and $R_{\mathrm{e}}/R_{\mathrm{t,obs}}$ = 3.9.

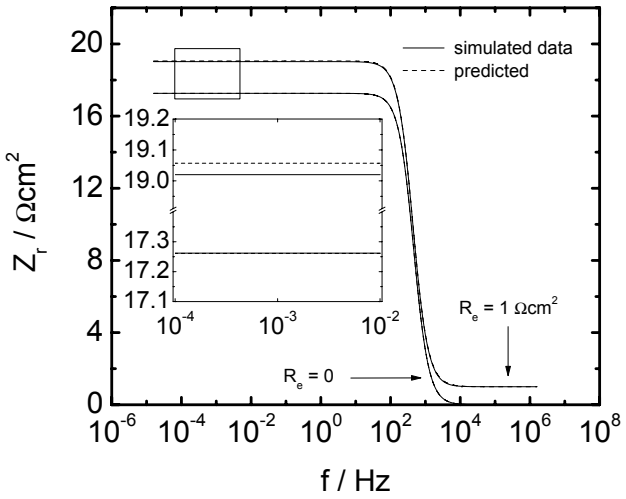

Figure 4-5. A comparison of simulation results to the real component of impedance predicted using equation (4–1) for the systems with $R_e = 0\ \Omega\text{cm}^2$ and $R_e = 1\ \Omega\text{cm}^2$. The system parameters presented in Table 4-1 give rise to $R_{t,obs}/R_{t,0}$ = 0.658 and $R_{t,obs}/R_{t,0}$ = 0.684, respectively. In the absence of Ohmic resistance, the simulated data and the predicted values are equal.

For the system with $R_e = 1\ \Omega\text{cm}^2$, the real component of impedance predicted from equation (4–1) deviated from the real component of the simulated data, indicating noncompliance with the Kramers-Kronig transforms due to violation of linearity. This result is in agreement with the results presented in Figure 4-3.

The direct integration of equation (4–1) was also able to reveal an inconsistency with the Kramers-Kronig relations for the system with $R_e = 100\ \Omega\text{cm}^2$ system, as is shown in Figure 4-6. The percent error in the low frequency region, corrected for Ohmic resistance, is 4 times greater for the $R_e = 100\ \Omega\text{cm}^2$ system as compared to the $R_e = 1\ \Omega\text{cm}^2$ system shown in Figure 4-5. For the system with $R_e = .01\ \Omega\text{cm}^2$, however, direct integration of equation (4–1) did not reveal the inconsistencies with the Kramers-Kronig relations shown by the measurement model analysis in Figure 4-2. This discrepancy may be regarded to be a testimony to the sensitivity of the measurement model analysis for failures of consistency with the Kramers-Kronig relations.

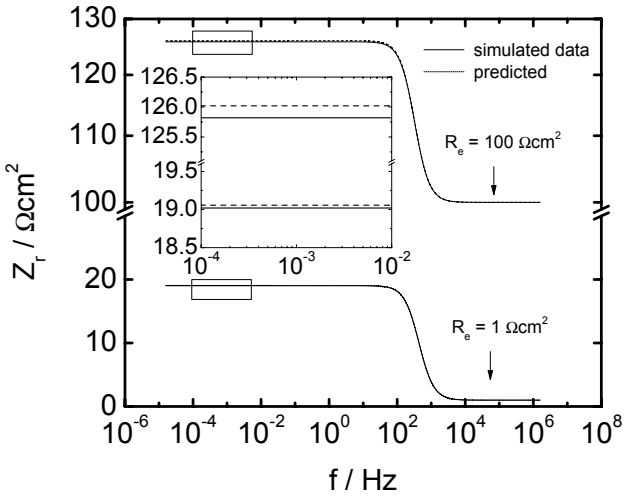

Figure 4-6. A comparison of simulation results to the real component of impedance predicted using equation (4–1) for the systems with $R_{\mathrm{e}} = 1\ \Omega\mathrm{cm}^2$ and $R_{\mathrm{e}} = 100\ \Omega\mathrm{cm}^2$. The system parameters presented in Table 4-1 give rise to $R_{\mathrm{t,obs}}/R_{\mathrm{t},0}$ = 0.684 and $R_{\mathrm{t,obs}}/R_{\mathrm{t},0}$ = 0.981, respectively.

4.3 The Applicability of the Kramers-Kronig Relations to Detecting Nonlinearity

The sensitivity of the Kramers-Kronig transforms to nonlinearity clearly depends on both the magnitude of the errors $R_{\mathrm{t,obs}}/R_{\mathrm{t},0}$ and on the Ohmic resistance. The objective of the following section is to identify the conditions under which the Kramers-Kronig relations may detect errors caused by a nonlinear impedance response.

4.3.1 Influence of Transition Frequency

The maximum variation of interfacial potential $\Delta V_{\max}$ corresponding to an input perturbation $\Delta U = 0.1$ V is given in Figure 4-7(a) for the simulations presented in Table 4-1. One influence of the Ohmic resistance is seen at low frequencies, where

$$\lim_{\omega \to 0} \Delta V_{\max} = \frac{\Delta U}{(1 + R_{\mathrm{e}}/R_{\mathrm{t,obs}})} \tag{4–3}$$

The presence of the Ohmic resistance further decreases the perturbation amplitude at higher frequencies where the interfacial impedance becomes small and the role of the Faradaic current is diminished.

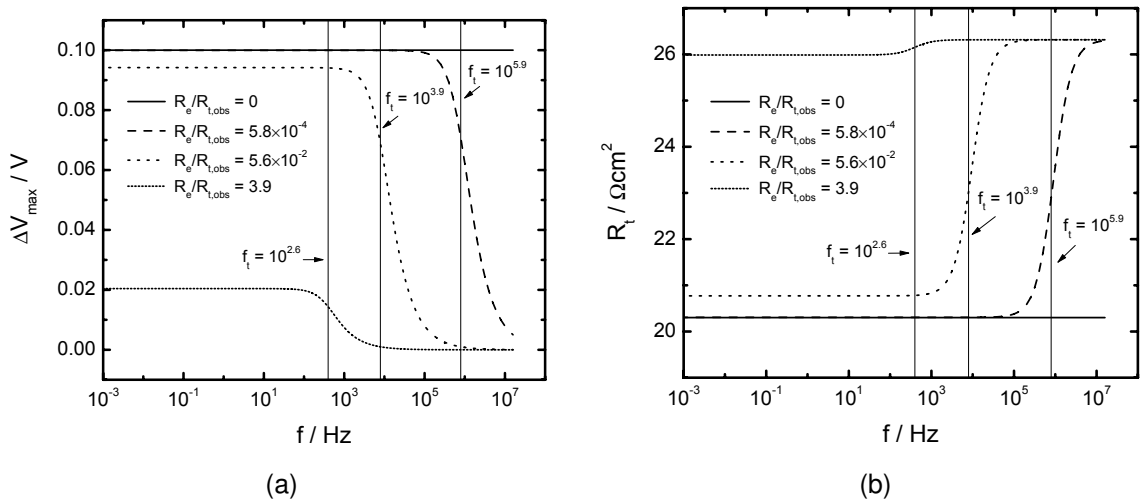

Figure 4-7. Interfacial parameters as functions of frequency for the simulations presented in Table 4-1: a) Maximum variation of the interfacial potential; and b) the effective charge-transfer resistance. Vertical lines correspond to the transition frequency given by equation (3–40).

As discussed in Section 3.3.4, the frequency dependence of the interfacial potential causes a corresponding change in the apparent charge transfer resistance, as shown in Figure 4-7(b). The frequency characteristic of the transformation shown in Figure 4-7 from low-frequency behavior to high-frequency behavior is given by equation (3–40). The transition frequency depends on the dimensionless ratio $R_{\mathrm{t,obs}}/R_{\mathrm{e}}$ and is given in units of Hz.

The influence of the transition frequency can be seen in Figure 4-8 where the normalized real part of the impedance is presented as a function of normalized frequency for the system with $R_{\mathrm{e}} = 1\ \Omega\mathrm{cm}^2$. The frequency is scaled by the frequency characteristic of the $R_{\mathrm{t},0}C$ time constant, and the real part of the impedance is corrected for the Ohmic resistance and scaled by the $R_{\mathrm{t,obs}}$ seen at low frequency. At the transition frequency given by equation (3–40), the effective charge-transfer resistance changes from the low-frequency value $R_{\mathrm{t,obs}}$, which is affected by the nonlinear response, to the linear value $R_{\mathrm{t},0}$.

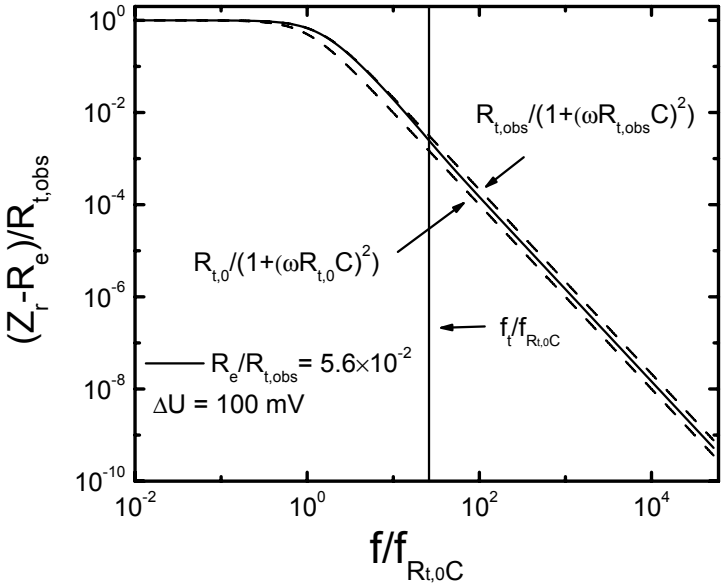

Figure 4-8. The normalized real part of the impedance as a function of normalized frequency for the system with $R_{\mathrm{e}} = 1\ \Omega\mathrm{cm}^2$ (solid line). The dashed lines represent the ideal linear responses for systems with $R_{\mathrm{t},0} = 26.3\ \Omega\mathrm{cm}^2$ and with $R_{\mathrm{t,obs}} = 18.0\ \Omega\mathrm{cm}^2$.

The change in apparent charge-transfer resistance has an influence as well in the imaginary part of the impedance. The normalized impedance responses are presented as functions of normalized frequency for the systems with $R_{\mathrm{e}} = 0.01$, 1, and $100\ \Omega\mathrm{cm}^2$ in Figures 4-9(a) and 4-9(b) for the real and imaginary parts, respectively. The solid curve is the ideal linear response and the dashed curves are the nonlinear impedance responses arising from a large input amplitude of $\Delta U = 100$ mV for system parameters presented in Table 4-1. As shown in Figure 4-9(a), the real component of impedance is distorted from the ideal linear response for the $R_{\mathrm{e}} = 1\ \Omega\mathrm{cm}^2$ and $R_{\mathrm{e}} = .01\ \Omega\mathrm{cm}^2$ systems. Distortion is also present for the $R_{\mathrm{e}} = 100\ \Omega\mathrm{cm}^2$ system, however, it is not visually evident in Figure 4-9(a) due to the small deviation of the observed charge-transfer resistance from the linear value, *i.e.,* $R_{\mathrm{t,obs}}/R_{\mathrm{t},0}$ = 0.981. The distortion from the linear response occurs at the transition frequency described by equation (3–40). As shown in Figure 4-9(b), the imaginary component of impedance is distorted from the ideal linear response for the $R_{\mathrm{e}} = 1\ \Omega\mathrm{cm}^2$ and $R_{\mathrm{e}} = 100\ \Omega\mathrm{cm}^2$ systems. Distortion is not

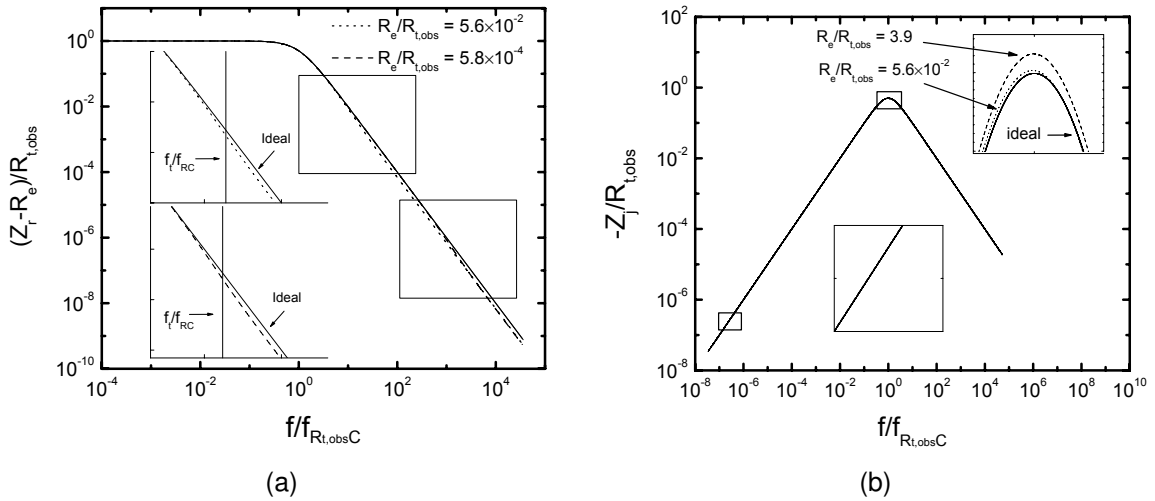

(a) (b)

Figure 4-9. The normalized impedance response as functions of normalized frequency for the systems with $R_{\mathrm{e}} = 0.01$, 1, and $100\ \Omega\mathrm{cm}^2$: a) real part; and b) imaginary part. The solid curve is the ideal linear response and the dashed curves are the nonlinear impedance responses arising from a large input amplitude of $\Delta U = 100$ mV for system parameters presented in Table 4-1.

evident for the $R_{\mathrm{e}} = .01\ \Omega\mathrm{cm}^2$ system. For the case with $R_{\mathrm{e}} = .01\ \Omega\mathrm{cm}^2$ the transition frequency was $f_t = 8 \times 10^5$ Hz which was in the calculated range of frequencies, but the transition to $R_{\mathrm{t},0}$ takes place in a frequency range where the current is predominately charging and the value of the charge-transfer resistance is inconsequential.

In contrast no distortion of the impedance response is seen for the case in which $R_{\mathrm{e}} = 0$. The normalized impedance response for the system with $R_{\mathrm{e}} = 0$ is presented as a function of normalized frequency in Figures 4-10(a) and 4-10(b) for the real and imaginary parts, respectively. Both the ideal linear response and the nonlinear impedance response are superposed in spite of the large potential amplitude applied, yielding a value $R_{\mathrm{t,obs}}/R_{\mathrm{t},0} = 0.658$.

The work presented here demonstrates that the sensitivity of the Kramers-Kronig relations on the nonlinearity of an electrochemical system depends on both the magnitude of the potential perturbation and the value of the transition frequency given by equation (3–40). The critical parameters are ΔU^*, given by equation (4–2), $R_{\mathrm{t,obs}}C_{\mathrm{dl}}$,

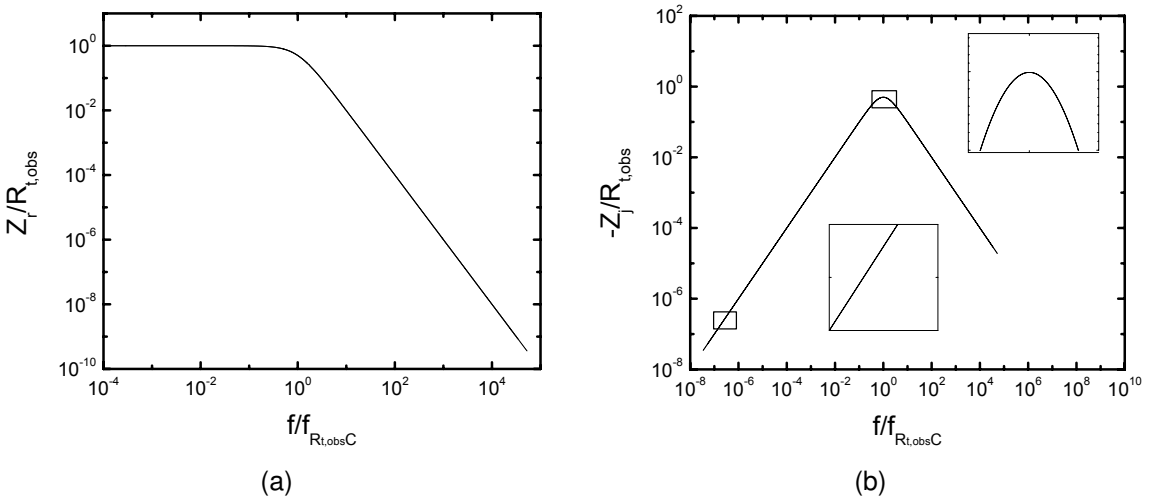

Figure 4-10. The normalized impedance response as functions of normalized frequency for the system with $R_{\mathrm{e}} = 0$: a) real part; and b) imaginary part. Both the ideal linear response and the nonlinear impedance response are superposed.

and $R_{\mathrm{e}}/R_{\mathrm{t,obs}}$. When $R_{\mathrm{e}} = 0$, the transition frequency given by equation (3–40) is equal to infinity, and the impedance response is given by

$$Z = \frac{R_{\mathrm{t,obs}}}{1 + j\omega R_{\mathrm{t,obs}} C} \tag{4–4}$$

where $R_{\mathrm{t,obs}}$ differs from $R_{\mathrm{t},0}$ but is independent of frequency. In this case, the Kramers-Kronig relations are satisfied. When the Ohmic resistance is small and the transition frequency is outside the experimentally assessable range, the effective charge-transfer resistance is approximately independent of frequency, as shown in Figure 4-7(b), and the Kramers-Kronig relations will be satisfied. The Kramers-Kronig relations will also be satisfied if the the departure from linear behavior is sufficiently small that $R_{\mathrm{t,obs}}/R_{\mathrm{t},0} \approx 1$. The Kramers-Kronig relations will be violated for conditions where $R_{\mathrm{t,obs}}/R_{\mathrm{t},0} \neq 1$ and the transition frequency given by equation (3–40) falls within the experimental frequency range. In such a case, the varying effective charge-transfer resistance is the mechanism that causes the Kramers-Kronig relations to fail, just as a time-dependent R_{t} would cause the Kramers-Kronig relations to fail due to violation of the condition of causality.

There exists an interesting balance of effects for the systems with a large Ohmic resistance. The presence of a large Ohmic resistance reduces the portion of the applied potential perturbation that contributes to the interfacial potential, and therefore reduces the departure of $R_{\mathrm{t,obs}}/R_{\mathrm{t},0}$ from unity. At the same time, the transition frequency approaches $1/R_{\mathrm{t,obs}}C_{\mathrm{dl}}$, thus making any departure from linear behavior detectable by use of the Kramers-Kronig relations. In these cases, the use of Lissajous figures at low frequencies may be less sensitive to nonlinear behavior as compared to the use of the Kramers-Kronig relations. For example, the Lissajous analysis of the $R_{\mathrm{e}} = 100\ \Omega\mathrm{cm}^2$ system, shown in Figure 7 of the work by Hirschorn *et al.*,[75] did not detect the presence of nonlinearity, while the Kramers-Kronig analysis shown in Figure 4-6 did detect nonlinear behavior. It should be noted that further increase in the Ohmic resistance will eventually lead to an approximately linear response that is in compliance with the Kramers-Kronig relations.

For small values of Ohmic resistance, the transition frequencies are significantly greater than $1/R_{\mathrm{t,obs}}C_{\mathrm{dl}}$ and the transition to $R_{\mathrm{t},0}$ takes place in a frequency range where the value of the charge-transfer resistance has a negligible influence on the imaginary impedance. Therefore, it will be difficult to detect discrepancies at low frequencies between the data and the predicted values using the Kramers-Kronig transform expressed by equation (4–1). This is in agreement with the results presented in Figure 4-6, where the $R_{\mathrm{e}} = 100\ \Omega\mathrm{cm}^2$ system with $f_t = 4 \times 10^2$ Hz is more sensitive to nonlinear behavior than is the $R_{\mathrm{e}} = 1\ \Omega\mathrm{cm}^2$ system with $f_t = 8 \times 10^3$ Hz.

4.3.2 Application to Experimental Systems

The transition frequency given by equation (3–40) is presented in Figure 4-11 as a function of RC time constant with $R_{\mathrm{e}}/R_{\mathrm{t}}$ as a parameter. The time constant for fast reactions, such as the reduction of ferricyanide on a platinum electrode at an appreciable fraction of the mass-transfer-limited current density, can be on the order of 10^{-5} s. For these systems, the transition frequency may fall outside the experimentally accessible

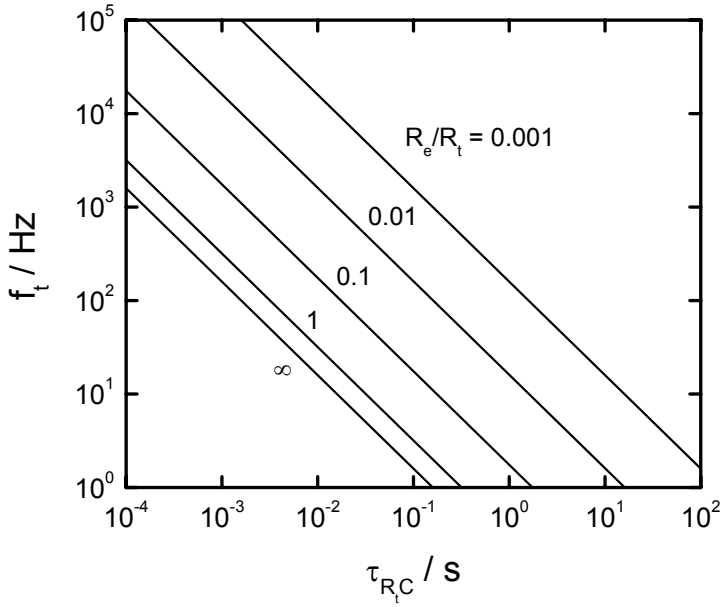

Figure 4-11. The transition frequency given by equation (3–40) as a function of RC time constant with $R_\mathrm{e}/R_\mathrm{t}$ as a parameter.

frequency range. The RC time constant for reactions near the equilibrium potential may, however, be significantly larger. For these systems, the transition frequency may fall within the experimental range, even for small values of $R_\mathrm{e}/R_\mathrm{t}$.

Urquidi-Macdonald *et al.* have reported, based on experimental observations, that the Kramers-Kronig relations are not sensitive to a nonlinear system response.[74] Their conclusions were based on experiments performed with different perturbation amplitudes on an iron electrode in a 1 M $\mathrm{H_2SO_4}$ electrolyte. They found that the Kramers-Kronig relations were satisfied even for potential perturbation amplitudes sufficiently large to cause measurable distortions in the impedance response. Their results can be placed into the context of Figure 4-11. System parameters $R_\mathrm{e} = 2\ \Omega\mathrm{cm}^2$, $C_\mathrm{dl} = 10\ \mu\mathrm{F/cm}^2$, and $R_\mathrm{t,obs} = 14\ \Omega\mathrm{cm}^2$ were estimated from the small-amplitude impedance data from the published experimental results shown in Figure 4 of their work.[74] The corresponding transition frequency was approximately 9000 Hz. Their experimental frequency range extended only to 5000 Hz, as shown in Figure 5 of their work. Therefore, the transition frequency was not in the measured frequency range and

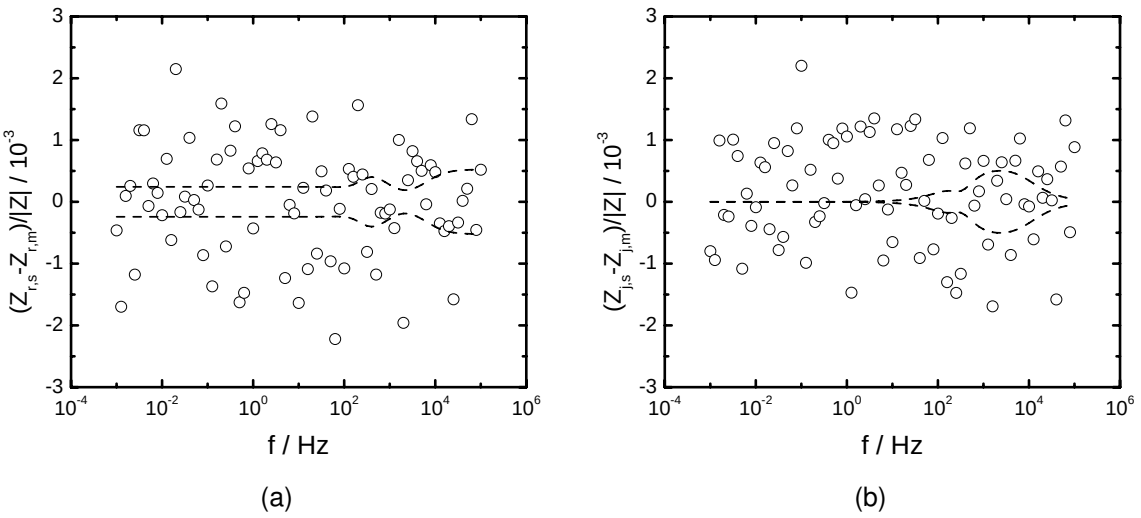

Figure 4-12. Normalized residual errors resulting from a measurement model fit Z_{m} to simulated impedance data Z_{s} with normally distributed additive stochastic errors with standard deviation of 0.1 percent of the modulus for the system with $R_{\mathrm{e}} = 1\ \Omega\mathrm{cm}^2$: a) real part; and b) imaginary part. The lines correspond to the 95.4% confidence interval for the regression. The input potential perturbation amplitude was $\Delta U = 1$ mV.

the measured charge-transfer resistance, although in error due to nonlinearity associated with large perturbation amplitudes, was approximately frequency independent. As a result, the data complied with Kramers-Kronig relations.

It is worth asking, for systems for which the measured frequency range includes the transition frequency, whether the distortions associated with nonlinear behavior are sufficiently large to be discernable in experimental measurements. Normally distributed additive stochastic errors with a mean value of zero and a standard deviation of 0.1 percent of the modulus of the calculated impedance response were applied to the system with $R_{\mathrm{e}} = 1\ \Omega\mathrm{cm}^2$. This level of noise has been reported to be typical of impedance measurements.[85,86] The measurement model analysis for this system with an input potential perturbation amplitude of $\Delta U = 100$ mV was presented in Figure 4-3 in the absence of added noise. The measurement model analysis is presented in Figure 4-12 for simulated data using an input potential perturbation amplitude of $\Delta U = 1$ mV. The normalized residual errors for both real and imaginary parts of the

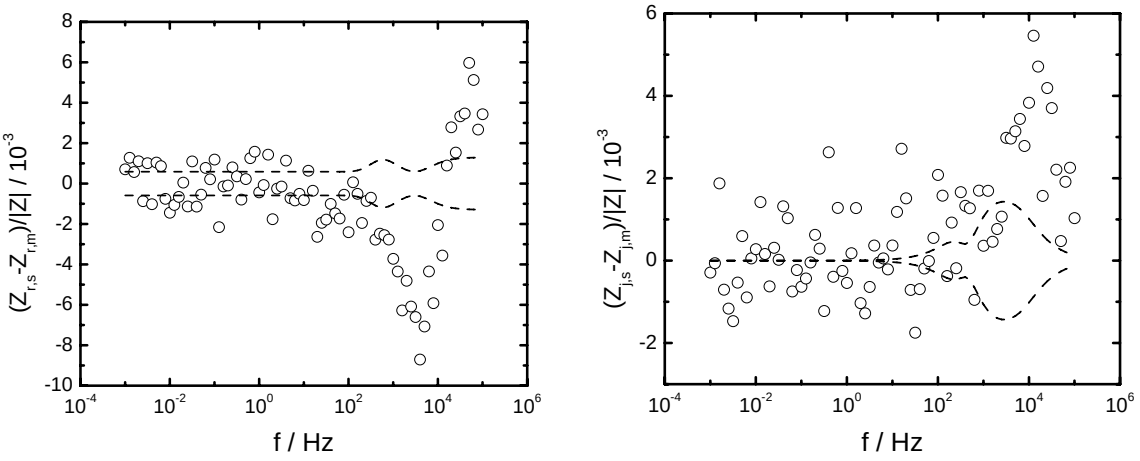

Figure 4-13. Normalized residual errors resulting from a measurement model fit Z_{m} to simulated impedance data Z_{s} with normally distributed additive stochastic errors with standard deviation of 0.1 percent of the modulus for the system with $R_{\mathrm{e}} = 1\ \Omega\mathrm{cm}^2$: a) real part; and b) imaginary part. The lines correspond to the 95.4% confidence interval for the regression. The input potential perturbation amplitude was $\Delta U = 100$ mV.

impedance, shown in Figures 4-12(a) and 4-12(b), respectively, are distributed around zero, indicating that the Kramers-Kronig relations are satisfied.

The corresponding measurement model analysis using an input potential perturbation amplitude of $\Delta U = 100$ mV is presented in Figure 4-13. The normalized residual errors for both real and imaginary parts of the impedance, shown in Figures 4-13(a) and 4-13(b), respectively, are not distributed around zero, indicating that the Kramers-Kronig relations are not satisfied. Thus, a Kramers-Kronig analysis based on the measurement model will detect nonlinearity of systems for which the measured frequency range includes the transition frequency, even when reasonable experimental error is present.

4.4 Conclusions

While the results presented here are consistent with the observations reported by Urquidi-Macdonald *et al.*[74] that the Kramers-Kronig relations were insensitive to failures of linearity, this work also shows that, under appropriate conditions, the Kramers-Kronig relations provide a useful tool for detection of nonlinear system responses. The

sensitivity of the Kramers-Kronig relations on the nonlinearity of an electrochemical system depends on both the magnitude of the potential perturbation and on whether the transition frequency given by equation (3–40) falls within the experimental frequency range. The value of the transition frequency depends on $R_{\mathrm{t,obs}}C_{\mathrm{dl}}$ and $R_{\mathrm{e}}/R_{\mathrm{t,obs}}$. The Kramers-Kronig relations will be violated for conditions where $R_{\mathrm{t,obs}}/R_{\mathrm{t,0}} \neq 1$ and the transition frequency given by equation (3–40) falls within the experimental frequency range.

For small values of $R_{\mathrm{e}}/R_{\mathrm{t,obs}}$, the Kramers-Kronig relations may be of limited utility for detecting errors associated with a nonlinear response. In this case, it will be more appropriate to use experimental tests involving either repeated measurements with different perturbation amplitudes or observation of nonlinear responses in low-frequency Lissajous plots.[7,75] Inspection of Lissajous plots may be less useful for systems with large values of $R_{\mathrm{e}}/R_{\mathrm{t,obs}}$. In this case, the Kramers-Kronig relations may provide a more useful tool for detection of nonlinear responses to large potential perturbations. In Chapter 3, a generalized method for optimizing the implementation of impedance experiments was developed. Confirmation of collected data was presented in the current Chapter. Both experimental techniques and proper data analysis are critical for fitting impedance data and estimating model parameters. The work presented in Chapter 3 and the present chapter provides the foundation for accurately interpreting data in terms of physically meaningful parameters.

CHAPTER 5
CHARACTERISTICS OF THE CONSTANT-PHASE ELEMENT

In Chapters 1 and 2, a background on the use and interpretation of the constant-phase element was provided. In Chapters 3 and 4, a generalized method was developed for optimizing experimental and data analysis techniques for enhancing parameter estimation. In the present chapter, the mathematics of the CPE are reviewed and graphical methods are provided for extracting CPE parameters.

The impedance of the CPE, expressed by equation (1–1), is written in terms its real Z_r and imaginary Z_j components as

$$Z_{\text{cpe}} = \frac{(2\pi f)^{-\alpha}}{Q}\cos(-\alpha\pi/2) + j\frac{(2\pi f)^{-\alpha}}{Q}\sin(-\alpha\pi/2) \tag{5–1}$$

The phase-angle is expressed as

$$\phi_{\text{cpe}} = \arctan\left(\frac{Z_j}{Z_r}\right) = -\frac{\alpha\pi}{2} \tag{5–2}$$

As shown by equation (5–2), the phase-angle does not depend on frequency, which is the origin of the term *constant-phase element*.

For experimental systems the value of α generally ranges between 0.5 and 1. As shown in Figure 5-1, for $\alpha = 1$ the CPE displays a vertical line in the impedance plane, which is representative of the impedance response of an ideal capacitor. When $\alpha < 1$, the impedance response is inclined from the vertical. The smaller the value of α the greater the deviation from the vertical response. The phase-angle with α as a parameter is shown in Figure 5-2.

The real and imaginary components of the CPE as a function of frequency are shown in Figures 5-3(a) and 5-3(b), respectively. As discussed by Orazem *et al.*,[87] and shown by equation (5–1), $d\log|Z_j|/d\log f = -\alpha$. Therefore, the CPE parameter α can be obtained from experimental data as

$$\alpha = \left|\frac{d\log|Z_j|}{d\log f}\right| \tag{5–3}$$

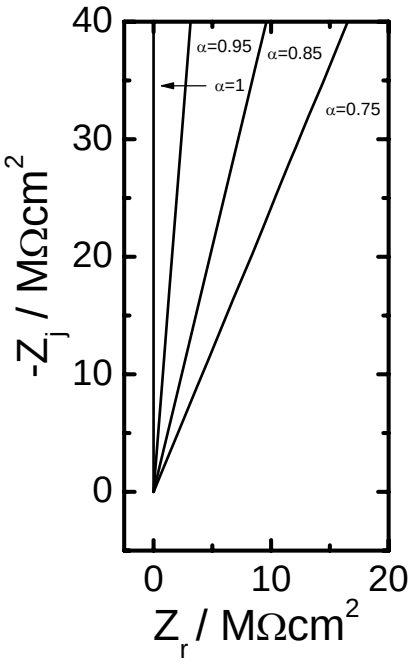

Figure 5-1. Impedance plane representation of the CPE, equation (5–1), with α as a parameter and $Q = 1 \times 10^{-6}$ Fs$^{(\alpha-1)}/\mathrm{cm}^2$.

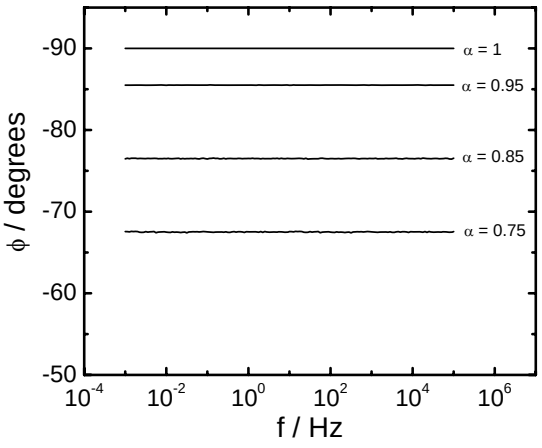

Figure 5-2. The phase-angle associated with the CPE, equation (5–2), with α as a parameter.

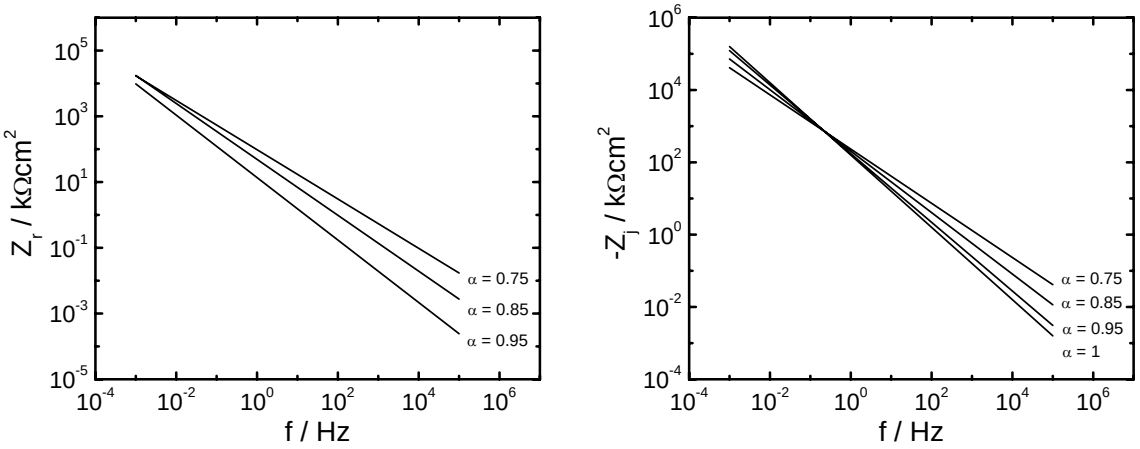

Figure 5-3. Impedance response of the CPE, equation (5–1), with α as a parameter and $Q = 1 \times 10^{-6}$ Fs$^{(\alpha-1)}/\mathrm{cm}^2$; a) the real component; and b) the imaginary component.

and Q can be obtained from

$$Q = \sin(\frac{\alpha\pi}{2})\frac{-1}{Z_j(2\pi f)^{\alpha}} \tag{5–4}$$

The impedance of a reactive system exhibiting the CPE is expressed by equation (1–2). As shown in Figure 5-4, for $\alpha = 1$ the impedance displays a semi-circle in the impedance plane, which is representative of the impedance response of a single time-constant (RC). When $\alpha < 1$, the impedance response is a depressed semi-circle. The smaller the value of α the greater the depression from the ideal semi-circle. The peak of the imaginary component occurs at the characteristic frequency

$$f_c = \frac{1}{2\pi(RQ)^{1/\alpha}} \tag{5–5}$$

The real and imaginary components of the impedance as a function of frequency are shown in Figures 5-5(a) and 5-5(b), respectively. The impedance expressed by equation (1–2) is characterized by a symmetric response about the characteristic frequency expressed by equation (5–5). The value of α can be obtained from experimental data using equation (5–3).

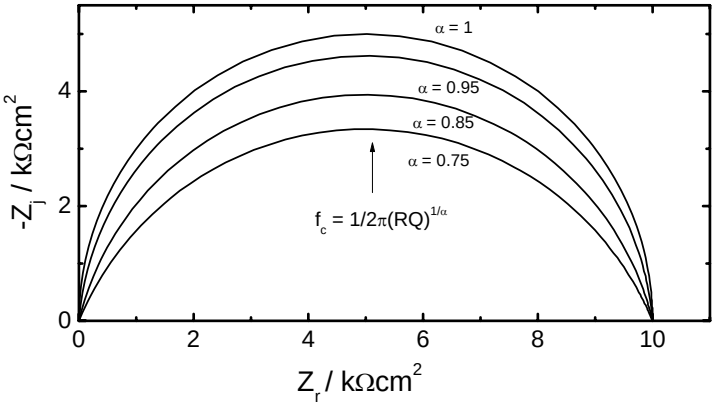

Figure 5-4. Impedance plane representation of equation (1–2) with α as a parameter and $Q = 1 \times 10^{-6}$ Fs$^{(\alpha-1)}/\mathrm{cm}^2$ and $R = 10\mathrm{k}\ \Omega\mathrm{cm}^2$.

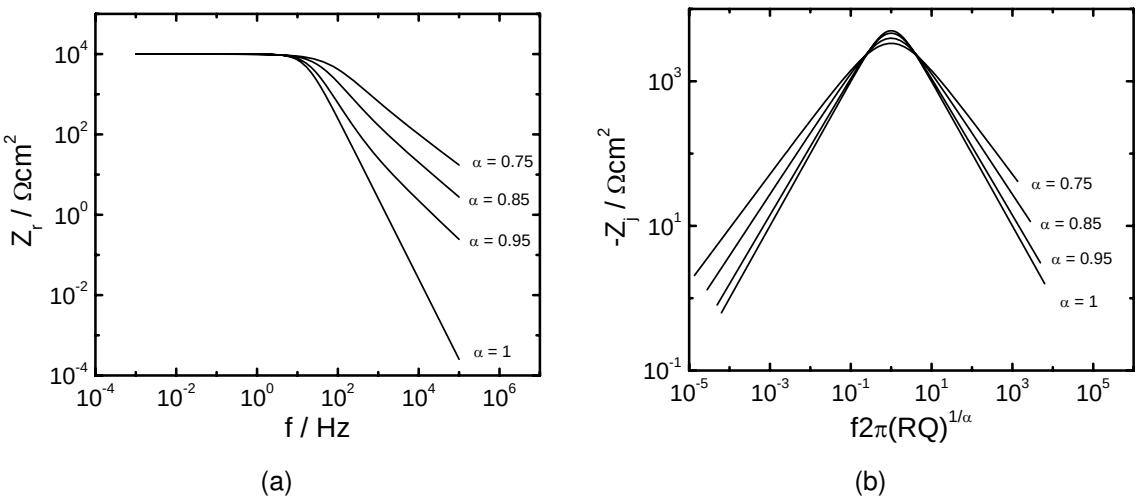

Figure 5-5. Impedance response of equation (1–2) with α as a parameter and $R = 10\mathrm{k}\ \Omega\mathrm{cm}^2$ and $Q = 1 \times 10^{-6}\ \mathrm{Fs}^{(\alpha-1)}/\mathrm{cm}^2$; a) the real component; and b) the imaginary component.

The CPE is a mathematical model widely used to fit experimental impedance data. As discussed in Chapters 1 and 2, the interpretation of the CPE in terms of physically meaningful parameters, such as capacitance, is controversial. In Chapter 6, the capacitance of electrochemical systems is reviewed and relationships between CPE parameters and capacitance, taken from the literature, are developed.

CHAPTER 6
THE CAPACITIVE RESPONSE OF ELECTROCHEMICAL SYSTEMS

The present chapter provides the theoretical framework necessary for interpreting the capacitive response of systems exhibiting the CPE. The diffuse layer capacitance and the capacitance of a dielectric layer is reviewed. Relationships relating capacitance and CPE parameters provided by Brug *et al.*[3] and Hsu and Mansfeld[6] yield different results. In many cases, both sets of equations have been applied to similar systems and are used without regarding the source of the CPE. The two different mathematical formulas for estimating effective capacitance from CPE parameters are associated unambiguously with either surface or normal time-constant distributions. The background presented in this chapter supplies the context needed for analysis of simulated and experimental data presented in Chapters 7-10.

6.1 Capacitance of the Diffuse Layer

Any interface between dissimilar phases, such as the electrode/electrolyte interface in an electrochemical cell, promotes charge separation that can be interpreted in terms of a capacitance. The electrode/electrolyte interface is characterized by distinct regions adjacent to the metal electrode. The inner Helmholtz plane (IHP) marks the distance of closest approach of specifically adsorbed ions and the outer Helmholtz plane (OHP) marks the distance of closest approach of solvated adsorbed ions. Following the notation of Newman,[88] the IHP is at a distance y_1 from the electrode and the OHP is at a distance y_2. The distance between the metal boundary y_m and the OHP boundary y_2 is on the sub-nanometer scale and contains the charge q_1. Extending beyond the OHP is the diffuse region which is on the order of nanometers and contains the charge q_2. Adjacent to the diffuse region is the diffusion region which is electrically neutral but may contain concentration gradients. Beyond the diffusion region is bulk electrolyte. The double layer refers to the Helmholtz region and the diffuse region.

The double layer capacitance is defined as

$$C_{\mathrm{dl}} = \left(\frac{\partial q}{\partial U}\right)_{\mu,T} \tag{6–1}$$

where q is the charge associated with the double layer and U is the potential. The charge on the metal interface is represented by q such that,

$$q + q_1 + q_2 = 0 \tag{6–2}$$

The diffuse layer capacitance is defined as

$$C_{\mathrm{d}} = -\left(\frac{\partial q_2}{\partial \Phi_2}\right)_{\mu,T} \tag{6–3}$$

where the subscript 2 represents the charge and potential associated with the diffuse layer. Deriving an expression for the diffuse layer capacitance begins with the statement of Poisson's equation

$$\nabla^2\Phi = -\frac{\rho_e}{\epsilon\epsilon_0} = -\frac{F}{\epsilon\epsilon_0}\sum_i z_i c_i \tag{6–4}$$

which relates the spacial distribution of the potential field with the charge distribution that gave rise to the field. Equation (6–4) relates the net charge density in the diffuse layer with the concentration of charged species. A relation between concentration and the potential field for the diffuse layer can be generated by applying the general species flux equation

$$N_i = -z_i u_i F c_i \nabla\Phi - D_i \nabla c_i + c_i \mathbf{v} \tag{6–5}$$

where u_i is the mobility and D_i is the diffusion coefficient. In the diffuse layer there is no net flux and no convection. Therefore, with use of the Nerst-Einstein relation $D_i = RTu_i$, equation (6–5) becomes

$$\nabla c_i = -\frac{z_i F}{RT} c_i \nabla\Phi \tag{6–6}$$

The solution of equation (6–6) is

$$c_i = c_{i\infty} \exp\left(-\frac{z_i F\Phi}{RT}\right) \tag{6–7}$$

which is the Boltzmann distribution of ionic concentrations. Equation (6–7) can be substituted into equation (6–4) yielding a differential equation relating the potential field and distance within the diffuse region.

The solution of the differential equation described by equations (6–4) and (6–7) for the diffuse layer requires the boundary conditions at the metal interface and in the solution bulk. The electric potential is zero far from the electrode surface

$$\Phi \rightarrow 0, y \rightarrow \infty \tag{6–8}$$

The metal interface boundary condition is a statement of Gauss's law

$$\frac{d\Phi}{dy} = \frac{q_2}{\epsilon\epsilon_0}, y = y_2 \tag{6–9}$$

stating that the electric field at the diffuse layer boundary is equivalent to the charge enclosed divided by the permittivity.

Newman[88] has shown the details of solving equations (6–4)-(6–9) where an expression relating charge in terms of potential is used to evaluate the diffuse layer capacitance according to equation (6–3)

$$C_{\mathrm{d}} = \frac{\epsilon\epsilon_0}{\lambda} \cosh\left(\frac{zF\Phi_2}{2RT}\right) \tag{6–10}$$

where λ is the Debye length,

$$\lambda = \sqrt{\frac{\epsilon\epsilon_0 RT}{2z^2F^2c_\infty}} \tag{6–11}$$

For the special case where the exponential term of equation (6–7) can be linearly approximated, *i.e.,* the Debye-Huckel approximation, equation (6–10) becomes

$$C_{\mathrm{d}} = \frac{\epsilon\epsilon_0}{\lambda} \tag{6–12}$$

6.2 Capacitance of a Dielectric Layer

The capacitance associated with a dielectric material is derived following the assumption that no free charges are present in the layer. Laplace's equation, rather than

equation (6–4), applies

$$\nabla^2 \Phi = 0 \tag{6–13}$$

The equivalent charge to the metal charge q is assumed to be located completely at the dielectric material boundary δ. The metal charge is called q and the material boundary charge is called q_2. In contrast, in the case of the diffuse layer the equivalent charge is distributed within the layer. Integrating equation (6–13) in one-dimension yields

$$\frac{d\Phi}{dy} = k \tag{6–14}$$

where k is a constant of integration. The first boundary condition is equivalent to the boundary condition expressed by equation (6–9),

$$\frac{d\Phi}{dy} = \frac{q_2}{\epsilon\epsilon_0}, y = 0 \tag{6–15}$$

Equation (6–15) is a statement of Gauss's law that the electric field is proportional to the charge enclosed. For a dielectric material there is no free charges and thus no change in the amount of charge enclosed as you move away from the interface. Therefore, the electric field is constant and equation (6–14) becomes

$$\frac{d\Phi}{dy} = \frac{q_2}{\epsilon\epsilon_0} \tag{6–16}$$

for y less than δ. Integration of equation (6–16) yields

$$\Phi = \frac{q_2}{\epsilon\epsilon_0} y + C \tag{6–17}$$

where C is a constant of integration. The second boundary condition is

$$\Phi = 0, y = \delta \tag{6–18}$$

Equation (6–18) is a statement of Gauss's law that the charge enclosed as you extend past the second boundary becomes zero and thus the electric field and electric potential is zero. This is an equivalent statement to equation (6–8). Using the boundary condition

equation (6–18) in equation (6–17) yields

$$\Phi = \frac{q_2}{\epsilon\epsilon_0} y - \frac{q_2}{\epsilon\epsilon_0}\delta \tag{6–19}$$

As was the case presented in Section 6.1, the capacitance is determined via evaluation of the potential at the metal interface as expressed by equation (6–3). The potential at the metal interface occurs at $y = 0$ and

$$\Phi_2 = -\frac{q_2}{\epsilon\epsilon_0}\delta \tag{6–20}$$

Rearranging equation (6–20) and applying equation (6–3) yields

$$C_{\mathrm{di}} = \frac{\epsilon\epsilon_0}{\delta} \tag{6–21}$$

where C_{di} is the capacitance associated with a dielectric material. Equation (6–12) implies that the capacitance of the diffuse layer is mathematically equivalent to the capacitance of a dielectric with all of the charge located at the Debye length. It should be noted that the Debye length is typically much smaller than the thickness of a dielectric layer, *i.e.,* an oxide film on the surface of electrode, and therefore, the effective capacitance associated with a dielectric in series with the diffuse layer capacitance is dominated by the capacitance of the dielectric.

6.3 Calculation of Capacitance from Impedance Spectra

As discussed in Chapter 1, the CPE is considered to arise from a distribution of time-constants in a system. Calculating capacitance using a single time-constant model does not apply for systems exhibiting the CPE. The formulas provided by Brug *et al.*[3] and Hsu and Mansfeld[6] yield different results for capacitance and are associated unambiguously with either surface or normal time-constant distributions.

6.3.1 Single Time-Constant Responses

When the impedance response of a system can be described by a single time-constant the calculation of the system's effective capacitance is straight-forward. The

impedance response of a single time-constant corrected for Ohmic resistance is

$$Z = \frac{R}{1 + j\omega RC} \tag{6–22}$$

and in the high-frequency region equation (6–22) reduces to

$$Z = \frac{1}{j\omega C} \tag{6–23}$$

Therefore, the capacitance of a system that can be modeled by a single RC is calculated from the measured imaginary impedance in the high-frequency region as

$$C_{RC} = \frac{-1}{\omega Z_j} \tag{6–24}$$

Alternatively, the capacitance of a single time-constant model can be determined by identifying the frequency corresponding to the peak of the imaginary impedance

$$C_{RC} = \frac{1}{2\pi R f_{\text{peak}}} \tag{6–25}$$

where R is determined at the limit of low-frequency.

6.3.2 Surface Distributions

In the case of a surface time-constant distribution, the global admittance response of the electrode must include additive contributions from each part of the electrode surface. The situation is demonstrated in Figure 6-1(a), where a surface distribution of time constants in the presence of an Ohmic resistance results in a distributed time-constant behavior expressed as a summation of admittances. For an appropriate time-constant distribution, the impedance response may be expressed in terms of a CPE. Interestingly, in the absence of an Ohmic resistance, shown in Figure 6-1(b), the surface distribution of time constants results in an effective RC behavior in which

$$\frac{1}{R_{\text{eff,s}}} = \sum \frac{1}{R_i} \tag{6–26}$$

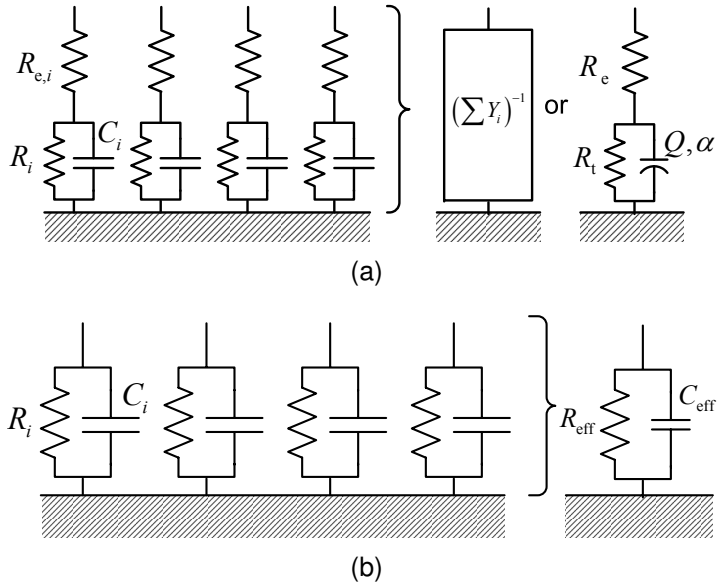

Figure 6-1. Schematic representation of a surface distribution of time constants: a) distribution of time constants in the presence of an Ohmic resistance resulting in a distributed time-constant behavior that, for an appropriate time-constant distribution, may be expressed as a CPE; and b) distribution of time constants in the absence of an Ohmic resistance resulting in an effective RC behavior. The admittance Y_i shown in (a) includes the local interfacial and Ohmic contributions.

and

$$C_{\text{eff,s}} = \sum C_i \tag{6–27}$$

Thus, the appearance of a CPE behavior associated with a surface distribution of time constants requires the contribution of an Ohmic resistance.[89,90] While an Ohmic resistance in physical systems cannot be avoided, the example illustrated in Figure 6-1(b) illustrates the crucial role played by the Ohmic resistance in CPE behavior associated with surface distributions.

Following the development of Brug *et al.*,[3] the relationship between CPE parameters and capacitance requires an assessment of the characteristic time constant corresponding to the admittance of the electrode. Thus,

$$Y = \sum_i Y_i = \sum_i \left(R_{\text{e},i} + \frac{R_i}{1 + j\omega R_i C_i} \right)^{-1} \tag{6–28}$$

where Y_i is the local admittance represented in Figure 6-1(a), $R_{\text{e},i}$ is the local Ohmic resistance and R_i and C_i represent the local surface properties. On the other hand, the total admittance of the electrode can also be expressed in terms of the symmetric CPE represented by equation (1–2) as

$$Y = \frac{1}{R_\text{e}} \left[1 - \frac{R_\text{t}}{R_\text{e} + R_\text{t}} \left(1 + \frac{R_\text{e} R_\text{t}}{R_\text{e} + R_\text{t}} Q(j\omega)^\alpha \right)^{-1} \right] \tag{6–29}$$

where R_e is the global Ohmic resistance and R_t, Q, and α represent global properties. Equation (6–29) can be expressed in terms of a characteristic time constant associated with the admittance spectra τ_Y as

$$Y = \frac{1}{R_\text{e}} \left[1 - \frac{R_\text{t}}{R_\text{e} + R_\text{t}} \left(1 + (j\omega\tau_Y)^\alpha \right)^{-1} \right] \tag{6–30}$$

where

$$\tau_Y = \frac{R_\text{e} R_\text{t}}{R_\text{e} + R_\text{t}} C \tag{6–31}$$

The characteristic time-constant τ_Y corresponds to the frequency at which the imaginary component of the admittance spectra of the symmetric CPE, equation (6–29), reaches

its peak value. Comparison of equations (6–29) and (6–30) yields

$$\tau_Y^{\alpha} = Q\frac{R_{\mathrm{e}}R_{\mathrm{t}}}{R_{\mathrm{e}}+R_{\mathrm{t}}} = Q\left(\frac{1}{R_{\mathrm{e}}}+\frac{1}{R_{\mathrm{t}}}\right)^{-1} \tag{6–32}$$

The capacitance associated with the CPE can therefore be expressed as

$$C_{\mathrm{B}} = Q^{1/\alpha}\left(R_{\mathrm{e}}^{-1}+R_{\mathrm{t}}^{-1}\right)^{(\alpha-1)/\alpha} \tag{6–33}$$

or

$$C_{\mathrm{B}} = Q^{1/\alpha}\left(\frac{R_{\mathrm{e}}R_{\mathrm{t}}}{R_{\mathrm{e}}+R_{\mathrm{t}}}\right)^{(1-\alpha)/\alpha} \tag{6–34}$$

where the subscript B refers to the author Brug. Equations (6–33) and (6–34) are equivalent to equation (20) derived by Brug *et al.*[3] for a surface distribution with a different definition of CPE parameters. In the limit that R_{t} becomes infinitely large, equation (6–34) becomes

$$C_{\mathrm{B}} = Q^{1/\alpha}R_{\mathrm{e}}^{(1-\alpha)/\alpha} \tag{6–35}$$

which is equivalent to equation (5) presented by Brug *et al.*[3] for a blocking electrode.

6.3.3 Normal Distributions

In the case of a normal time-constant distribution through a surface layer, the global impedance response of the electrode must include additive contributions from each part of the layer. The situation is demonstrated in Figure 6-2, where a normal distribution of time constants results in a distributed time-constant behavior expressed as a summation of impedances. For an appropriate time-constant distribution, the impedance response may be expressed in terms of a CPE. In this case, the appearance of a CPE behavior does not require the contribution of an Ohmic resistance. The appearance of a CPE from a series of Voigt RC elements does, however, require contributions from both resistive and capacitive elements.

The relationship between CPE parameters and capacitance requires an assessment of the characteristic time constant corresponding to the impedance of the layer τ_Z.

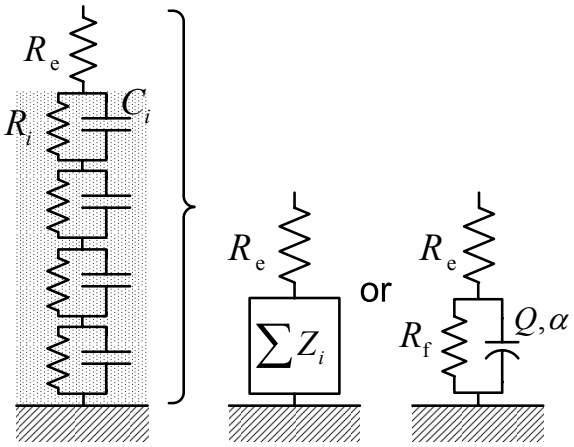

Figure 6-2. Schematic representation of a normal distribution of time constants resulting in a distributed time-constant behavior that, for an appropriate time-constant distribution, may be expressed as a CPE.

Thus,

$$Z = R_{\mathrm{e}} + \sum_i Z_i = R_{\mathrm{e}} + \sum_i \frac{R_i}{1 + j\omega R_i C_i} \tag{6–36}$$

where R_{e} is the Ohmic resistance and R_i and C_i represent the local properties of the layer. For a series of RC elements the effective capacitance is expressed as

$$C_{\mathrm{eff,n}} = \frac{1}{\sum \frac{1}{C_i}} \tag{6–37}$$

Since the Ohmic resistance does not contribute to the time-constant dispersions of a film, the development can be performed in terms of an Ohmic resistance-corrected impedance $Z - R_{\mathrm{e}}$.

The Ohmic resistance-corrected impedance of a film can be expressed in terms of a CPE as

$$Z - R_{\mathrm{e}} = \frac{R_{\mathrm{f}}}{1 + (j\omega)^{\alpha} Q R_{\mathrm{f}}} \tag{6–38}$$

where

$$R_{\mathrm{f}} = \sum_i R_i \tag{6–39}$$

represents the film resistance. Alternatively,

$$Z - R_{\mathrm{e}} = \frac{R_{\mathrm{f}}}{1 + (j\omega\tau_Z)^{\alpha}} \tag{6–40}$$

Comparison of equations (6–38) and (6–40) yields

$$\tau_Z^{\alpha} = (R_{\mathrm{f}}C)^{\alpha} = QR_{\mathrm{f}} \tag{6–41}$$

The characteristic time-constant τ_Z corresponds to the frequency at which the imaginary component of the impedance spectra of the symmetric CPE, equation (6–29), reaches its peak value. The capacitance associated with the CPE can therefore be expressed as

$$C_{\mathrm{HM}} = Q^{1/\alpha}R_{\mathrm{f}}^{(1-\alpha)/\alpha} \tag{6–42}$$

Equation (6–42) is equivalent to equation (3) presented without derivation by Hsu and Mansfeld[6] in terms of $\omega_{\max}$.

6.4 Conclusions

The capacitance of a dielectric, as shown by equation (6–21), is inversely related to layer thickness. The effective capacitance, equations (6–27) and (6–37), was defined as the composite capacitance of the individual capacitances of a system. Calculation of capacitance using equation (6–24) is only valid for systems described by a single time-constant, *i.e.,* $\alpha = 1$. The derivations of the Brug and Hsu-Mansfeld formulas for calculating capacitance of CPE systems are based on the premise that there is a characteristic time-constant corresponding to the peak of the imaginary admittance and imaginary impedance, respectively. Equations (6–34), (6–35), and (6–42) have all the same form, but the resistance used in the calculations of capacitance is different in the three cases, being respectively the parallel combination of R_{t} and R_{e} for equation (6–34), R_{e} for equation (6–35) and R_{f} for equation (6–42).

Without the aid of a physical model to account for the CPE it is generally assumed that the Brug and Hsu-Mansfeld formulas yield the effective capacitance of a system. These formulas yield different results for the same CPE parameters. A distinction was made between systems where a surface distribution of properties is expected to be the source of the CPE from systems where a normal distribution of properties is expected to

be the source of the CPE. For surface distributions the CPE is envisioned to arise from the sum of admittances and the Ohmic resistance plays a crucial role in the presence of the CPE. Therefore, equation (6–34) is assumed to apply for surface distributions. For normal distributions the CPE is envisioned to arise from the sum of impedances and the Ohmic resistance plays no role in the presence of the CPE. Therefore, equation (6–42) is assumed to apply for normal distributions. The Brug and Hsu-Mansfeld equations for capacitance are evaluated using simulated and experimental systems in Chapter 7.

CHAPTER 7
ASSESSMENT OF CAPACITANCE-CPE RELATIONS TAKEN FROM THE LITERATURE

Two different mathematical formulas for estimating effective capacitance from CPE parameters, presented in Chapter 6, were associated unambiguously with either surface or normal time-constant distributions. In many cases, these formulas are used without regard for the type of distribution that is the source of the CPE. The objective of the present chapter is to explore the conditions of validity for models which relate capacitance to CPE parameters. Application to different experimental and simulated systems are used to illustrate the importance of using the correct formula that corresponds to a given type of distribution. When the local resistivity varies considerably over the thickness of a film, the experimental frequency range may preclude observation of the capacitance contribution of a portion of the film, resulting in under prediction of the film thickness. In many cases, calculating capacitance from CPE parameters without the aid of a physical model is unreliable, which provides the motivation for developing mechanisms to account for the CPE presented in Chapter 8.

7.1 Surface Distributions

Huang *et al.*[18] have shown that current and potential distributions induce a high-frequency pseudo-CPE behavior in the global impedance response of an ideally polarized blocking electrode with a local ideally capacitive behavior. In a related work, Huang *et al.*[19] explored the role of current and potential distributions on the global and local impedance responses of a blocking electrode exhibiting a local CPE behavior. They were able to relate the global impedance response to local impedance, and distinctive features of the calculated global and local impedance response were verified experimentally. A similar development was presented for a disk electrode with a Faradaic reaction.[2]

This work was used to explore the applicability of equations (6–34), (6–35), and (6–42) for determination of effective capacitance. The approach allowed comparison

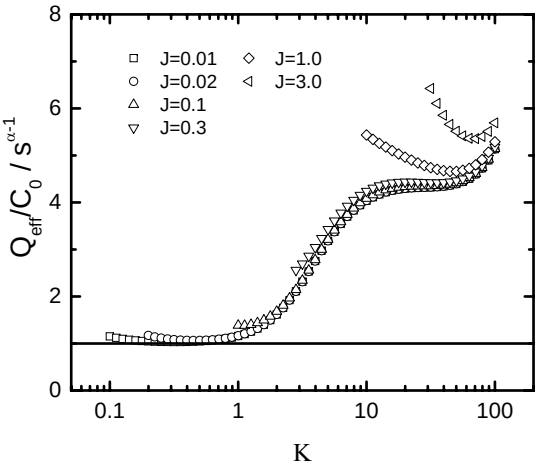

Figure 7-1. Effective CPE coefficient scaled by the interfacial capacitance as a function of dimensionless frequency K with J as a parameter. Taken from Huang *et al.*[2]

between the estimated capacitance and the value assumed for the simulations. The graphical methods presented by Orazem *et al.*[87] were used to obtain CPE parameters α and Q. The parameters α and Q were obtained from equations (5–3) and (5–4), respectively. The parameters α and Q obtained by graphical evaluation are the same as would be obtained by regression analysis. As discussed by Huang *et al.*,[2] the frequencies used for the analysis were limited to those that were one decade larger than the characteristic peak frequency because, in this frequency range, the value of α was well-defined. The analysis took into account the observation that the value of α was dependent on the frequency at which the slope was evaluated.

The value of effective CPE coefficient, Q, scaled by the interfacial capacitance C_0 used for the simulations, is presented in Figure 7-1 as a function of dimensionless frequency $\mathrm{K} = \omega C_0 r_0/\kappa$, where r_0 is the disk radius, and κ is the conductivity of the electrolyte. The results given in Figure 7-1 are presented as a function of the parameter J, incorporated as part of the boundary condition for Faradaic reactions at the electrode surface. Under the assumption of linear kinetics, valid for steady-state current densities $\bar{i}$ much smaller than the the exchange current density i_0, the parameter J was defined to

be

$$J = \frac{(\alpha_a + \alpha_c)\, F i_0 r_0}{RT\kappa} \tag{7–1}$$

where α_a and α_c are, respectively, anodic and cathodic apparent transfer coefficients. For Tafel kinetics, valid for $\bar{i} >> i_0$, the parameter J was defined to be a function of radial position on the electrode surface as

$$J(r) = \frac{\alpha_c F \left|\bar{i}(r)\right| r_0}{RT\kappa} \tag{7–2}$$

where $\bar{i}(r)$ was obtained from the steady-state solution as

$$\bar{i}(r) = -i_0 \exp\left(-\frac{\alpha_c F}{RT}\left(\bar{V} - \bar{\Phi}_0(r)\right)\right) \tag{7–3}$$

where $\bar{V} - \bar{\Phi}_0(r)$ represents the local interfacial potential driving force for the reaction.

The parameter J can be expressed in terms of the Ohmic resistance R_{e} and charge transfer resistance R_{t} as

$$J = \frac{4}{\pi}\frac{R_{\mathrm{e}}}{R_{\mathrm{t}}} \tag{7–4}$$

Large values of J are seen when the Ohmic resistance is much larger than the charge-transfer resistance, and small values of J are seen when the charge-transfer resistance dominates. At high-frequencies, where frequency dispersion plays a significant role, the effective CPE coefficient Q provides an inaccurate estimate for the interfacial capacitance used as an input for the simulations, even for small values of J where, as shown by Huang *et al.*,[2] α is close to unity. As shown in Figure 7-1, assumption that Q represents the interfacial capacitance results in errors on the order of 500 percent at $\mathrm{K} = 100$.

Equations (6–35) and (6–34), *i.e.,* C_{B}, are compared to the input value of interfacial capacitance in Figures 7-2(a) and 7-2(b), respectively. Following the observation by Huang *et al.*[2] that the geometry-induced potential and current distributions yield a pseudo-CPE behavior in which the coefficient α is a weak function of frequency, Figures 7-2(a) and 7-2(b) were developed using frequency-dependent values of α and Q. Thus,

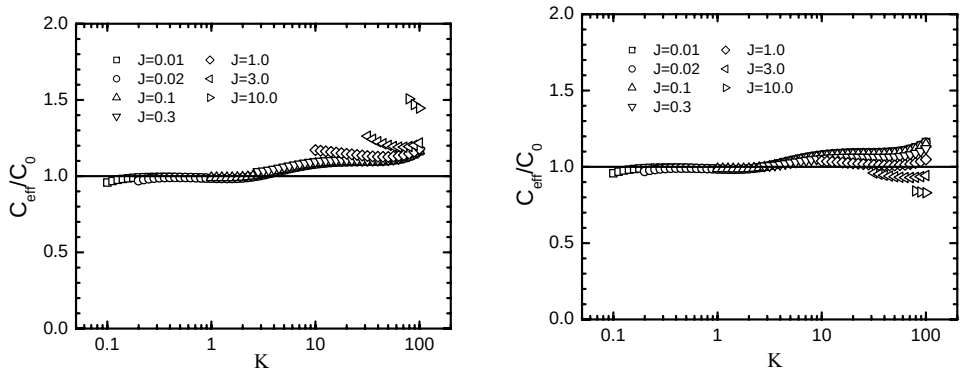

Figure 7-2. Normalized effective capacitance calculated from relationships presented by Brug *et al.*[3] for a disk electrode as a function of dimensionless frequency K with J as a parameter: a) with correction for Ohmic resistance R_e (equation (6–35)); and b) with correction for both Ohmic resistance R_e and charge-transfer resistance R_t (equation (6–34)). Taken from Huang *et al.*[2]

the value of Q reported is that corresponding to the value of α at a given frequency K. The error in equation (6–35) is a function of both frequency K and J. While equation (6–35) applies strictly for a blocking electrode, it gives the correct answer for Faradaic systems if one chooses to calculate α at frequencies $\mathrm{K} < 5$, but fails for $\mathrm{K} > 5$. The dependence on J is reduced significantly when both the Ohmic resistance R_e and charge-transfer resistance R_t are taken into account, and the errors in estimating interfacial capacitance are less than 20 percent. The correction for R_t in equation (6–34) is important for frequencies $\mathrm{K} > 5$. Of the relationships tested, equation (6–34) provides the best means for estimating interfacial capacitance when frequency dispersion is significant.

Equation (6–42), *i.e.,* C_HM, was tested against the input value of interfacial capacitance in Figure 7-3 where C_0 is the known interfacial capacitance. While equation (6–42) represents an improvement as compared to direct use of the CPE coefficient Q, the errors in estimating the interfacial capacitance depend on both J and K and

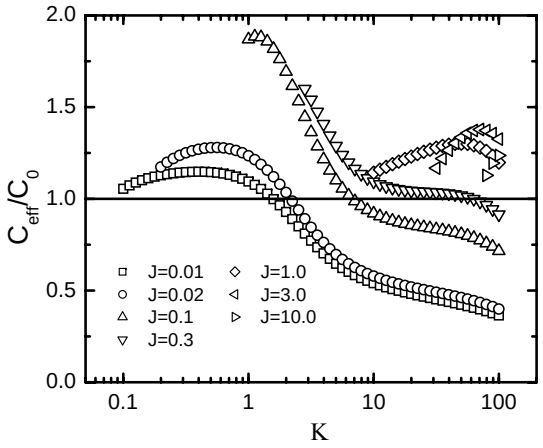

Figure 7-3. Effective capacitance calculated from equation (6–42) and normalized by the input interfacial capacitance for a disk electrode as a function of dimensionless frequency K with J as a parameter. Taken from Huang *et al.*[2]

range between -70 to $+100$ percent. Equation (6–42), developed for a normal time-constant distribution, is not appropriate for interpretation of results affected by a surface time-constant distribution.

7.2 Normal Distributions

Equation (6–42), developed for normal time-constant distributions, was applied for determination of effective capacitance in two systems in which a normal variation of resistivity may be expected.

7.2.1 Niobium

The anodic dissolution of a 0.25 cm^2 Nb (99.9%, Goodfellow) rotating disk electrode was studied in a pH 2 solution containing 0.1 M NH_4F and sodium sulfate as supporting electrolyte.[4] The experimental impedance data corresponding to an anodization potential of 6 V(SCE) are shown in Figure 7-4(a). According to the "surface charge approach" developed by Bojinov,[91,92] the dielectric properties of the oxide film dominate the high-frequency response. The medium-frequency inductive loop and low-frequency capacitive line are also described by Cattarin *et al.*[4] and Frateur.[93] Figure 7-4(b) shows that a plot of the logarithm of the imaginary part of the impedance as a function of the logarithm of the frequency yields a straight line with a slope of -0.90 for frequencies

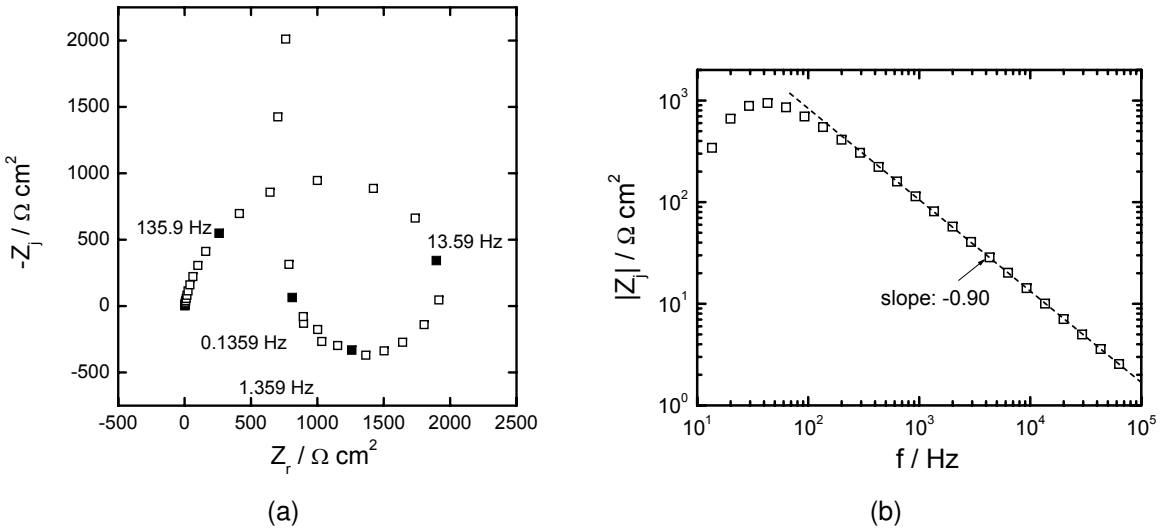

Figure 7-4. Experimental impedance data obtained with a Nb rotating disk electrode (900 rpm) in 0.1 M NH_4F solution (pH 2), at 6 V(SCE): a) Complex plane plot; and b) the imaginary part of the impedance as a function of frequency. Data taken from Cattarin *et al.*[4]

higher than 300 Hz, which indicates a CPE behavior with a CPE exponent of 0.90,[87] rather than the response of a true $R_f C_f$ parallel combination, where R_f is the oxide film resistance and C_f is the oxide film capacitance. Furthermore, in Figure 7-4(b), the surface distribution caused by non-uniform current and potential distributions cannot be observed in the high-frequency range since $\mathrm{K} = 1$ would correspond to 65 kHz and the maximum frequency that was used in the experiments was 63.1 kHz.[19]

The CPE parameters α and Q for the high-frequency loop were obtained using the graphical methods presented by Orazem *et al.*,[87] (equations (5–3) and (5–4), respectively). The resulting values for different anodization potentials are presented in Table 7-1. The values of the oxide film resistance corresponding to the diameter of the high-frequency loop are also reported in Table 7-1. From the CPE parameters and the film resistance, the capacitance of the oxide film was calculated via equation (6–42), *i.e.,* C_{HM}, and applied as the system's effective capacitance (see Table 7-1).

For normal time-constant distributions for which the dielectric constant may be assumed to be independent of position, the capacitance should be related to film

Table 7-1. CPE parameters, resistance, effective capacitance, and thickness of oxide films formed on a Nb disk electrode in 0.1 M NH_4F solution (pH 2) as a function of the anodization potential.

Potential / V(SCE)	α	Q / Ω^{-1}cm^{-2}s$^{\alpha}$	R_f / kΩcm^2	C_{HM} / μF cm^{-2}	d_{eff} / nm
2	0.95	5.9×10^{-6}	1.30	4.6	8
6	0.90	3.5×10^{-6}	2.01	2.0	18
10	0.88	2.5×10^{-6}	3.65	1.3	29

thickness according to equation (6–21). If C_{HM} is taken as the system's effective capacitance then

$$C_{HM} = \frac{\varepsilon\varepsilon_0}{d_{eff}} \tag{7–5}$$

where ε is the dielectric constant and $\varepsilon_0 = 8.8542 \times 10^{-14}$ F/cm is the permittivity of vacuum. In equation (7–5) δ has been replaced with d_{eff} to represent the fact that the calculated capacitance according to the Hsu-Mansfeld formula, *i.e.,* equation (6–42), is considered to represent the effective capacitance of the system. In the case of anodic dissolution of Nb in acid fluoride medium, the oxide is assumed to be Nb_2O_5 and $\varepsilon = 42$.[94,95] The values of d_{eff} are presented in Table 7-1 for different anodization potentials.

The calculated values of d_{eff} can be compared to those given in the literature. In Lohrengel's review of metal oxides,[96] different values for the thickness of Nb_2O_5 films formed on Nb electrodes at $E = 0$ V(SHE) are given that vary between 3 and 6.7 nm. Moreover, the formation ratio (*i.e.,* the thickness increase caused by a unit increase of the polarization potential) is reported to be 2.6 or 2.8 nm/V. Therefore, according to Lohrengel,[96] the thickness δ can be estimated approximately to be $\delta = 5.0 + 2.70E$ where δ has units of nm and E is expressed in V(SHE). The method(s) used to determine the oxide film thicknesses and the electrolyte composition are not mentioned in Reference [96]. Arsova *et al.*[97] measured the thickness of Nb_2O_5 films formed in 1 M H_2SO_4 by ellipsometry. The formation ratio determined by these authors is 2.26 nm/V. Extrapolation of their δ to $E = 0$ V yields $\delta = 5$ nm. Therefore, the

Table 7-2. Thickness of oxide films developed on a Nb electrode, as a function of the anodization potential. Comparison of values deduced from impedance data with those from the literature.

	Present Work	Values from Literature		
Potential / V(SCE)	d_{eff} / nm	δ / nm [96]	δ / nm [97]	δ / nm [98]
2	8	11	10	7
6	18	22	19	15
10	29	33	28	24

thickness found by Arsova *et al.*[97] can be estimated to be $\delta = 5.0 + 2.26E$ where δ has units of nm and E is expressed in V(SHE). Habazaki *et al.*[98] measured the thickness of the oxide by TEM of an ultramicrotomed section and by impedance. From their data, the thickness can be estimated to be $\delta = 2.4 + 2.08E$ where δ has units of nm and E is referenced to Pt in 0.1 M H_3PO_4. The values of Nb_2O_5 film thickness calculated by using equations (6–42) and (7–5) for different anodization potentials are compared with those calculated from the data of Lohrengel,[96] Arsova *et al.*[97] and Habazaki *et al.*[98] in Table 7-2. The values of d_{eff} calculated by application of equations (6–42) and (7–5) to impedance data are in very good agreement with the literature values, in particular with those obtained from non-electrochemical measurements. Our results agree also with those of Heidelberg *et al.*[99] who reported on the oxidation of 10 nm thick Nb layers in micro- and nano-cells.

To show the consequence of the misuse of the resistance term in the calculation of the effective capacitance, the values of C_{B} were calculated using equation (6–34) in which R_{t} was replaced by R_{f}. Equation (6–35) yielded the same values for C_{B} as equation (6–34) since $R_{\text{f}} >> R_{\text{e}}$. As before, equation (7–5) was used to estimate d_{eff} with C_{HM} replaced by C_{B}. Use of equation (6–35) yielded: for 2 V(SCE), $C_{\text{B}} = 3.2\ \mu$F/cm^2 and $d_{\text{eff}} = 12$ nm, for 6 V(SCE), $C_{\text{B}} = 0.9\ \mu$F/cm^2 and $d_{\text{eff}} = 41$ nm, and for 10 V(SCE), $C_{\text{B}} = 0.5\ \mu$F/cm^2 and $d_{\text{eff}} = 74$ nm. Comparison to the values presented in Table 7-1 shows that the effective film thickness obtained using the effective capacitance

obtained from equation (6–35) can be significantly larger than the actual film thickness, especially at high potential.

7.2.2 Human Skin

Impedance data were collected for heat-separated excised human stratum corneum obtained from the abdomen or the back.[1] The separation procedure involved physical and mechanical manipulations to separate the stratum corneum from the underlying dermis. Deionized water was the only solvent added during the process. The skin samples were mounted between glass diffusion cells prior to the impedance study. The skin and the solution were maintained at constant temperature of 32°C with a water-jacketed diffusion cell. Magnetic stir bars were used for each chamber of the diffusion cell to keep the solutions well mixed. The electrochemical impedance measurements were conducted with a Solartron 1286 potentiostat and a Solartron 1250 frequency-response analyzer. A four-electrode configuration was used for all of the studies. The Ag/AgCl counter and working electrodes were produced by In Vivo Metric. The Ag/AgCl reference electrodes were fabricated by Micro Electrodes, Inc.

The slightly moistened epidermis was stored in between two sheets of polymer film in a refrigerator. At the start of a typical experiment the skin was removed from the refrigerator and immersed in a 32°C 50 mM $CaCl_2$ / 20 mM HEPES solution (pH of 6.95) which provided approximately the same pH and ionic strength as the electrolytic fluid within the body.[100] Replicate electrochemical impedance spectra were collected periodically using Variable-Amplitude Galvanostatic (VAG) modulation.[101,102] The sinusoidal current perturbation was superimposed about a 0 μA DC current bias, and the amplitude of the potential response across the skin was maintained at $\pm$10 mV. The individual scans took approximately five minutes and were shown to satisfy the Kramers-Kronig relations, indicating that the system was stationary on the time scale of the experiments. Upon completion of an impedance scan the skin was allowed to relax for three minutes before the replicated spectrum was collected.

Table 7-3. CPE parameters, resistance, effective capacitance, and thickness for heat-stripped human stratum corneum in 50 mM buffered $CaCl_2$ electrolyte as a function of immersion time. Data taken from Membrino.[1]

Time / hr	α	Q / Ω^{-1}cm^{-2}s$^{\alpha}$	R_f / kΩcm^2	C_{HM} / μF cm^{-2}	δ_{HM} / μm
0.0	0.824	6.13×10^{-8}	60	1.86×10^{-2}	2.3
1.9	0.834	5.36×10^{-8}	51	1.66×10^{-2}	2.6
5.1	0.838	5.40×10^{-8}	42	1.66×10^{-2}	2.6

Impedance results are presented in Figure 7-5(a) with immersion time as a parameter. The straight lines evident at high frequencies in Figure 7-5(b) show a high-frequency constant-phase behavior. The CPE parameters α and Q were obtained using the graphical methods presented by Orazem *et al.*[87] The resulting values for different immersion times are presented in Table 7-3. The value of the thickness of the skin depends on its dielectric constant ε. The estimated thicknesses d_{eff} reported in Table 7-3 were obtained from equations (6–42) and (7–5) under the assumption that $\varepsilon = 49$. The value of dielectric constant used in the present work was obtained by the comparison, shown in a subsequent section, of the Young model to the impedance data. The resulting values of d_{eff} of around 2 μm are substantially smaller than the thickness of the stratum corneum, which is accepted to have a value between 10 and 40 μm.[103]

Equation (6–35) was also used to calculate the effective capacitance. As for the case of Nb_2O_5, equation (6–34) yielded similar values for C_B as equation (6–35) since $R_f >> R_e$. Equation (7–5) with C_{HM} replaced by C_B was used to estimate d_{eff}. Use of equation (6–35) yielded: for 0.0 h, $C_B = 4.5 \times 10^{-3}$ μF/cm^2 and $d_{eff} = 9.6$ μm, for 1.9 h, $C_B = 3.7 \times 10^{-3}$ μF/cm^2 and $d_{eff} = 12$ μm, and for 5.1 h, $C_B = 3.1 \times 10^{-3}$ μF/cm^2 and $d_{eff} = 14$ μm. Interestingly, the effective film thickness calculated using the effective capacitance obtained from equation (6–35) was closer to the expected value than was the thickness estimated using equation (6–42). The apparent better agreement is found in spite of the fact that the Ohmic resistance R_e has no relationship to the dielectric property of the skin. This work illustrates a need for a better understanding of the influence of strong variations of resistivity on the impedance response.

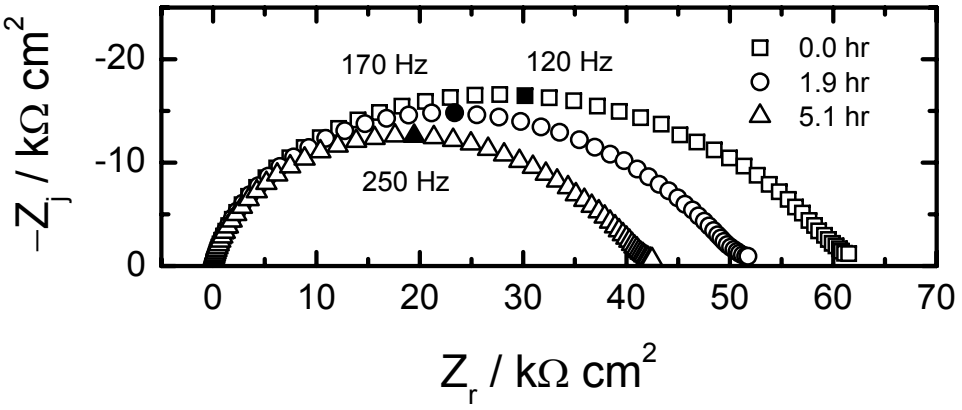

(a)

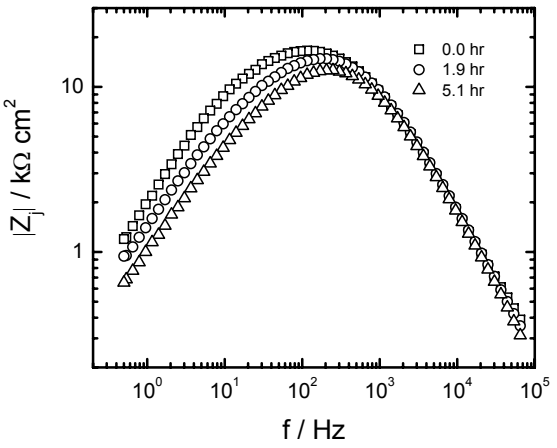

(b)

Figure 7-5. Experimental impedance data obtained for heat-separated excised human stratum corneum in 50 mM buffered $CaCl_2$ electrolyte with immersion time as a parameter: a) Complex plane plot; and b) the imaginary part of the impedance as a function of frequency. Data taken from Membrino.[1]

7.2.3 Films with an Exponential Decay of Resistivity

The values of d_{eff} calculated using equations (6–42) and (7–5) were in very good agreement with the literature values for Nb_2O_5 films, but the values obtained for human stratum corneum were substantially smaller than the expected values. Both the Niobium oxide[93,26,104] and the skin systems[27,105] have been described as having a resistivity that decays exponentially with position. The case of a film with a uniform dielectric constant and an exponential decay of local resistivity is mathematically equivalent to the Young model, in which an exponential increase in conductivity is assumed.[26,104] The local resistance $R(x)$ can be expressed as

$$R(x) = \rho_0 \mathrm{e}^{-x/\lambda} \mathrm{d}x \tag{7–6}$$

where ρ_0 is the maximum value of resistivity found at $x = 0$, which corresponds to the oxide–electrolyte interface, and λ represents a characteristic length. The effective resistance of the film can be obtained by integration over the film thickness δ, *i.e.,*

$$R_{\text{eff}} = \int_0^{\delta} \rho_0 \mathrm{e}^{-x/\lambda} \mathrm{d}x \tag{7–7}$$

to yield

$$R_{\text{eff}} = \rho_0 \lambda \left(1 - \mathrm{e}^{-\delta/\lambda}\right) \tag{7–8}$$

The local capacitance can be expressed as

$$C(x) = \frac{\varepsilon \varepsilon_0}{\mathrm{d}x} \tag{7–9}$$

where the dielectric constant ε was assumed to have a uniform value. The effective capacitance, obtained by integration over the film thickness, following

$$\frac{1}{C_{\text{eff}}} = \int_0^{\delta} \frac{1}{\varepsilon \varepsilon_0} \mathrm{d}x \tag{7–10}$$

is found to be

$$C_{\text{eff}} = \frac{\varepsilon \varepsilon_0}{\delta} \tag{7–11}$$

Equation (7–11) is identical to equation (7–5) and equation (6–21), as the integration is valid for all dielectrics.

The impedance of the film is obtained from integration across the film thickness following

$$Z = \int_0^{\delta} \frac{\rho_0 \mathrm{e}^{-x/\lambda}}{1 + j\omega\rho_0 \mathrm{e}^{-x/\lambda}\varepsilon\varepsilon_0} \mathrm{d}x \tag{7–12}$$

The result is

$$Z = -\frac{\lambda}{j\omega\varepsilon\varepsilon_0} \ln\left[\frac{1 + j\omega\varepsilon\varepsilon_0\rho_0 \mathrm{e}^{-\delta/\lambda}}{1 + j\omega\varepsilon\varepsilon_0\rho_0}\right] \tag{7–13}$$

as was already calculated by Göhr *et al.*[106,107] Equation (7–13) is referred to as the Young impedance. In the low-frequency limit, application of L'Hôpitals rule yields

$$\lim_{\omega\to 0} Z = \lambda\rho_0 \left(1 - \mathrm{e}^{-\delta/\lambda}\right) \tag{7–14}$$

This result is in agreement with the direct integration of resistivity which yielded equation (7–8). In the high-frequency limit,

$$\lim_{\omega\to\infty} Z = -j\frac{\delta}{\omega\varepsilon\varepsilon_0} \tag{7–15}$$

This result is also in agreement with direct integration of capacitance which yielded equation (7–11).

The impedance response associated with equation (7–13) is presented in Figure 7-6 in dimensionless form with δ/λ as a parameter. The impedance was scaled by the zero-frequency asymptote given by equation (7–14). The characteristic frequency indicated in the figure is in dimensionless form following $\omega\varepsilon\varepsilon_0\rho_0$. For $\delta/\lambda = 1$, the peak in the imaginary impedance is slightly smaller than 0.5 and the Nyquist plot is only slightly depressed from perfect RC behavior. For larger values of δ/λ, distortion is evident at higher frequencies. The shape of the plot remains unchanged for $\delta/\lambda > 5$. The absence of time-constant dispersion at low frequencies indicates that the Young model cannot account for the low-frequency behavior for skin seen in Figure 7-5(a).

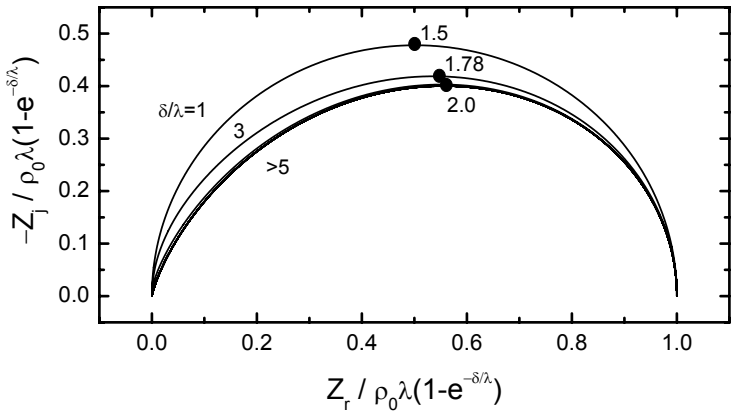

Figure 7-6. Nyquist plots for simulation of the impedance associated with an exponential decay of resistivity with δ/λ as a parameter. The characteristic frequency indicated is in dimensionless form following $\omega\varepsilon\varepsilon_0\rho_0$.

To understand the relationship between Young impedance and CPE behavior, impedance values calculated according to equation (7–13) were analyzed by an R_{f}-CPE parallel combination, in series with the electrolyte resistance. The CPE parameters Q and α can be obtained following the graphical methods outlined by Orazem *et al.*[87] The parameter α can be obtained from the slope of the imaginary part of the impedance plotted as a function of frequency in a logarithmic scale. The slope is presented in Figure 7-7 as a function of dimensionless frequency $\omega\varepsilon\varepsilon_0\rho_0$. At low frequency, $\mathrm{d}\log|Z_j|/\mathrm{d}\log\omega = 1$, showing that the exponential decay of resistivity does not result in low-frequency time-constant dispersion. At high frequency and for $\delta/\lambda = 1$, $\mathrm{d}\log|Z_j|/\mathrm{d}\log\omega = -1$, again showing that the exponential decay of resistivity does not result in high-frequency time-constant dispersion. For larger values of δ/λ, a significant frequency range above $\omega\varepsilon\varepsilon_0\rho_0 = 1$ is seen for which $\mathrm{d}\log|Z_j|/\mathrm{d}\log\omega$ differs from -1.

The CPE parameters Q and α were determined graphically for each frequency above $\omega\varepsilon\varepsilon_0\rho_0 = 1$. The effective capacitance was calculated using equation (6–42), and the effective film thickness was calculated using equation (7–5). The results are presented in Figure 7-8(a) as a function of dimensionless frequency and with δ/λ as a parameter. If the frequency is sufficiently large, the effective film thickness d_{eff} is

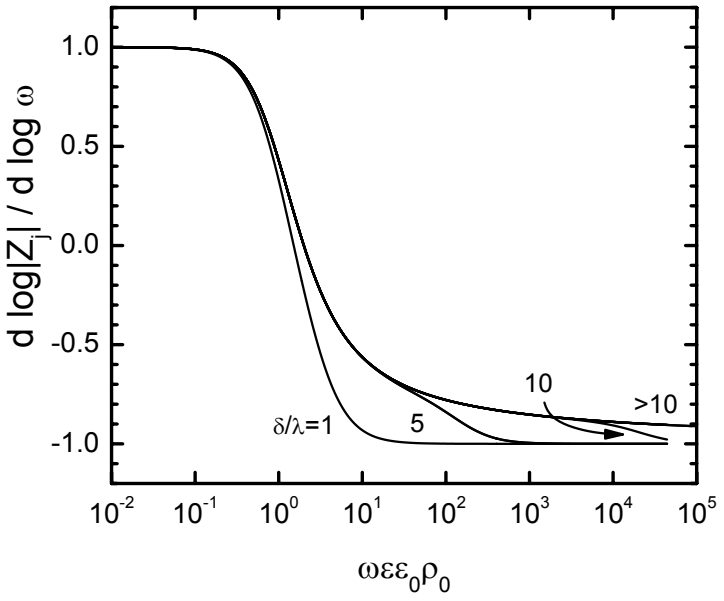

Figure 7-7. The derivative of the logarithm of the magnitude of the imaginary part of the impedance with respect to the logarithm of frequency as a function of dimensionless frequency for the simulations presented in Figure 7-6.

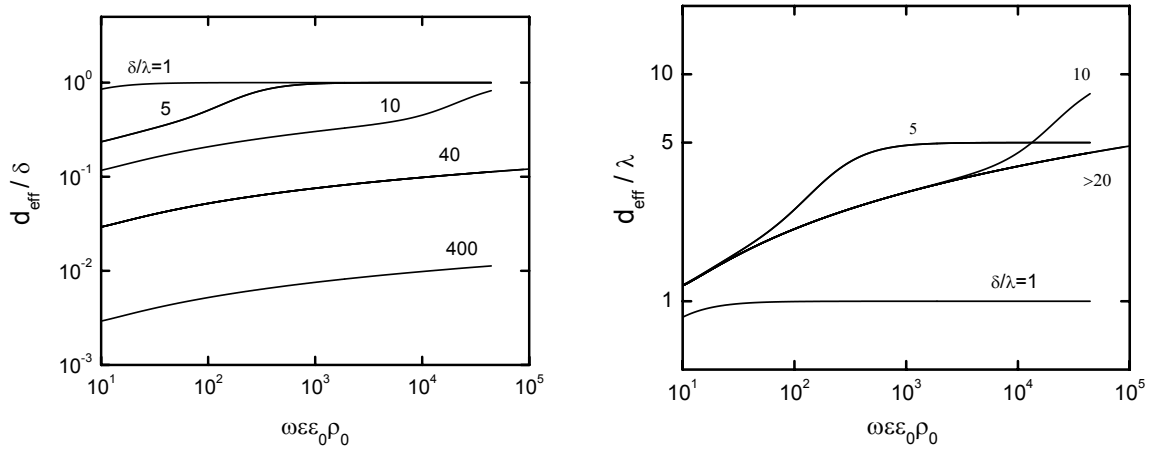

Figure 7-8. The effective film thickness obtained for the simulations presented in Figure 7-6 using equations (6–42) and (7–5): a) normalized by the known film thickness δ; and b) normalized by the characteristic length λ.

equal to the actual film thickness δ for any value of δ/λ. For a broad frequency range and for $\delta/\lambda > 1$, the effective film thickness obtained from the capacitance can clearly be significantly smaller than the actual film thickness. For $\delta/\lambda = 400$, the effective film thickness is two orders of magnitude smaller than the actual film thickness for frequencies as high as $\omega\varepsilon\varepsilon_0\rho_0 = 10^5$.

The simulations show that, for $\delta/\lambda = 5$, the effective film thickness abruptly approaches the actual film thickness at $\omega\varepsilon\varepsilon_0\rho_0 = 10^2$. A similar abrupt change is seen for $\delta/\lambda = 10$ at $\omega\varepsilon\varepsilon_0\rho_0 = 10^4$. The simulations indicate that, while the capacitance obtained from the impedance response for a film with an exponential decay of resistivity should yield, in the limit of infinite frequency, the correct thickness of the film, measurement over a finite frequency range will yield a film thickness that is substantially smaller. As shown in Figure 7-8(b), the effective film thickness is larger than the characteristic length λ. Thus, the film thickness obtained from the capacitance can lie between the actual film thickness δ and the characteristic length λ.

7.3 Application of the Young Model to Niobium and Skin

The results presented above show that, while equation (7–5) will be valid in the limit of infinite frequency, a finite experimentally accessible frequency range may render undetectable the capacitance contributions from a portion of the film. This effect may be significant for cases where the local resistivity varies significantly with position. The effect is illustrated in Figure 7-9. For a constant capacitance C and local resistance R_1, measurement at frequencies much below $\omega = 1/R_1C$ will yield only the resistance R_1 because the capacitor acts as an open circuit at these frequencies. In this case, represented by the upper two RC elements in Figure 7-9, the effective capacitance obtained from equation (6–42) will under predict the thickness of the film. Only the most resistive part of the film is probed by impedance. The capacitance elements that are not observed by impedance can be either at the metal/film interface or at the film/electrolyte interface.

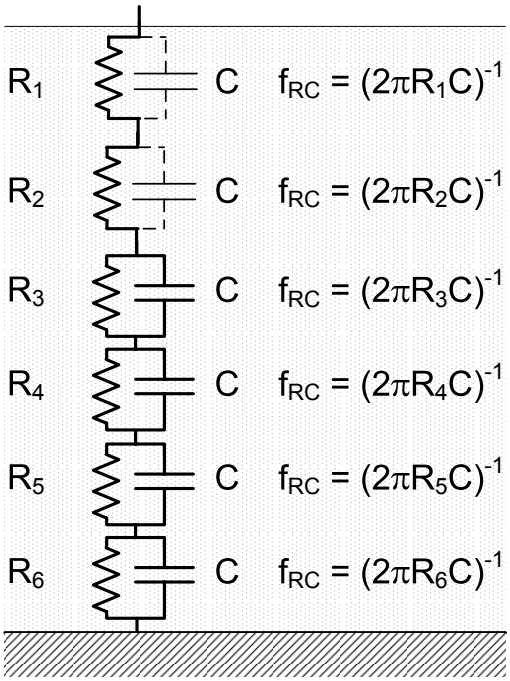

Figure 7-9. Circuit representation of a normal distribution of resistivity in which some capacitance elements are not observed over an experimentally accessible frequency range due to local variation of resisitivity.

The consequence is explored here for the specific case of a film with a uniform dielectric constant and an exponential decay of resistivity. The dielectric response of both Niobium oxide[93,26,104] and skin[27,105] have been described in terms of exponential decays of resistivity. Regression of such a model to the data obtained for anodic dissolution of Niobium at a potential of 6V(SCE) in an acid fluoride medium yielded, for $\varepsilon = 42$, values of $\rho_0 = 2.66 \times 10^9$ Ωcm, $\delta = 30$ nm, and $\lambda = 8$ nm. Under these conditions, the simulation of an exponential decay of resistivity indicates that, for frequencies above 5 kHz, $\alpha \approx 1$ and $d_{\text{eff}}/\delta \approx 1$. A comparison of the Young model to the impedance data for Niobium oxide at a potential of 6V(SCE), presented in Figure 7-10(a), shows that the slope of the Young model is equal to unity for frequencies greater than 5 kHz. The disagreement between the value of $\alpha = 0.90$ obtained from experiment and the value of $\alpha = 1$ obtained from the model indicates that the exponential decay of resistivity provides only an approximate description of the high-frequency behavior of the Nb_2O_5. Nevertheless, the simulation value of $d_{\text{eff}}/\delta = 1$ is consistent with the good agreement

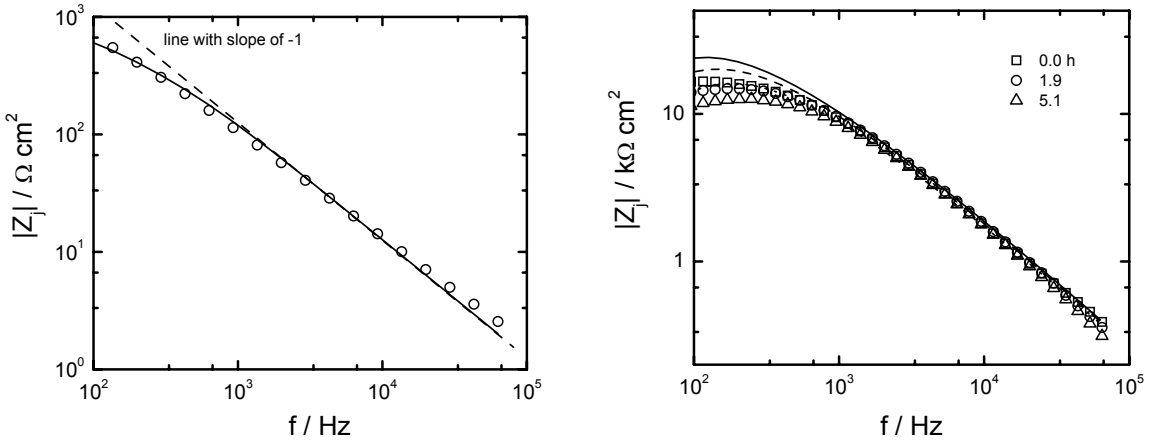

Figure 7-10. Comparison of the Young model to the high-frequency part of the experimental imaginary part of the impedance as a function of frequency: a) Niobium oxide at a potential of 6V(SCE) (see Figure 7-4); and b) human stratum corneum with immersion time as a parameter (see Figure 7-5). The lines represent the model, and symbols represent the data.

found between the thickness estimated from the impedance measurement using equations (6–42) and (7–5) and values obtained by independent methods.

In-vivo impedance experiments obtained by tape-stripping successive layers of skin from human subjects demonstrated that the resistivity of human stratum corneum decays exponentially with position.[27,105] A Young model analysis was therefore performed for the in-vitro data presented in Figure 7-5 for heat-stripped human stratum corneum. Model parameters were obtained by matching the high-frequency portion of the impedance response given in Figure 7-5. The model parameters ε, ρ_0, and λ were selected to match the zero-frequency asymptote for the real part of the impedance, match the characteristic frequency at which the imaginary part of the impedance had a maximum magnitude, and yield a dielectric constant between the dielectric constant of water ($\varepsilon = 80$) and lipid ($\varepsilon = 2$).[108] The value of skin thickness was assumed to be either 20 μm or 40 μm, in keeping with reported values.[27,105] The comparison between the Young model and the data is given in Figure 7-10(b), and the resulting parameters

Table 7-4. Physical properties obtained by matching the high-frequency portion of the impedance response given in Figure 7-5 for heat-stripped stratum corneum in 50 mM buffered $CaCl_2$ electrolyte as a function of immersion time.

Time / h	ρ_0 / Ωcm	ε	δ / μm	λ / μm	α	d_{eff}/δ
0	6×10^8	49	20	1	0.848	0.152
0	6×10^8	49	40	1	0.858	0.078
1.9	5×10^8	49	20	1	0.844	0.143
1.9	5×10^8	49	40	1	0.854	0.076
5.1	4×10^8	49	20	1	0.839	0.139
5.1	4×10^8	49	40	1	0.850	0.074

are presented in Table 7-4. The characteristic length $\lambda = 1$ μm is in agreement with the data presented by Kalia *et al.*,[105] but is smaller than the value $\lambda = 5$ μm reported by Yamamoto and Yamamoto.[27] Values of $\lambda > 1.5$ yielded, for the present experimental data, dielectric constants that were greater than that of water.

The values of α and d_{eff}/δ reported in Table 7-4 were estimated from the simulation at a frequency of 50 kHz. This frequency was chosen for this analysis because it is at the upper limit of the experimental frequency range. As shown in Figure 7-7, the Young model provides only a pseudo-CPE behavior over a broad high-frequency range in which the CPE parameters are weak functions of frequency. The good agreement between the value of α obtained from experiment and from the model suggests that the exponential decay of resistivity provides a good description for the high-frequency behavior of the skin. In addition, the simulation values for d_{eff}/δ are consistent with the observation that the thicknesses estimated from impedance measurements using equations (6–42) and (7–5) were substantially smaller than those reported in the literature. The results presented here support the observation by Oh *et al.* that the capacitance of the skin could not be measured after repeated removal of skin layers reduced the impedance to a value indistinguishable from that of the bathing medium.[109]

The resistivity profiles corresponding to the simulations presented in this section are given in Figure 7-11. The change in resistivity for the Nb_2O_5 film is small enough that the entire dielectric response of the film can be seen in the experimental frequency

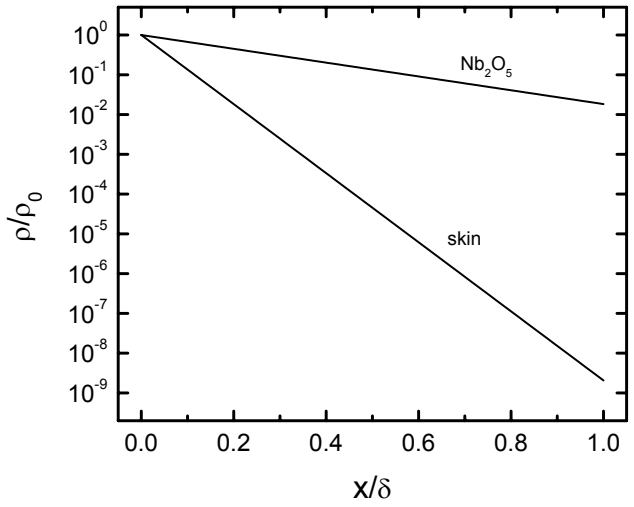

Figure 7-11. Resistivity profiles associated with the simulation of the impedance response for Nb_2O_5 at 6 V(SCE) and skin using a uniform dielectric constant and an exponentially decaying resistivity.

range. In contrast, the change in local resistivity of the skin is much larger, and the capacitance associated with the region of smaller resistivity values is not seen in the experimental frequency range. Accordingly, the thickness estimated from the effective capacitance is much smaller than the actual thickness of the skin. In this case, the thickness obtained from impedance measurements is the thickness of the higher resistivity region. As illustrated in Figure 7-8 for the Young model, δ/λ is the key parameter for determining the meaning of the effective film thickness. When δ/λ is small, the effective thickness determined from the capacitance is the actual film thickness. When δ/λ is large, the effective thickness determined from the capacitance is the thickness of only the resistive portion of the film.

7.4 Conclusions

Methods for determination of effective capacitance from CPE parameters have been employed extensively in the impedance literature. It is not obvious that all the authors who used the relationships derived by Brug *et al.*[3] and presented by Hsu and Mansfeld[6] were fully aware that the former are appropriate only for a surface distribution of time constants and the latter applies only to a normal distribution, as is demonstrated in

Chapter 6. The results presented in the current Chapter illustrate the importance of using the correct formula that corresponds to a given type of distribution. Misuse of the formulas, for example by using an incorrect effective resistance in the calculation of capacitance, may lead to macroscopic errors, since the values of electrolyte resistance, charge transfer resistance and film resistance may be quite different. The selection of the right formula should rest on the knowledge of the system under investigation, obtained by different methods. For instance, local impedance may provide evidence for surface/normal inhomogeneity; whereas, spectroscopic methods may show the presence of films for which properties might be distributed in the normal direction.

The results presented in the current Chapter illustrate that the formulas provided for calculating capacitance do not necessarily provide the correct value even if the appropriate formula for a given type of distribution is used. For instance, the Young model provided an adequate representation of the impedance for the human skin system, however, the application of the Hsu-Mansfeld formula yielded an inaccurate estimate of capacitance. Conversely, the Hsu-Mansfeld formula yielded an accurate estimate of capacitance for the Niobium oxide system, however, regression to the Young model did not provide an adequate representation of the impedance at high-frequency. In addition, the Hsu-Mansfeld formula does not apply to blocking systems where the low-frequency resistance is undefined. This work demonstrates the importance of developing physically reasonable models that account for the CPE. A physical model that accounts for CPE behavior in films is developed in Chapter 8. An analytic expression for capacitance, based on the proposed model, is developed in Chapter 9 and applied to experimental systems.

CHAPTER 8
CPE BEHAVIOR CAUSED BY RESISTIVITY DISTRIBUTIONS IN FILMS

As shown in Chapter 7, the exponential resistivity distribution proposed by Young does not give rise to CPE behavior. The Hsu-Mansfeld formula was developed for normal distributions, but the film thickness obtained using this formula can be too small. The results presented in Chapter 7 illustrated the need to develop mechanisms to account for the CPE. In the present chapter, physical models are developed that can account for the appearance of the CPE in systems where the variation of properties is expected in the direction normal to the electrode.

8.1 Resistivity Distribution

The approach taken by Brug *et al.*[3] to model CPE behavior was to assume that the CPE originated from a surface distribution of time constants with uniform Ohmic and kinetic resistances. The time-constant dispersion therefore was assumed to originate from a distribution of capacitances. The mathematical development of the distribution functions using the methods of Fuoss and Kirkwood[9] yielded a normalizable probability distribution. The method of Fuoss and Kirkwood could not, however, be applied to a normal distribution of time-constants with equal values of capacitance because the resulting probability distribution could not be normalized.

An original approach was employed in the present work in which regression of a measurement model[58,59] to synthetic data yielded a distribution of time constants. The synthetic data were generated following equation (1–1) and were regressed to the Voigt measurement model, expressed as

$$Z_{\mathrm{RC}} = \sum_i \frac{R_i}{1 + j\omega\tau_i} \tag{8–1}$$

yielding a discrete number of time-constants $\tau_i = R_i C_i$ and resistance values R_i that fit the synthetic data. Following the procedure described by Agarwal *et al.*,[58,59] sequential Voigt elements were added to the model until the addition of an element did not improve

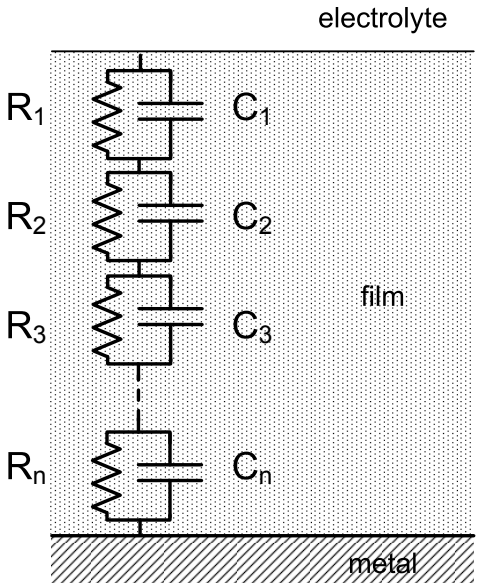

Figure 8-1. A distribution of RC elements that corresponds to the impedance response of a film.

the fit. Model parameters were rejected that included zero within their 95.4 percent (2σ) confidence interval.

According to the model presented in Figure 8-1, the RC time-constants are assumed to be associated with differential layers of the film. The differential capacitance C_i was obtained from the regressed parameters R_i and τ_i by

$$C_i = \tau_i / R_i \tag{8–2}$$

The fits obtained by regression of the RC measurement model to synthetic CPE data are shown in Figures 8-2(a), 8-2(b), and 8-2(c) for the real part of the impedance, the imaginary parts of the impedance, and the phase angle, respectively. The corresponding values for resistance and capacitance are presented in Figures 8-3(a) and 8-3(b) as functions of the time-constant τ. The values of R_i and C_i for the largest time constants do not conform to the pattern seen for the values at other time constants. This can be attributed to the difficulty in fitting blocking systems with a Voigt model, which has a finite impedance at the DC limit. For this reason, these points were not considered in the subsequent analysis.

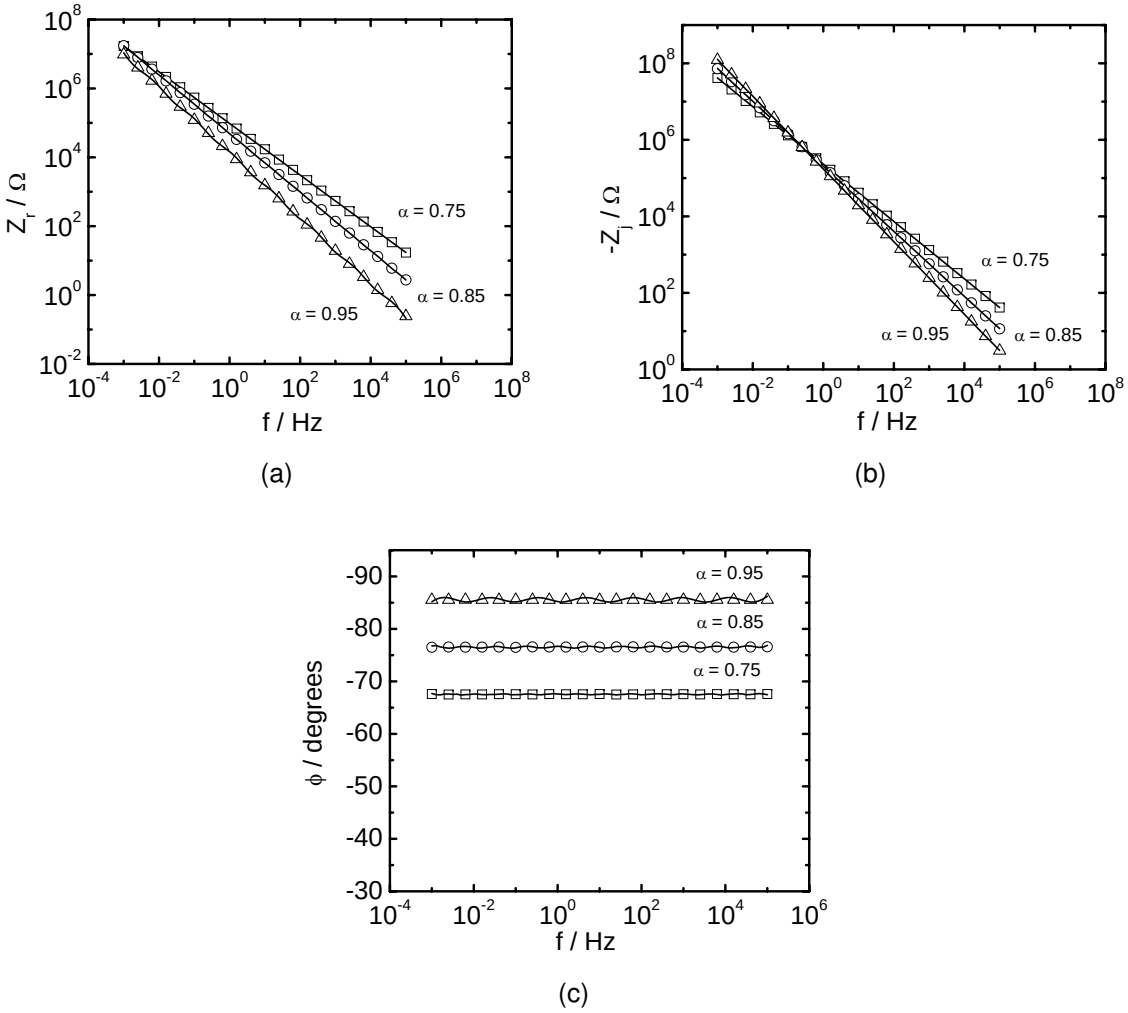

Figure 8-2. Synthetic data (symbols) following equation (1–1) with $Q = 1 \times 10^{-6}\ s^{\alpha}/\Omega\mathrm{cm}^2$ with α as a parameter and the corresponding RC measurement model fits (lines) for a) the real component of the impedance; b) the imaginary component of the impedance; and c) the phase angle. The regressed elements are shown in Figures 8-3(a) and 8-3(b).

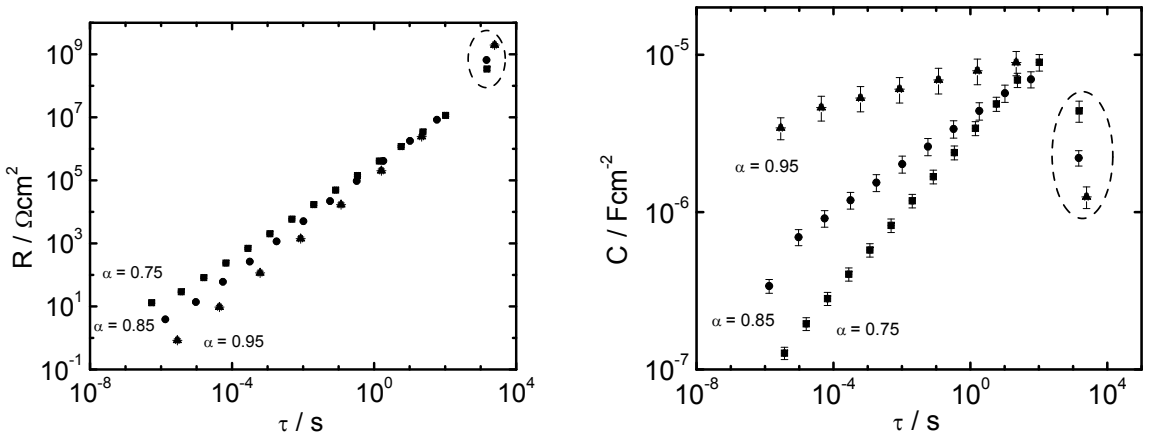

(a) (b)

Figure 8-3. The regressed measurement model parameters as a function of time-constant for the synthetic CPE data shown in Figures 8-2(a) and 8-2(b): a) resistance ; and b) capacitance. The circled values were not used in the subsequent analysis.

A similar approach was taken by Orazem *et al.*,[110] where the distribution of resistance values represented the weighting applied to a distribution of time constants. Orazem *et al.*,[110] however, did not explore the variation of capacitance required to simulate CPE behavior with a Voigt model. As shown in Figure 8-3(b), the capacitance values required to fit the CPE data varied as much as two orders of magnitude. For many experimental systems the variation in local dielectric constant is not expected to encompass such a broad range.

The local capacitance is related to local dielectric constant ϵ_i by

$$C_i = \frac{\epsilon_i \epsilon_0}{d_i} \tag{8–3}$$

where ϵ_0 is the permittivity of vacuum and d_i is the thickness associated with element i. The local resistance can be expressed in terms of a local resistivity ρ_i as

$$R_i = \rho_i d_i \tag{8–4}$$

The time constant

$$\tau_i = \rho_i \epsilon_i \epsilon_0 \tag{8–5}$$

is independent of the element thickness. The variability of capacitance could be interpreted, for a uniform dielectric constant, as being a consequence of a changing element thickness. This interpretation has consequences for local resistivity. Thus, if

$$d_i = \frac{\epsilon \epsilon_0}{C_i} \tag{8–6}$$

the corresponding resistivity is given by

$$\rho_i = \frac{R_i}{d_i} = \frac{\tau_i}{\epsilon \epsilon_0} \tag{8–7}$$

A resistivity distribution model can, therefore, be inferred from the regressed values for τ_i and C_i.

The local resistivity was calculated according to equation (8–7). The discrete resistivity values were arranged monotonically with their corresponding element thickness interpreted in terms of a local position such that

$$x_k = \sum_{i=0}^{k} d_i \tag{8–8}$$

The results are presented in Figure 8-4, where the symbols represent the discrete values of resistivity calculated from the regressed parameters, $\xi = x/\delta$ represents the dimensionless position, and δ is the thickness of the layer

$$\delta = \sum_{i=0}^{n} d_i \tag{8–9}$$

As shown in Figure 8-4, the resistivity follows a nearly linear profile on a logarithmic scale which can be expressed according to

$$\frac{\rho}{\rho_\delta} = \xi^{-\gamma} \tag{8–10}$$

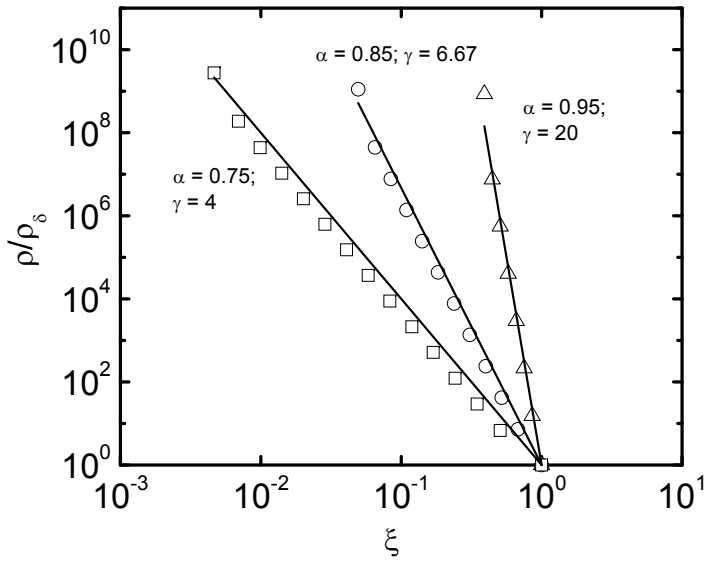

Figure 8-4. Resistivity as a function of dimensionless position. The symbols are the discrete resistivity values calculated from equations (8–6) and (8–7) using the regressed values of resistances and capacitances given in Figures 8-3(a) and 8-3(b) and $\epsilon = 10$. The lines represent equation (8–10) with parameter γ determined according to equation (8–27).

where ρ_δ is the resistivity at $\xi = 1$ and γ is a constant indicating how sharply the resistivity varies. A distribution of resistivity which provides a bounded value for resistivity is proposed to be

$$\frac{\rho}{\rho_\delta} = \left(\frac{\rho_\delta}{\rho_0} + \left(1 - \frac{\rho_\delta}{\rho_0} \right) \xi^\gamma \right)^{-1} \tag{8–11}$$

where ρ_0 and ρ_δ are the boundary values of resistivity at the interfaces.

It is worth noting that, while Agarwal *et al.*[58,59] have insisted that the measurement model, as used for analysis of error structure, has no physical meaning, in the present application, the Voigt measurement model has meaning in terms of the normal distribution of resistivity and dielectric constant. Under assumption of a uniform dielectric constant, an impedance response showing blocking CPE behavior can be explained in terms of a power-law distribution of resistivity. In the subsequent section, equation (8–11) is used to develop models for the impedance response of surface films.

8.2 Impedance Expression

Under assumption that the dielectric constant is uniform, the impedance of the film can be written for an arbitrary resistivity distribution $\rho(x)$ as

$$Z_{\mathrm{f}}(\omega) = \int_0^{\delta} \frac{\rho(x)}{1 + j\omega\epsilon\epsilon_0\rho(x)} dx \tag{8–12}$$

Equation (8–12) can be written in terms of dimensionless position $\xi = x/\delta$

$$Z_{\mathrm{f}}(\omega) = \delta \int_0^{1} \frac{1}{\rho(\xi)^{-1} + j\omega\epsilon\epsilon_0} d\xi \tag{8–13}$$

When the frequency tends toward zero,

$$Z_{\mathrm{f}}(0) = \delta \int_0^{1} \rho(\xi) d\xi \tag{8–14}$$

which can be expressed in terms of the impedance of the circuit shown in Figure 8-1 as

$$Z_{\mathrm{f}}(0) = \sum_1^n R_i \tag{8–15}$$

When the frequency tends toward infinity

$$Z_{\mathrm{f}}(\infty) = \frac{\delta}{j\omega\epsilon\epsilon_0} = \frac{1}{j\omega} \sum_1^n \frac{1}{C_i} = \frac{1}{j\omega C} \tag{8–16}$$

Introduction of the resistivity profile given in equation (8–11) yields

$$Z_{\mathrm{f}}(\omega) = \delta \int_0^{1} \frac{1}{a(\omega) + b\xi^{\gamma}} d\xi \tag{8–17}$$

where

$$a(\omega) = \rho_0^{-1} + j\omega\epsilon\epsilon_0 \tag{8–18}$$

and

$$b = \rho_{\delta}^{-1} - \rho_0^{-1} \tag{8–19}$$

An analytic solution to equation (8–17) is possible for some integer values of γ. For example, when $\gamma = 3$,

$$Z_{\mathrm{f}}(\omega) = \frac{\delta k}{3a(\omega)} \left[\frac{1}{2} \log \frac{(k+1)^3}{1+k^3} + \sqrt{3} \arctan \frac{2-k}{k\sqrt{3}} + \frac{\pi\sqrt{3}}{6} \right] \tag{8–20}$$

where $k = (a(\omega)/b)^{1/3}$.

Under the condition that $\rho_0 >> \rho_\delta$, k is less than 1 for $\omega < (\rho_\delta \epsilon \epsilon_0)^{-1}$, and equation (8–20) reduces to

$$Z_{\mathrm{f}}(\omega) = \frac{2\pi}{3\sqrt{3}} \frac{\delta}{b^{1/3} a(\omega)^{2/3}} = \frac{2\pi}{3\sqrt{3}} \frac{\delta \rho_\delta^{1/3}}{(\rho_0^{-1} + j\omega\epsilon\epsilon_0)^{2/3}} \tag{8–21}$$

Equation (8–21) is derived for the special case of $\gamma = 3$. A general expression of the impedance can be proposed in the same form as

$$Z_{\mathrm{f}}(\omega) = g \frac{\delta \rho_\delta^{1/\gamma}}{(\rho_0^{-1} + j\omega\epsilon\epsilon_0)^{(\gamma-1)/\gamma}} \tag{8–22}$$

where g is a function of γ and, in the case of $\gamma = 3$, $g = 2\pi/3\sqrt{3}$. The comparison of equation (8–22) to the numerical integration of equation (8–17) shows that this expression is general and can be applied for all $\gamma > 2$ over a broad range of frequencies.

The real and imaginary parts of the impedance obtained by numerical integration of equation (8–17) are presented in Figures 8-5(a) and 8-5(b), respectively, with γ as a parameter. The lines represent the evaluation of equation (8–22) where the numerical value of g was obtained at the zero frequency limit of equation (8–22) according to the expression

$$g = \frac{Z_{\mathrm{f}}(0)}{\rho_0^{(\gamma-1)/\gamma} \rho_\delta^{1/\gamma} \delta} \tag{8–23}$$

and where $Z_{\mathrm{f}}(0)$ is obtained from numerical integration of equation (8–17) at $\omega = 0$. Equation (8–22) provides a good agreement with numerical integration of equation (8–17) for frequencies below a characteristic frequency given as $f_\delta = (2\pi\rho_\delta\epsilon\epsilon_0)^{-1}$. Details of algorithm used for the numerical integration of equation (8–17) is provided in Appendix B.

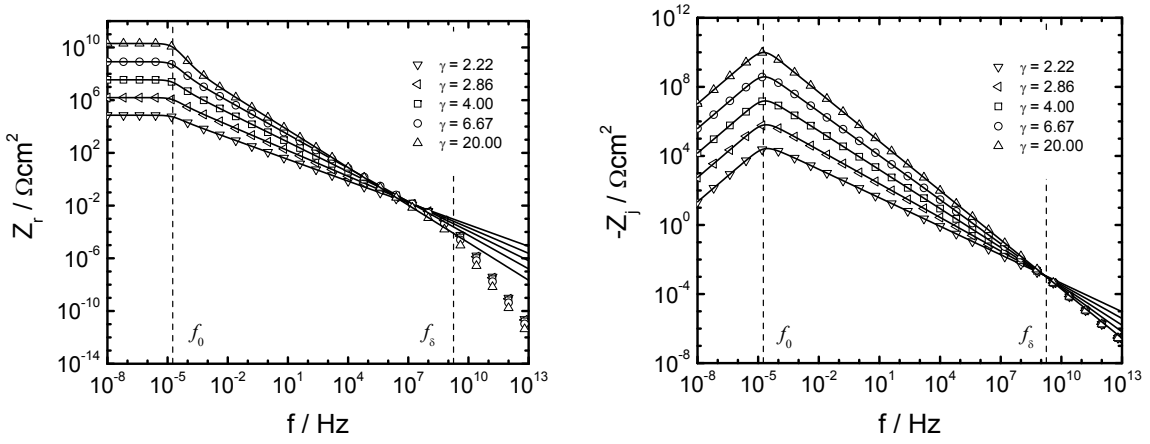

Figure 8-5. A comparison of the impedance response generated by numerical integration of equation (8–17) (symbols) and the analytic expression provided by equation (8–22) (lines) with $\rho_0 = 1 \times 10^{16}\ \Omega\text{cm}$, $\rho_\delta = 100\ \Omega\text{cm}$, $\epsilon = 10$, $\delta = 100$ nm, and γ as a parameter: a) the real component of impedance; and b) the imaginary component of impedance.

A numerical evaluation was used to confirm that g can be expressed as a function of only γ and is independent of other system parameters. As shown by Figure 8-6, the value of g ranges between 1 and 1.6 for $0 \leq 1/\gamma \leq 0.5$. An interpolation formula

$$g = 1 + 2.88\gamma^{-2.375} \tag{8–24}$$

could be obtained that adequately represents the function in the range $0 \leq 1/\gamma \leq 0.5$. As shown in Figures 8-5(a) and 8-5(b), the analytic expression provided by equation (8–22) is in agreement with the numerical solution of equation (8–17) for $\omega < (\rho_\delta \epsilon \epsilon_0)^{-1}$. In the low-frequency range, for $\omega < (\rho_0 \epsilon \epsilon_0)^{-1}$ (or $f < f_0$, as shown in Figure 8-5, where $f_0 = (2\pi\rho_0 \epsilon \epsilon_0)^{-1}$),

$$Z_r = Z_{\text{f}}(0) = g\rho_0^{(\gamma-1)/\gamma}\rho_\delta^{1/\gamma}\delta \tag{8–25}$$

as defined in equation (8–14) or, in the limit of $\omega = 0$ in equation (8–22). In the high-frequency range where $\omega > (\rho_\delta \epsilon \epsilon_0)^{-1}$, $Z_j(\omega)$ is equal to $1/j\omega C$ for all values of γ, in agreement with equation (8–16).

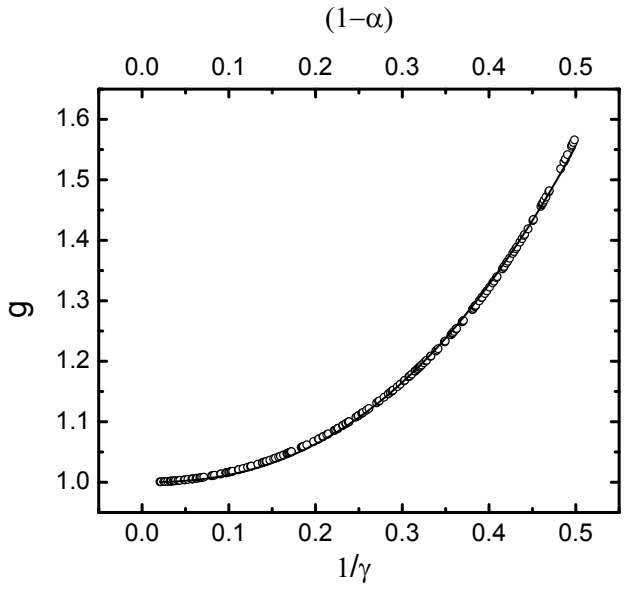

Figure 8-6. The numerical evaluation of g as a function of $1/\gamma$ where the symbols represent results obtained from equation (8–23). The line represents the interpolation formula given as equation (8–24).

Equation (8–22) is in the form of the CPE for $\omega > (\rho_0 \epsilon \epsilon_0)^{-1}$, *i.e.,*

$$Z_{\mathrm{f}}(\omega) = g \frac{\delta \rho_\delta^{1/\gamma}}{(j\omega\epsilon\epsilon_0)^{(\gamma-1)/\gamma}} = \frac{1}{(j\omega)^\alpha Q} \tag{8–26}$$

Therefore, equation (8–22) yields the impedance given by equation (1–1) for $(\rho_0 \epsilon \epsilon_0)^{-1} < \omega < (\rho_\delta \epsilon \epsilon_0)^{-1}$. Inspection of equation (8–26) suggests that

$$\alpha = \frac{\gamma - 1}{\gamma} \tag{8–27}$$

or $1/\gamma = 1 - \alpha$ where $\gamma \geq 2$ for $0.5 \leq \alpha \leq 1$. Thus,

$$g = 1 + 2.88(1 - \alpha)^{2.375} \tag{8–28}$$

and

$$Q = \frac{(\epsilon\epsilon_0)^\alpha}{g\delta\rho_\delta^{1-\alpha}} \tag{8–29}$$

Thus, equation (8–27) provides the analytic expression for the relationship between α and γ suggested by the results presented in Figure 8-4.

The impedance corresponding to equation (8–22) is presented in Figure 8-7 for

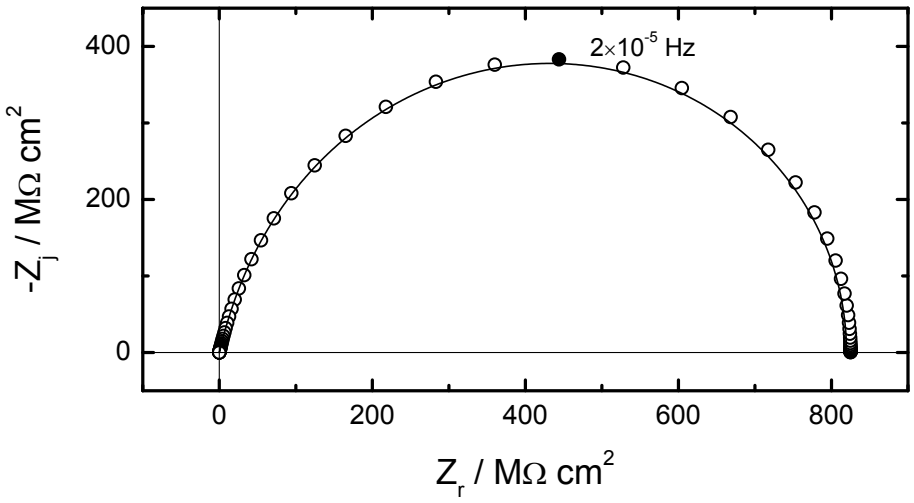

Figure 8-7. Nyquist representation of the impedance given in Figure 8-5 for $\gamma = 6.67$. The marked impedance at a frequency of 2×10^{-5} Hz is close to the characteristic frequency $f_0 = 1.8 \times 10^{-5}$ Hz.

$\gamma = 6.67$ ($\alpha = 0.85$) in Nyquist coordinates. The high and low-frequency behaviors of the impedance are not symmetric. In high frequency, a CPE response is evident; whereas, the low frequency behavior corresponds to a pure capacitive loop.

8.3 Discussion

An analytic expression for the impedance response associated with a power-law distributions of resistivity was developed in the previous section. It is useful to explore the conditions under which this model can be used to extract physical parameters from experimental data. It is also useful to compare this impedance response to the impedance obtained from other resistivity distributions reported in the literature.

8.3.1 Extraction of Physical Parameters

The frequency range for which the impedance response provided by equation (8–17) is consistent with the CPE is presented in Figure 8-5. Generally, ϵ is known from independent measurements. Operation in the frequency range $f_0 < f < f_\delta$ provides only the product $\delta \rho_\delta^{1-\alpha}$ given by equation (8–29). Therefore, measurements for $f > f_\delta$ are required to obtain separately the film thickness δ and the interfacial resistivity ρ_δ.

Measurements for $f < f_0$ are required to obtain the interfacial resistivity ρ_0. Application to experimental data is presented in Chapter 9.

8.3.2 Comparison to Young Model

The impedance corresponding to a power-law distribution of resistivity (equation (8–22)) can be compared to the impedance obtained using an exponential resistivity distribution as proposed by Young.[26,104] The Young resistivity distribution can be expressed as

$$\rho(x) = \rho_0 \exp(-x/\lambda) \tag{8–30}$$

where ρ_0 is the resistivity at the surface and λ represents a characteristic length. An analytic expression for the impedance resulting from equation (8–12) can be found for an exponential distribution of resistivity to be[106,107]

$$Z_Y(\omega) = -\frac{\lambda}{j\omega\epsilon\epsilon_0} \ln\left[\frac{1 + j\omega\epsilon\epsilon_0\rho_0 \mathrm{e}^{-\delta/\lambda}}{1 + j\omega\epsilon\epsilon_0\rho_0}\right] \tag{8–31}$$

Equation (8–31) is known as the Young impedance[26,104] and is widely used to model impedance data arising from a film.

Hirschorn *et al.*[111] have shown that the Young impedance yields a pseudo-CPE response in which the CPE parameters, α and Q, are weak functions of frequency over a limited frequency range. In addition, the range for α obtained from a Young model is limited to values greater than roughly 0.8.

Simulation results are presented in Figure 8-8 for power-law and Young resistivity distributions. The parameters used for the power-law distribution were $\rho_0 = 1 \times 10^{12}\ \Omega\mathrm{cm}$, $\rho_\delta = 2 \times 10^{7}\ \Omega\mathrm{cm}$, and $\gamma = 6.67$. The corresponding simulations for the Young distribution used the same value of ρ_0 and $\lambda = 9.24$ nm, yielding the value of ρ_δ used in the power-law simulations. In this case, the characteristic frequency $f_\delta = 9$ kHz, well below the largest frequency of 100 kHz used in the calculations.

An inflection is seen at $f = 9$ kHz in the plots given in Figures 8-8(b) and 8-8(c). The resistivity profiles used in the calculations are presented in Figure 8-9(a),

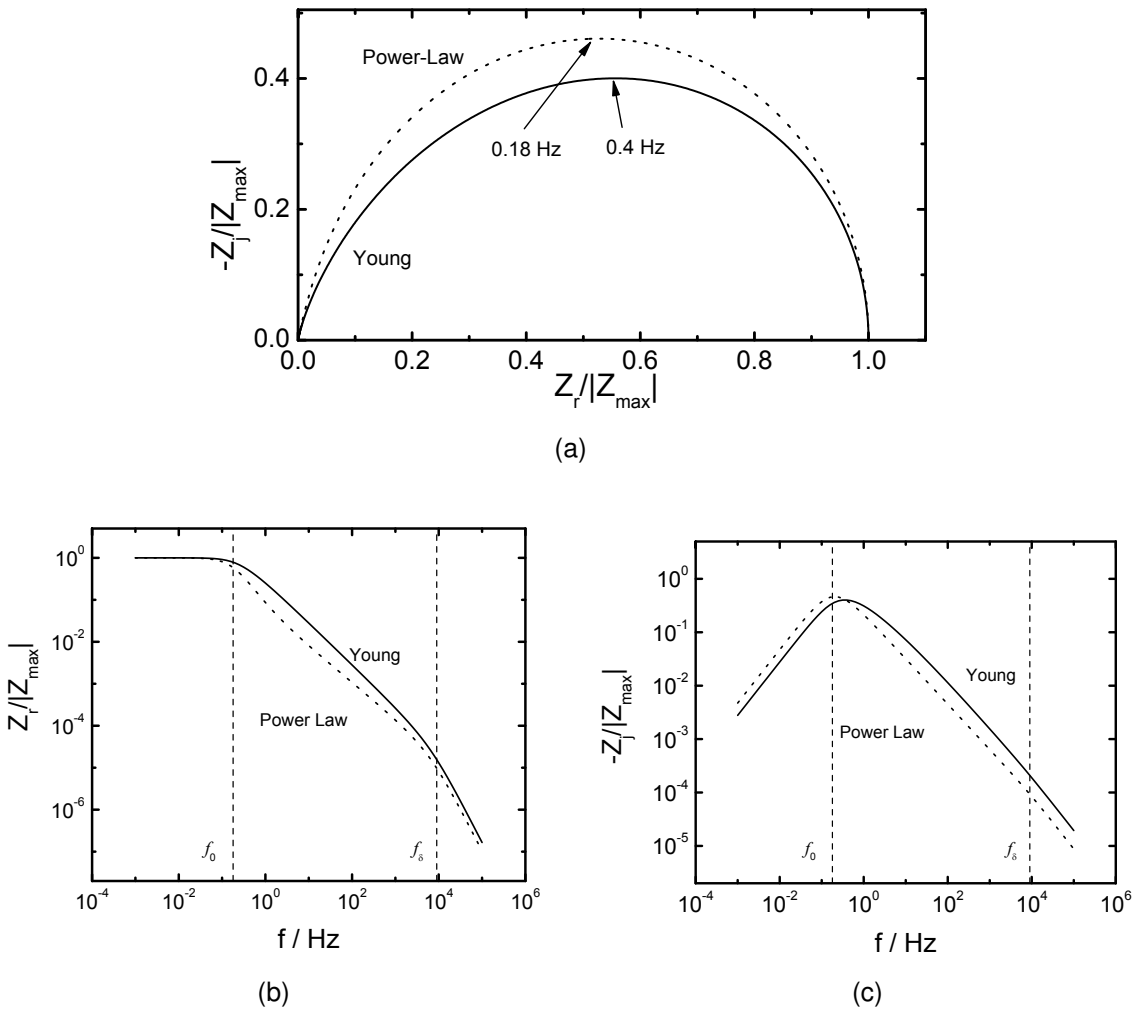

Figure 8-8. Normalized impedance response associated with normal distributions of resistivity with a fixed dielectric constant $\epsilon = 10$ and a thickness $\delta = 100$ nm. The dashed line provides the results for a resistivity given as equation (8–11) with $\rho_0 = 1 \times 10^{12}\ \Omega\mathrm{cm}$, $\rho_\delta = 2 \times 10^{7}\ \Omega\mathrm{cm}$, and $\gamma = 6.67$. The solid line provides the result for a Young model with a resistivity profile following equation (8–30) with the same values of ρ_δ and ρ_0, yielding $\lambda = 9.24$ nm. a) Nyquist plot; b) real part of the impedance; and c) imaginary part of the impedance.

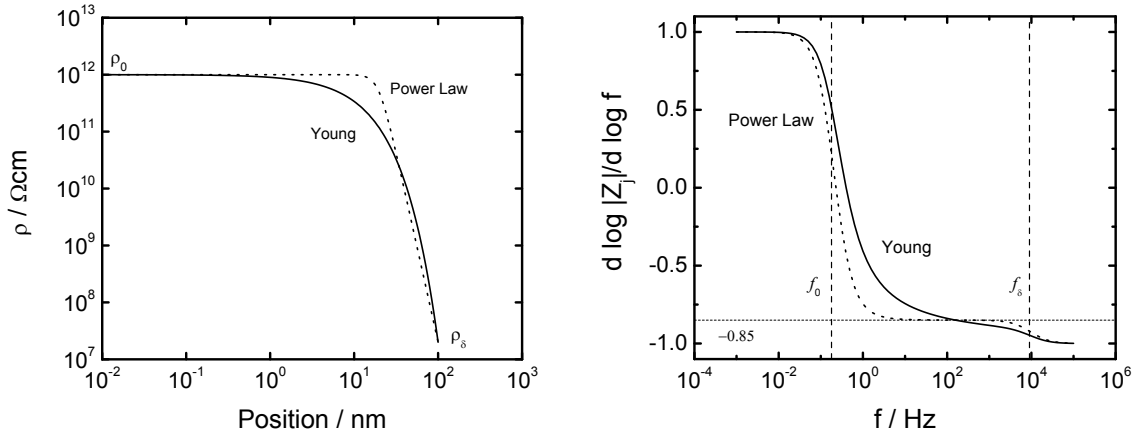

Figure 8-9. Resistivity profiles and estimated values of α for the simulations reported in Figure 8-8: a) resistivity versus position; and b) the value of $d\log|Z_j|/d\log f$ obtained from the slopes given in Figure 8-8(c).

and the corresponding values of $d\log|Z_j|/d\log f$ are presented in Figure 8-9(b). As discussed by Orazem *et al.*,[87] the slope $d\log|Z_j|/d\log f$ is equal to $-\alpha$ for a system that shows CPE behavior. The value of α for the power-law model at high frequencies is independent of frequency in the range of 1 Hz to 9 kHz, but changes abruptly to a value of unity for frequencies higher than 9 kHz. A pseudo-CPE behavior is seen for the Young model at frequencies between 1 Hz and 9 kHz, but, as is seen for the power-law model, α changes abruptly to a value of unity for frequencies higher than 9 kHz. For both distributions, the low-frequency response yields $\alpha = 1$, as was mentioned previously for the power-law model. Under conditions where f_δ is within the measured frequency range, CPE behavior, or, for the Young model, pseudo-CPE behavior, is not seen at the high-frequency limit. For such a case, C_{eff} can be directly determined at $f > f_\delta$.

8.3.3 Variable Dielectric Constant

If the resistivity distribution results from an inhomogeneous layer composition, then a profile for the dielectric constant may also be expected. The variation of dielectric constant, however, should be small and generally limited to less than a factor of 2 or 3. The present work shows that a distribution of RC time constant over many orders of

magnitude is required to yield CPE behavior over a broad frequency range; thus, this distribution cannot be explained by variation of dielectric constant alone. The present limiting case of a distributed resistivity and a uniform dielectric constant accounts for the dominant effects, since a variable dielectric constant represents a second order effect as compared to the variable resistivity.

8.4 Conclusions

The present work shows that, under assumption that the dielectric constant is independent of position, a normal power-law distribution of local resistivity is consistent with the CPE. The power-law resistivity distribution provides a physically reasonable model that offers an interpretation of the CPE for a broad class of systems where a variation in properties is expected in the direction normal to the electrode. The analytic expression for the resulting impedance provides a useful relationship between system properties and CPE parameters. Application of this model to experimental systems is presented in Chapter 9, where physical properties are estimated from the CPE response.

CHAPTER 9
APPLICATION OF THE POWER-LAW MODEL TO EXPERIMENTAL SYSTEMS

The objective of the present work is to develop a method to extract physically meaningful parameters from impedance data yielding CPE behavior corresponding to systems for which a variation of properties is expected in the direction normal to the electrode. The resulting approach is applied to experimental data. The data re-examined here were already published, and the experimental details may be found in the references.

9.1 Method

In many cases, the impedance response follows CPE behavior, expressed for blocking systems by equation (1–1) and for reactive systems by equation (1–2). For $(\rho_0\epsilon\epsilon_0)^{-1} < \omega < (\rho_\delta\epsilon\epsilon_0)^{-1}$, equation (8–22) takes the form of equation (1–1) with Q given by equation (8–29). Equation (8–29) provides a new means of relating CPE parameters to the physical properties of the film.

The frequency range for which the impedance response provided by equation (8–22) is consistent with the CPE is presented in Figure 9-1 for $\gamma = 4$ ($\alpha = 0.75$). The symbols represent the product of Q, obtained from equation (8–29), with the impedance, obtained by numerical integration of equation (8–12) where the resistivity is given by equation (8–11). The line represents $(j\omega)^{-0.75}$ in agreement with equation (1–1), and the characteristic frequencies are defined in terms of the parameters associated with equation (8–11) as $f_\delta = (2\pi\rho_\delta\epsilon\epsilon_0)^{-1}$ and $f_0 = (2\pi\rho_0\epsilon\epsilon_0)^{-1}$.

The impedance behaviors near frequencies f_0 and f_δ are presented in Nyquist format in Figures 9-2(a) and 9-2(b), respectively. The response is capacitive at frequencies lower than f_0 and at frequencies higher than f_δ. The impedance response reflects the distributed resistivity at frequencies between f_0 and f_δ.

Even if ϵ is known from independent measurements, operation in the frequency range $f_0 < f < f_\delta$ provides only the product $\delta\rho_\delta^{1-\alpha}$ given by equation (8–29). Therefore, measurements for $f > f_\delta$ are required to obtain separately the film thickness δ and

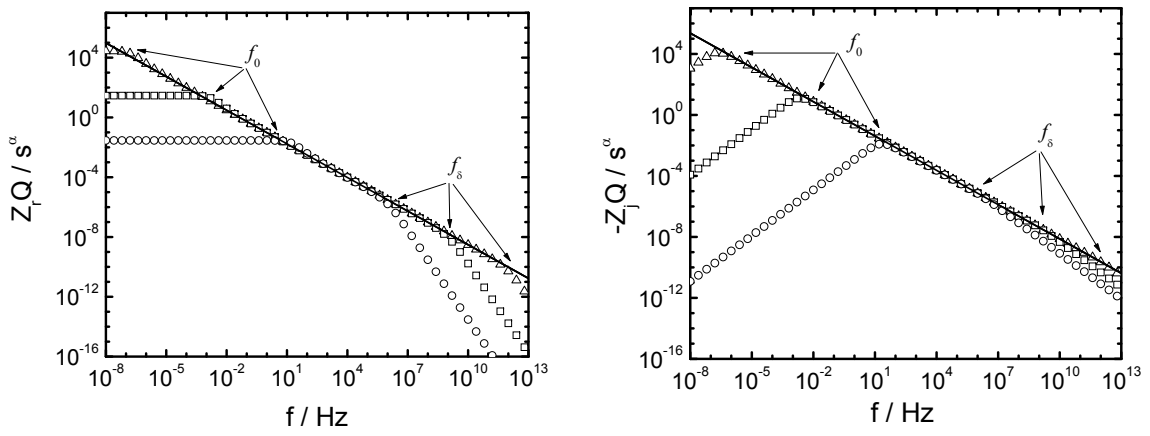

Figure 9-1. Representation of ZQ where Z is generated by numerical integration of equation (8–12) and Q is obtained from equation (8–29) for $\gamma = 4$ $(\alpha = 0.75)$ and $\epsilon = 10$ with ρ_0 and ρ_δ as parameters: a) the real component of impedance; and b) the imaginary component of impedance. The line represents $(j\omega)^{-0.75}$ in agreement with equation (1–1). The symbols represent calculations performed for $\triangle$ $\rho_0 = 10^{18}$ Ωcm and $\rho_\delta = 10^{-1}$ Ωcm; $\square$ $\rho_0 = 10^{14}$ Ωcm; $\rho_\delta = 10^{2}$ Ωcm; and $\bigcirc$ $\rho_0 = 10^{10}$ Ωcm; $\rho_\delta = 10^{5}$ Ωcm.

the interfacial resistivity ρ_δ. Measurements for $f < f_0$ are required to obtain the interfacial resistivity ρ_0. The maximum experimental frequency range for electrochemical systems is generally considered to be of the order of 1 mHz to 100 kHz. The impedance response given in Figure 9-1 is presented for a larger frequency range to explore the consequence of the large variation possible in the resistivity parameters ρ_0 and ρ_δ.

9.2 Results and Discussion

As discussed above, the characteristic frequencies f_0 and f_δ define the range for which the system behaves as a CPE. In addition, the characteristic frequency f_0 represents the frequency at the maximum magnitude of the imaginary part of the impedance. Since the frequencies f_0 and f_δ depend on the film properties ϵ, ρ_0, and ρ_δ, the subsequent discussion is organized according to the respective values of ρ_0 and ρ_δ.

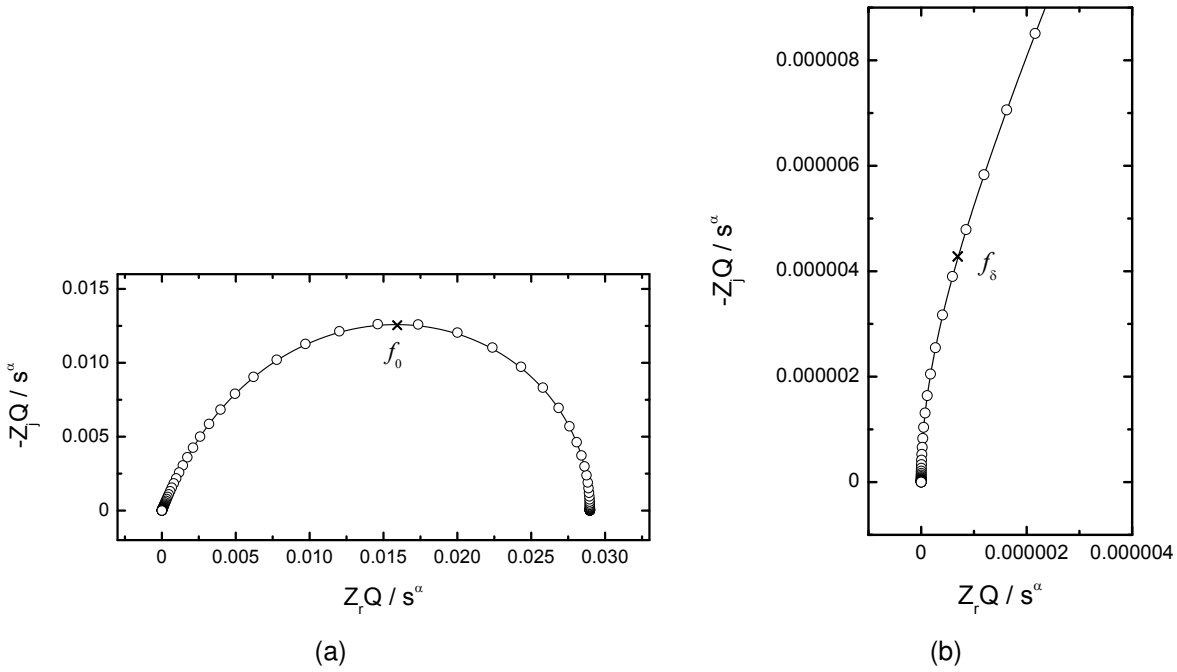

Figure 9-2. Nyquist plot of the data presented in Figure 9-1 for $\rho_0 = 10^{10}$ Ωcm and $\rho_\delta = 10^5$ Ωcm: a) plot showing the characteristic frequency $f_0 = (2\pi\rho_0\epsilon\epsilon_0)^{-1} = 18$ Hz; and b) zoomed region showing $f_\delta = (2\pi\rho_\delta\epsilon\epsilon_0)^{-1} = 1.8 \times 10^6$ Hz.

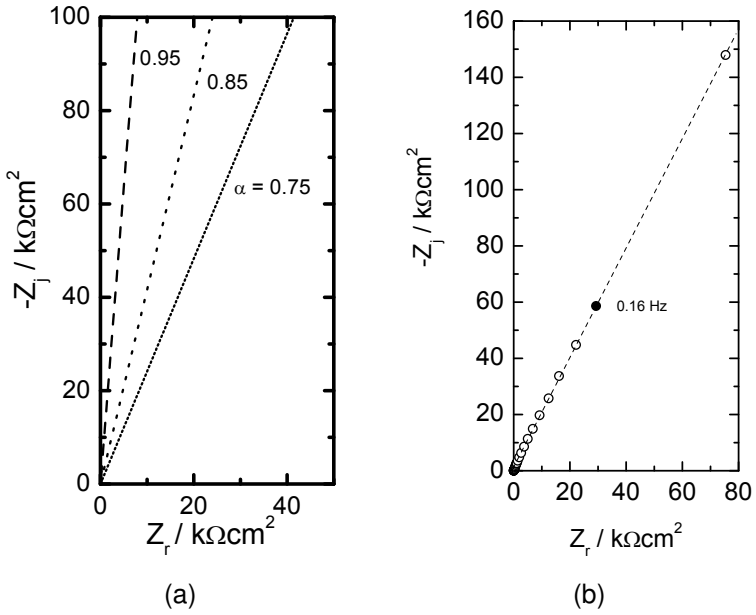

Figure 9-3. Impedance response associated with a frequency range which excludes the characteristic frequencies f_0 and f_δ: a) simulations obtained for $\epsilon = 10$ and with γ as a parameter; and b) experimental Nyquist plot for passive Aluminum in a 0.1 M Na_2SO_4 electrolyte (data taken from Jorcin *et al.*[5]). The dashed line represents a CPE fit to the data according to equation (1–1).

9.2.1 Aluminum Oxide (Large ρ_0 and Small ρ_δ)

When the resistivity limit ρ_δ is small, the high-frequency domain corresponds to a CPE. When the resistivity limit ρ_0 is very large, its influence on the impedance response can be outside the experimentally accessible frequency range. In this case, the resulting impedance response is that of a blocking electrode, as is seen in Figure 9-3(a) for a frequency range that excludes f_0 and f_δ. Such a behavior can be observed experimentally, as is shown in Figure 9-3(b) for passive Aluminum in a 0.1 M Na_2SO_4 electrolyte.[5] The dashed line in Figure 9-3(b) represents a CPE fit to the data according to equation (1–1).

The effective capacitance of a film can be expressed as

$$C_{\text{eff,f}} = \frac{\epsilon\epsilon_0}{\delta} \tag{9–1}$$

Introduction of equation (9–1) into equation (8–29) yields

$$C_{\text{eff,f}} = Q(\rho_\delta \epsilon \epsilon_0)^{1-\alpha} g \tag{9–2}$$

When $\alpha = 1$, $g = 1$ and, as shown by equation (9–2), the CPE parameter Q represents the capacitance of the layer. The parameters Q and α in equation (9–2) can be obtained from graphical analysis of impedance data,[87] and ϵ is often known from independent measurements. The parameter ρ_δ cannot be known exactly for data showing high-frequency CPE behavior. Nevertheless, equation (9–2) may be attractive for analysis of CPE data for which a polarization resistance cannot be estimated due to blocking behavior in the measured frequency range or for which the polarization resistance is influenced by phenomena not associated with the dielectric response of the film.

Although the value of ρ_δ is unknown for data showing high-frequency CPE behavior, an upper bound on its value can be defined because the characteristic frequency f_δ must be larger than the largest measured frequency $f_{\max}$. Thus, a maximum value of ρ_δ can be obtained

$$\rho_{\delta,\max} = \frac{1}{2\pi\epsilon\epsilon_0 f_{\max}} \tag{9–3}$$

The relationship between $\rho_{\delta,\max}$ and $f_{\max}$ for different values of dielectric constant is shown in Figure 9-4. Since equation (9–2) can be written

$$C_{\text{eff,f}} = Q(2\pi f_\delta)^{\alpha-1} g \tag{9–4}$$

a similar bound on the effective capacitance can be found to be

$$C_{\max} = Q(2\pi f_{\max})^{\alpha-1} g \tag{9–5}$$

Therefore,

$$\frac{C_{\text{eff,f}}}{C_{\max}} = \left(\frac{f_\delta}{f_{\max}}\right)^{\alpha-1} = \left(\frac{\rho_{\delta,\max}}{\rho_\delta}\right)^{\alpha-1} \tag{9–6}$$

The uncertainty in calculating effective capacitance due to uncertainty in the value of ρ_δ can be ascertained from the results presented in Figure 9-5. When α is close to

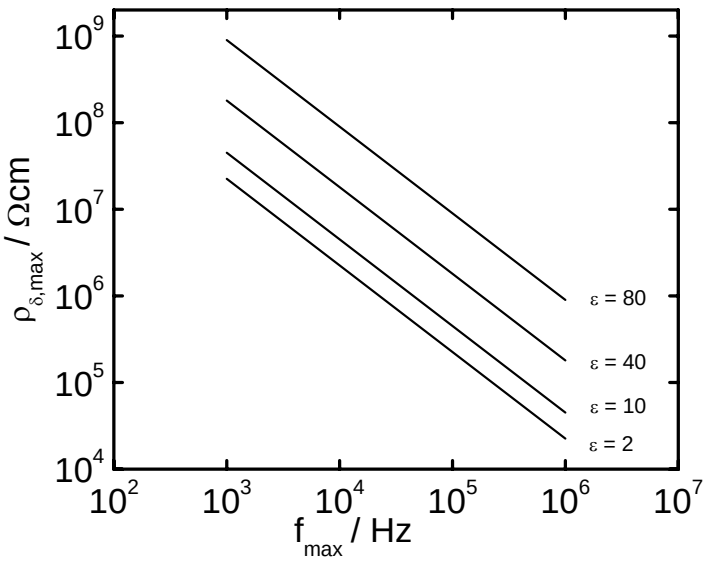

Figure 9-4. The value of $\rho_{\delta,\max}$ obtained from equation (9–3) with dielectric constant as a parameter.

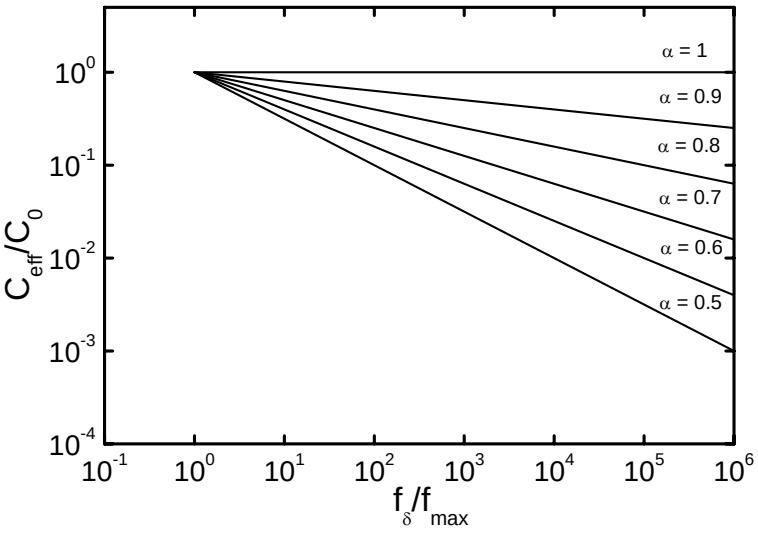

Figure 9-5. The calculated value of $C_{\mathrm{eff,f}}$ as a function of the cut-off frequency f_δ with α as a parameter. C_0 is the capacitance at the maximum frequency experimentally measured.

unity, the estimation of $C_{\text{eff,f}}$ from equation (9–2) is relatively insensitive to the value of ρ_δ; whereas, for $\alpha = 0.5$, an uncertainty of 2 orders of magnitude in ρ_δ results in an uncertainty of 1 order of magnitude in $C_{\text{eff,f}}$.

In Figure 9-3(b), the impedance of a passive aluminum electrode was given where the highest measured frequency $f_{\max}$ was 30 kHz. The corresponding CPE parameters were $\alpha = 0.77$ and $Q = 1.7 \times 10^{-5}\ \text{Fcm}^{-2}\text{s}^{-0.23}$. Following equation (9–5), $C_{\max} = 1.1\ \mu$F/cm^2. Under assumption of a dielectric constant of 11.5, a minimum film thickness can be estimated to be 9 nm. Following equation (9–3), $\rho_{\delta,\max} = 5.2 \times 10^6\ \Omega\text{cm}$. In a fashion similar to the development of $\rho_{\delta,\max}$, a minimum value $\rho_{0,\min}$ can be obtained from the lowest measured frequency $f_{\min} = 0.1$ Hz to be $1.6 \times 10^{12}\ \Omega\text{cm}$. Therefore, the minimum amplitude of resistivity variation within the alumina layer is 5.2×10^6 to $1.6 \times 10^{12}\ \Omega\text{cm}$. These values fall within the ranges typical of semiconductors and insulators, respectively.

The application of the Hsu-Mansfeld formula, given as equation (6–42), is not possible because a capacitive loop is not apparent in the experimental results, and a value for R_{f} cannot be estimated. This example shows that application of a power-law distribution of resistivity allows estimation of film thickness of a blocking film, for which the existing formulas do not apply. In the present case, the lower limit for the thickness and the minimum range of resistivity values are determined.

9.2.2 Stainless Steel (Finite ρ_0 and Small ρ_δ)

When ρ_0 is sufficiently small, the characteristic frequency f_0 falls within the experimental frequency range. Under these conditions, a finite value is obtained for the impedance at low frequencies.

An experimental example can be given with the impedance of oxides developed on stainless steel. Experimental data are shown in Figure 9-6(a) for the impedance response of a Fe17Cr disk (polarized in the passive domain for 1 h at -0.1 V measured with respect to a mercury/mercurous sulfate electrode in saturated K_2SO_4) in deaerated

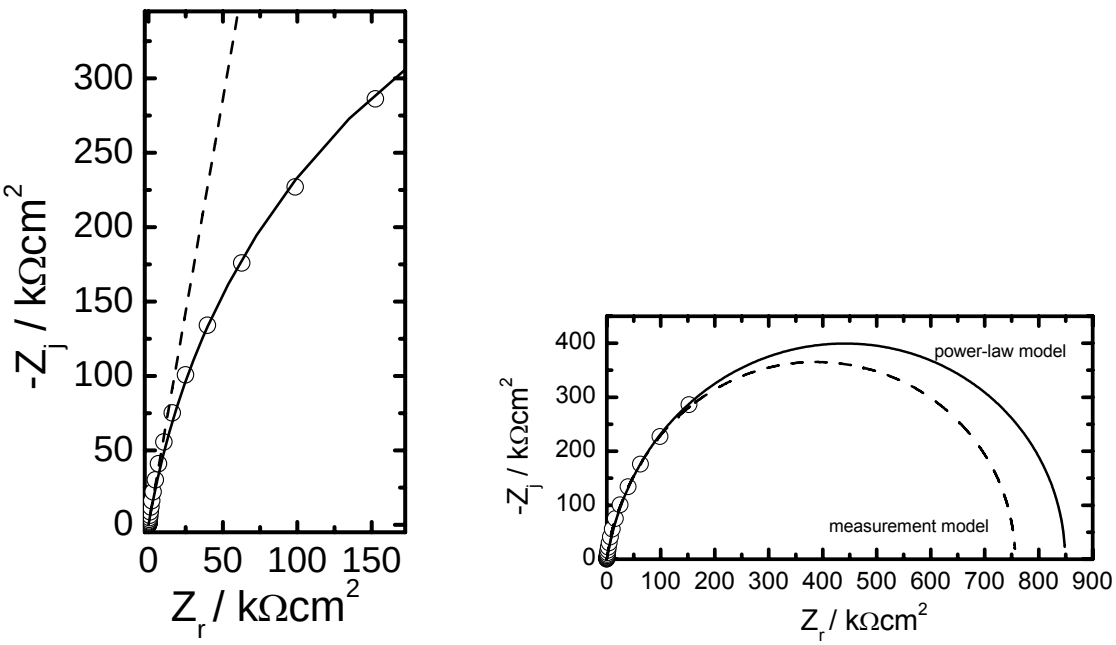

Figure 9-6. Impedance diagram of oxide on a Fe17Cr stainless steel disk (symbols): a) experimental frequency range. The solid line is the power-law model following equation (8–22) with parameters $\rho_0 = 4.5 \times 10^{13}\ \Omega\mathrm{cm}$, $\rho_\delta = 450\ \Omega\mathrm{cm}$, $\delta = 3$ nm, $\epsilon = 12$, and $\gamma = 9.1$, and the dashed line is the CPE impedance with $\alpha = 0.89$ and $Q = 3.7 \times 10^{-5}\ \mathrm{Fcm^{-2}s^{-0.11}}$; and b) extrapolation to zero frequency where the dashed line represents the fit of a Voigt measurement model and the solid line represents the fit of the power-law model.

pH 4, 0.05M Na_2SO_4 electrolyte. The impedance diagram resembles blocking CPE behavior; however, the response is not a pure CPE as was the case for the aluminum data presented above.

From XPS analysis, Frateur *et al.*[112] showed that the passive film developed on Fe17Cr consisted of an inner layer of Fe_2O_3 and Cr_2O_3 covered by an outer layer of $Cr(OH)_3$ and that the thickness was about 3 nm. In the following, a value of 12 was assumed for ϵ, which corresponds to the dielectric constant for Fe_2O_3 and Cr_2O_3. Graphical analysis of the impedance yielded $\alpha = 0.89$ and $Q = 3.7 \times 10^{-5}\ \mathrm{Fcm^{-2}s^{-0.11}}$. The film thickness δ being known, equation (8–29) was used to obtain $\rho_\delta = 450\ \Omega\mathrm{cm}$, which is a typical value for a semiconductor. As shown in Figure 9-6(a), the impedance

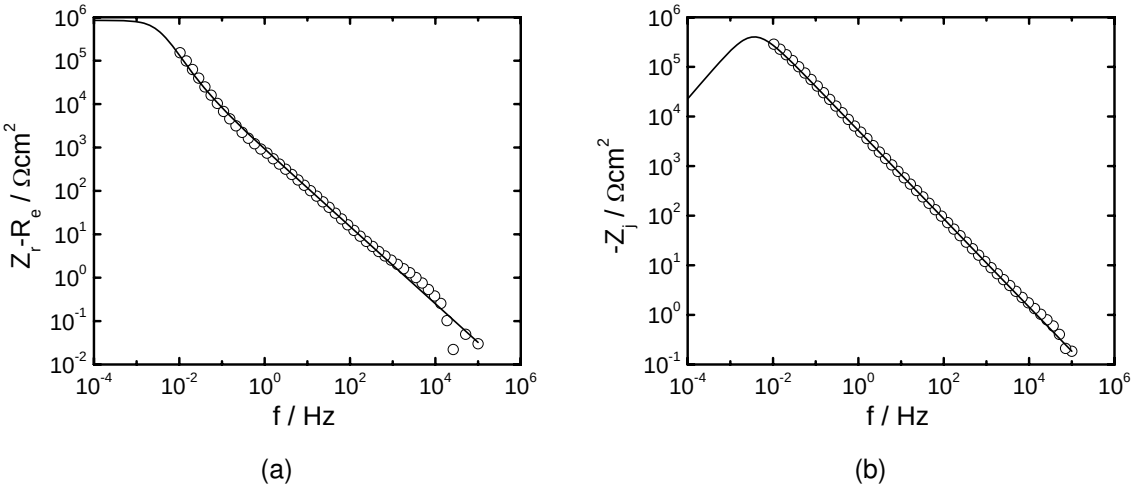

Figure 9-7. Impedance response of oxide on a Fe17Cr stainless steel disk (symbols) and the theoretical model (line) with parameters reported in Figure 9-6(a): a) the real component; and b) the imaginary component. The electrolyte resistance value was $23\ \Omega\mathrm{cm}^2$.

response does not follow a straight line, but its shape suggests a finite low-frequency impedance. As shown in Figures 9-6 and 9-7, introduction of $\rho_0 = 4.5 \times 10^{13}\ \Omega\mathrm{cm}$ into equation (8–11) provided a calculated response that agrees with the experimental results. This value of ρ_0 corresponds to an insulator and, with $\epsilon = 12$, the maximum of the imaginary impedance is expected to occur at $f_0 = 3.3$ mHz, which is smaller than the lowest measured frequency.

If ex-situ measurements are not available for the evaluation of layer thickness, only an estimate of δ is possible through use of equation (8–29) due to uncertainty in the parameter ρ_δ. Equation (9–3) provides an upper bound on ρ_δ. For this experiment, with a maximum measurement frequency of 100 kHz and with $\epsilon = 12$, $\rho_{\delta,\max} = 1.5 \times 10^6\ \Omega\mathrm{cm}$. A lower bound for ρ_δ may also be estimated on physical grounds. For an oxide, for example, ρ_δ is not expected to be smaller than minimum resistivity value expected for semiconductors, *i.e.,* $1 \times 10^{-3}\ \Omega\mathrm{cm}$. Using equation (8–29), this conservative range of ρ_δ yields an estimated layer thickness of $\delta = 1.2$ to 12.6 nm, which encompasses the value of 3 nm obtained from XPS. For $\alpha = 0.89$, an uncertainty in ρ_δ of 9 orders of magnitude

yielded an uncertainty in δ of only one order of magnitude. In many cases, a tighter bound on the estimated ρ_δ may be possible, as is the case for human stratum corneum presented in a subsequent section.

In contrast to the data presented for aluminum oxide, a capacitive loop is evident in the impedance response for oxides on steel. The zero-frequency impedance was estimated using an extension of the measurement model approach[113] to be $R_\mathrm{f} = 0.756 \pm 0.09$ MΩcm^2. The extrapolation is shown in Figure 9-6(b). The corresponding estimate of film thickness from the Hsu-Mansfeld formula, given as equation (6–42), is $\delta = 0.190$ nm. Extrapolation to zero frequency of the power-law model, also shown in Figure 9-6(b), yields $R_\mathrm{f} = 0.85$ MΩcm^2 and $\delta = 0.187$ nm. The film thickness value obtained from application of the Hsu-Mansfeld formula is substantially smaller than the experimentally measured value of 3 nm. In contrast, application of a power-law distribution of resistivity provides an estimation of film thickness that encompasses the experimentally determined value.

9.2.3 Human Skin (Power Law with Parallel Path)

Impedance data from Membrino[1] are presented in Figure 9-8 for heat-separated excised human stratum corneum immersed in 50 mM buffered $CaCl_2$ electrolyte for 1.9 hours. An analysis based on application of equation (6–42) was presented by Hirschorn *et al.*[111] who, using graphical methods,[87] found that $\alpha = 0.834$ and $Q = 5.36 \times 10^{-8}\ \mathrm{Fcm^{-2}s^{-0.166}}$. They reported that the skin thickness estimated using the capacitance from equation (6–42) and a dielectric constant of 49 was $2.6\ \mu$m, about one order of magnitude smaller than the expected value.

Application of equation (8–29) for estimation of film thickness requires an estimate for ρ_δ. As seen by the straight line in Figure 9-8(c), CPE behavior is evident at the largest measured frequencies. Thus, an upper bound for ρ_δ can be established from the maximum measured frequency of 21 kHz to be $1.7 \times 10^6\ \Omega$cm. The resistivity of body

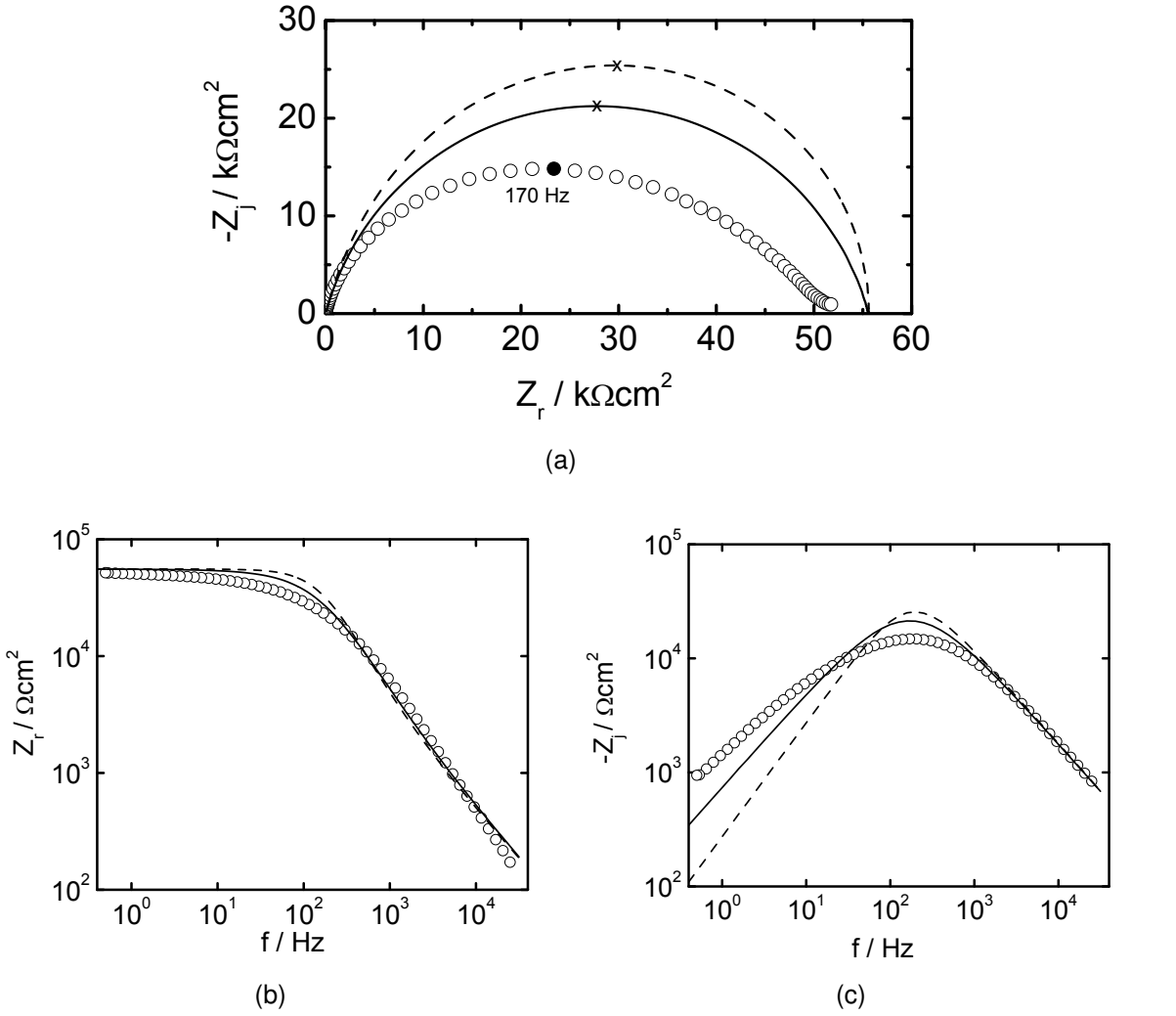

Figure 9-8. The impedance response (symbols) of human stratum corneum immersed in 50 mM buffered $CaCl_2$ electrolyte for 1.9 hours. The solid line is obtained following equation (8–22) with a large value of ρ_0, $\epsilon = 49$, $\gamma = 6.02$, and $\rho_\delta = 48\ \Omega\mathrm{cm}$ and a parallel resistance $R_p = 56\ \mathrm{k}\Omega\mathrm{cm}^2$. The dashed line is obtained using equation (8–22) with $\rho_0 = 2.2 \times 10^8\ \Omega\mathrm{cm}$, $\epsilon = 49$, $\gamma = 6.02$, and $\rho_\delta = 48\ \Omega\mathrm{cm}$: a) Nyquist plot; b) real part of the impedance; and c) imaginary part of the impedance.

fluids is $48\ \Omega$cm. If this value is considered to be a lower bound, the range of possible ρ_δ values is 1.7×10^6 to $48\ \Omega$cm. For $\alpha = 0.834$, $g = 1.04$ from equation (8–28).

The corresponding estimated thickness of skin is between 6 and $31\ \mu$m, in good agreement with the expected value of $10 - 40\ \mu$m. The thickness estimated using equation (9–2) is in better agreement with expected values than are the values obtained by use of equation (6–42). Hirschorn *et al.*[111] explained that the capacitance obtained using equation (6–42) does not account properly for the low resistivity regions of skin that have characteristic frequencies outside the measured frequency range. Equation (6–42) is based on calculation of the characteristic RC time constant and does not take any specific distribution of resistivity or dielectric constant into account. The better agreement obtained using equation (9–2) can be explained by the fact that it is based on formal solution for the impedance associated with a specified resistivity distribution and requires only the high-frequency portion of the measurement.

The power-law impedance model may also be applied to explore the low-frequency impedance response for skin. The low-frequency limit for the impedance response expressed as equation (8–22) is

$$Z_{\mathrm{f}}(0) = g\delta\rho_\delta^{1-\alpha}\rho_0^\alpha \tag{9–7}$$

The function g can be eliminated by introduction of equation (8–29) to yield

$$Z_{\mathrm{f}}(0) = \frac{(\rho_0\epsilon\epsilon_0)^\alpha}{Q} \tag{9–8}$$

The value of $\rho_0 = 2.2 \times 10^8\ \Omega$cm can be obtained from the characteristic frequency $f_0 = 170$ Hz by using the relationship

$$\rho_0 = \frac{1}{2\pi\epsilon\epsilon_0 f_0} \tag{9–9}$$

and the maximum value of the impedance is obtained from equation (9–8) to be $Z_{\mathrm{f}}(0) = 56$ kΩcm^2. Under the assumption that $\rho_\delta = 48\ \Omega$cm (or $\delta = 31\ \mu$m), equation (8–22)

yields the impedance simulation shown as a dashed line in Figure 9-8. As discussed in Chapter 8, the impedance response is asymmetric in a Nyquist plot, yielding CPE behavior at high frequency with $\alpha = 0.834$ and ideal capacitive behavior at low frequency with $\alpha = 1$.

An alternative extension to low frequency is obtained by considering ρ_0 to be infinitely large and including a parallel path for current flow with resistance R_p. The value for R_p was obtained from the characteristic frequency $f_0 = 170$ Hz using

$$R_p = \frac{\delta}{2\pi\epsilon\epsilon_0 f_0} \tag{9–10}$$

where, as was used above, $\delta = 31$ μm. The value of 56 kΩcm^2 obtained for R_p is in good agreement with the value of $Z_{\mathrm{f}}(0)$ obtained for the impedance expressed in terms of ρ_0. The resulting impedance response is shown as a solid line in Figure 9-8. The impedance response in this case is symmetric in a Nyquist plot, yielding CPE behavior with $\alpha = 0.834$ at both high and low frequency. The parallel path for current flow may be considered to arise from transport through skin pores. It is evident that, while the model with a parallel current path shows better agreement with experimental data, neither model accounts fully for the complexity of skin behavior. This lack of agreement, however, does not influence the application of equation (9–2) for assessing skin thickness, since this interpretation requires only the high frequency values.

9.3 Discussion

CPE behavior is commonly seen in the impedance response of electrochemical systems, and the determination of physical properties from interpretation of the impedance response remains a challenging problem. The two prevailing approaches in the literature are those of Brug *et al.*[3] and Hsu and Mansfeld.[6] The Brug formula was developed for surface distributions of capacitance and does not apply to the dielectric response of films. The Hsu-Mansfeld formula was developed for normal distributions, but

Hirschorn *et al.*[111] showed that the film thickness obtained using this formula can be too small.

The Hsu-Mansfeld formula was derived solely on the premise that, independent of the origin of the time-constant distribution, the time constant corresponding to the frequency for which the imaginary part of the impedance has a maximum magnitude can be expressed as $\tau_0 = R_{\mathrm{f}} C_{\mathrm{HM}}$. In contrast, the model development in Chapter 8 identified a specific normal resistivity distribution that exhibits CPE behavior.

The resistivity values at the extremities of the film, ρ_0 and ρ_δ represent key parameters in the power-law model. CPE behavior is seen for frequencies that lie between the corresponding characteristic frequencies f_0 and f_δ. For such data, neither ρ_0 nor ρ_δ can be determined unambiguously. The low-frequency behavior at frequencies below f_0 reflects ideal capacitive behavior for which $\alpha = 1$. The parameter ρ_0 can be determined unambiguously in this case. The high-frequency behavior for frequencies greater than f_δ also reflects ideal capacitive behavior for which $\alpha = 1$. The parameter ρ_δ can be determined unambiguously in this case.

While the power-law impedance may be applied over a complete range of frequency, a consequence of using a specific distribution is that physical properties can be inferred from the high-frequency portion of the spectrum, even for data that show CPE behavior over the entire high-frequency range. Graphical methods detailed by Orazem *et al.*[87] can be used to obtain the CPE parameters Q and α. Often, the dielectric constant is known for specific film compositions. While insertion of Q, α, and ϵ in equation (8–29) provides only the product $\delta \rho_\delta^{1-\alpha}$, this quantity is weakly dependent on ρ_δ for α close to unity. Thus, an estimate for film thickness can be obtained. The examples presented here show that the power-law model for resistivity distribution yields estimated values that are in good agreement with either measured or expected values for film thickness. The examples presented here also show situations for which the

Hsu-Mansfeld formula either cannot be used (aluminum oxide) or yields incorrect values for film thickness (stainless steel and human skin).

The present work should not be considered a substitute for development of system-specific process models. The approach is limited to systems for which the CPE behavior can be attributed to distributions of film properties in the direction normal to the electrode surface. Such systems, however, are commonly encountered. This work may apply to the study of systems that exhibit a distributed dielectric response such as oxides, organic coatings, biological membranes.

9.4 Conclusions

The work presented in Chapter 8 showed that, under assumption that the dielectric constant is independent of position, a normal power-law distribution of local resistivity is consistent with the CPE. An analytic expression was developed, based on the power-law resistivity distribution, that relates CPE parameters to the physical properties of a film. In the present work, this expression yielded physical properties, such as film thickness and resistivity, that were in good agreement with expected or independently measured values for such diverse systems as aluminum oxides, oxides on stainless steel, and human skin.

For the power-law resistivity distribution, CPE behavior was seen for measurements made between the characteristic frequencies f_0 and f_δ. The power-law distribution of local resistivity was shown to yield ideal capacitive behavior at frequencies that are sufficiently large and sufficiently small, as can be expected for any model that accounts for a distributed film resistivity. A symmetric CPE response was obtained by adding a parallel resistive pathway. In Chapter 10, surface distributions of resistance that can account for the CPE are considered.

CHAPTER 10
CPE BEHAVIOR CAUSED BY SURFACE DISTRIBUTIONS OF OHMIC RESISTANCE

A power-law distribution of resistivity in the direction normal to the electrode was shown in Chapter 8 to provide a physical origin of the CPE. The CPE parameters were related directly to physical properties of the system. However, in many cases, the CPE parameters are considered to arise from a distribution of time-constants along the surface of an electrode. Generally, the CPE is considered to arise from a dispersion of capacitance. The approach taken by Brug *et al.* was to assume that the CPE originated from a surface distribution of time constants with uniform Ohmic and charge-transfer resistances.[3] The time-constant dispersion therefore was assumed to originate from a distribution of capacitance. However, the resulting distribution required a range of capacitance over many orders of magnitude that is not considered reasonable for experimental systems.

The resistive properties of a surface may in fact vary significantly due to electrode geometrical effects. Huang *et al.* have shown that pseudo-CPE behavior, where α and Q are frequency dependent, can arise from geometrical effects due to current and potential distributions on ideally polarizable electrode surfaces.[18] The current distributions can be interpreted as a distribution of Ohmic resistance along the surface. However, the current distributions presented by Huang *et al.* are not representative of the CPE due to the frequency dependence of α and Q and the limited range of frequency for which the pseudo-CPE behavior applies.

In the present chapter, surface distributions of resistance with uniform capacitance are derived that result in impedance responses that are consistent with the CPE. The mathematics are developed for a general electrode geometry and then applied specifically for a disk electrode.

10.1 Mathematical Development

A surface distribution of blocking elements with a uniform surface capacitance is shown in Figure 10-1. The general expression for the admittance of a blocking surface

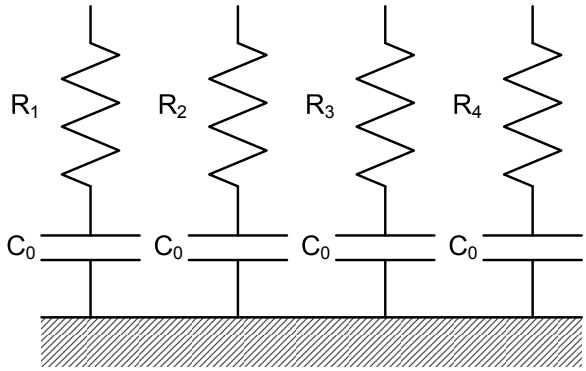

Figure 10-1. A surface distribution of blocking elements with a uniform distribution of local capacitance.

with uniform capacitance over an incremental area is written

$$Y_i(\omega) = \frac{dA}{R(A) + (j\omega C_0)^{-1}} \tag{10–1}$$

where $R(A)$ is a function of area with units of $\Omega\mathrm{cm}^2$ and C_0 is uniform with units of F/cm^2, respectively. Therefore, Y_i has units of Ω^{-1}. The sum of the admittance over the entire surface is expressed by the integral

$$Y_\mathrm{s}(\omega) = \int_0^{A_T} \frac{dA}{R(A) + (j\omega C_0)^{-1}} \tag{10–2}$$

where A_T is the total surface area. The sum Y_s is the unscaled admittance and dividing by the surface area A_T is required to obtained scaled units of admittance. Equation (10–2) can be written in terms of a dimensionless parameter as

$$Y(\omega) = \int_0^1 \frac{d\hat{A}}{R(\hat{A}) + (j\omega C_0)^{-1}} \tag{10–3}$$

where $\hat{A} = A/A_T$ and $Y = Y_\mathrm{s}/A_T$ such that the admittance is scaled. As shown by equation (10–3), as frequency tends toward infinity the observed Ohmic resistance is obtained as

$$Y(\infty) = R_\mathrm{e}^{-1} = \int_0^1 R(\hat{A})^{-1} d\hat{A} \tag{10–4}$$

and as the frequency tends toward zero the capacitance is obtained as

$$\frac{Y(0)}{j\omega} = C_0 \tag{10–5}$$

In Chapter 8, the development of a normal time-constant distribution that is consistent with the CPE was aided by regression of synthetic data to sequential RC elements. For a uniform capacitance it was shown that a power-law distribution of resistance was necessary to achieve the CPE response. The aid of regression was not required for the following development of a surface distribution that is consistent with the CPE.

The impedance response of an individual RC yields an ideal semi-circle when represented in the impedance plane. For a series contribution of individual elements the summation yields the total impedance. The admittance response of an individual blocking element yields an ideal semi-circle when represented in the admittance plane. For a parallel contribution of individual elements the summation yields the total admittance. For these two cases, a similar distribution of time-constants should yield similar responses in the impedance and admittance planes, respectively. Therefore, it is inferred that a power-law distribution of surface resistance will yield a CPE.

A distribution of resistance which provides a bounded value for resistance is proposed to be

$$R = R_s + (R_b - R_s)\hat{A}^\gamma \tag{10–6}$$

where R_b and R_s are boundary values of resistance. Introduction of equation (10–6) into equation (10–3) yields

$$Y(\omega) = \int_0^1 \frac{1}{a(\omega) + b\hat{A}^\gamma} d\hat{A} \tag{10–7}$$

where

$$a(\omega) = R_s + (j\omega C_0)^{-1} \tag{10–8}$$

and

$$b = R_b - R_s \tag{10–9}$$

An analytic solution to equation (10–7) is possible for some integer values of γ. For example, when $\gamma = 3$

$$Y(\omega) = \frac{k}{3a}\left[\frac{1}{2}\log\frac{(k+1)^3}{1+k^3} + \sqrt{3}\arctan\frac{2-k}{k\sqrt{3}} + \frac{\pi\sqrt{3}}{6}\right] \tag{10–10}$$

where $k = (a(\omega)/b)^{1/3}$. Under the condition that $R_b >> R_s$, k is less than 1 for $\omega > (R_b C_0)^{-1}$ and equation (10–10) reduces to

$$Y(\omega) = \frac{2\pi}{3\sqrt{3}} R_b^{-1/3}(R_s + (j\omega C_0)^{-1})^{-2/3} \tag{10–11}$$

The impedance of the system $Z(\omega) = Y(\omega)^{-1}$ is

$$Z(\omega) = \frac{3\sqrt{3}}{2\pi}\frac{R_b^{1/3}}{(R_s + (j\omega C_0)^{-1})^{-2/3}} \tag{10–12}$$

Equation (10–12) is derived for the special case $\gamma = 3$. A general expression of the impedance can be proposed in the same form as

$$Z(\omega) = \frac{1}{g}\frac{R_b^{1/\gamma}}{(R_s + (j\omega C_0)^{-1})^{-\frac{\gamma-1}{\gamma}}} \tag{10–13}$$

where g is a function of γ and, in the case of $\gamma = 3$,$g = \frac{2\pi}{3\sqrt{3}}$. The comparison of equation (10–13) to the numerical integration of equation (10–7) shows that this expression is general and can be applied for all $\gamma > 2$ over broad range of frequencies. Details of the algorithm used for the numerical integration are provided in Appendix C.

The real and imaginary parts of the impedance obtained by numerical integration of equation (10–7) are presented in Figures 10-2(a) and 10-2(b), respectively, with γ as a parameter. The lines represent the evaluation of equation (10–13) where the numerical value of g was obtained at the high-frequency limit of equation (10–13) according to the expression

$$g = \frac{R_b^{1/\gamma} R_s^{\frac{\gamma-1}{\gamma}}}{Z(\infty)} \tag{10–14}$$

and where $Z(\infty)$ is obtained from numerical integration of equation (10–7) at $\omega = \infty$. Equation (10–13) provides good agreement with numerical integration of equation

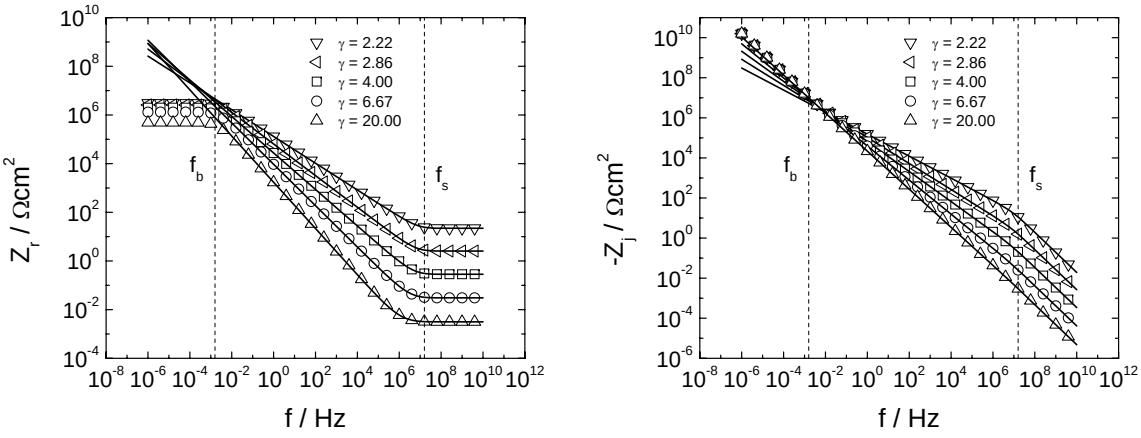

Figure 10-2. A comparison of the impedance response generated by numerical integration of equation (10–7) (symbols) and the analytic expression provided by equation (10–13) (lines) with $R_b = 1 \times 10^7\ \Omega\text{cm}^2$, $R_s = 1 \times 10^{-3}\ \Omega\text{cm}^2$, $C_0 = 10\ \mu F/\text{cm}^2$, and γ as a parameter: a) the real component of impedance; and b) the imaginary component of impedance.

(10–7) for frequencies above a characteristic frequency

$$f_b = \frac{1}{2\pi R_b C_0} \tag{10–15}$$

As shown by Figure 10-3, the value of g is identical to the value of g obtained from the normal power-law distribution presented in Chapter 8, except that in this case g appears in the denominator of the impedance expression.

For frequencies below a characteristic frequency

$$f_s < (2\pi R_s C_0)^{-1} \tag{10–16}$$

equation (10–13) is in the form of the CPE, *i.e.,*

$$Z = \frac{R_b^{1/\gamma}}{g(j\omega C_0)^{\frac{\gamma-1}{\gamma}}} = \frac{1}{(j\omega)^{\alpha} Q} \tag{10–17}$$

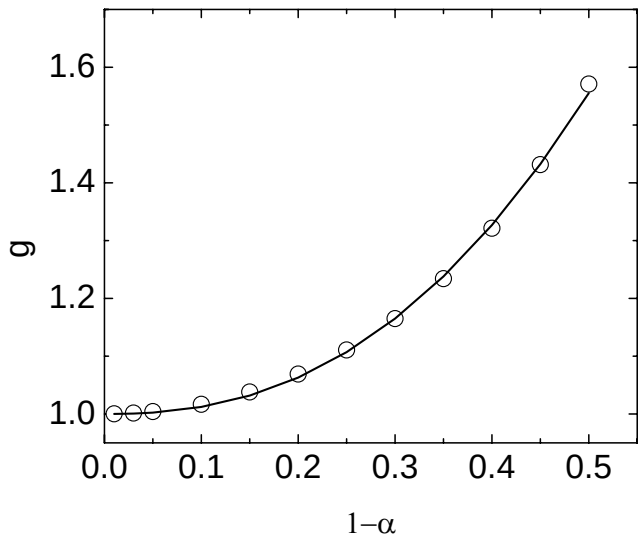

Figure 10-3. The numerical evaluation of g as a function of $1-\alpha$ where the symbols represent the results from equation (10–14). The line represents the interpolation formula given as equation (8–24).

Therefore, equation (10–13) yields the impedance given by equation (1–1) for $(2\pi R_b C_0)^{-1} < f < (2\pi R_s C_0)^{-1}$. Inspection of equation (10–17) suggests that

$$\alpha = \frac{\gamma - 1}{\gamma} \tag{10–18}$$

with

$$Q = \frac{g C_0^{\alpha}}{R_b^{1-\alpha}} \tag{10–19}$$

Thus, equation (10–18) provides the analytic expression for the relationship between α and γ and equation (10–19) provides the analytic expression for the relationship between Q and C_0 and R_b.

As shown in Figure 10-2(a), the Ohmic resistance is obtained at $f > f_s$ which is the frequency range at which equation (10–4) applies. As shown by Figure 10-2(b), the capacitance is obtained at $f < f_b$ which is the frequency range at which equation (10–5) applies. For $(2\pi R_b C_0)^{-1} < f < (2\pi R_s C_0)^{-1}$, only the product given by equation (10–19) is obtainable.

10.2 Disk Electrodes

In the previous section the impedance was derived in terms of a general area A. In the following section the objective is to derive the impedance response in terms of a disk electrode. Two cases are considered. First, the case where the magnitude of the resistance increases with increasing radius; and second, the case where the magnitude of the impedance decreases with increasing radius.

10.2.1 Increase of resistance with increasing radius

For a disk $\hat{A} = r^2/r_0^2$ and equation (10–3) and equation (10–6) yield

$$Y(\omega) = \frac{2}{r_0^2}\int_0^{r_0} \frac{rdr}{R_s + (R_b - R_s)(\frac{r}{r_0})^{2\gamma} + (j\omega C_0)^{-1}} \tag{10–20}$$

As shown in Figure 10-4, a simulated impedance response following equation (10–20) is consistent with the CPE. As shown in Figure 10-4(c), the graphically determined value of α is frequency independent for $f < f_s$. The resistance $R_b = 1 \times 10^{10}\ \Omega\mathrm{cm}^2$ was chosen such that f_b is outside the measurable frequency range. As shown in Figure 10-4(d), a broad distribution of resistance is necessary to achieve the CPE response in the measurable frequency range. For instance, according to equation (10–15), R_b must be greater than $1.59 \times 10^7\ \Omega\mathrm{cm}^2$ for CPE behavior to be evident at 1 mHz when $C_0 = 10\ \mu F/\mathrm{cm}^2$.

10.2.2 Decrease of resistance with increasing radius

Huang *et al.* have derived the current distributions that result from the geometry of an ideally polarizable disk electrode.[18] The current distributions can be interpreted in terms of distribution of local Ohmic resistance. The Ohmic resistance decreased with increasing radius resulting in apparent pseudo-CPE behavior over a small frequency range. The distribution necessary to achieve CPE behavior over a broad frequency range is explored below. Above, a resistance distribution that increases with area was derived that is consistent with the CPE. A numerical method was employed to convert to a resistance distribution that decreases with increasing radius.

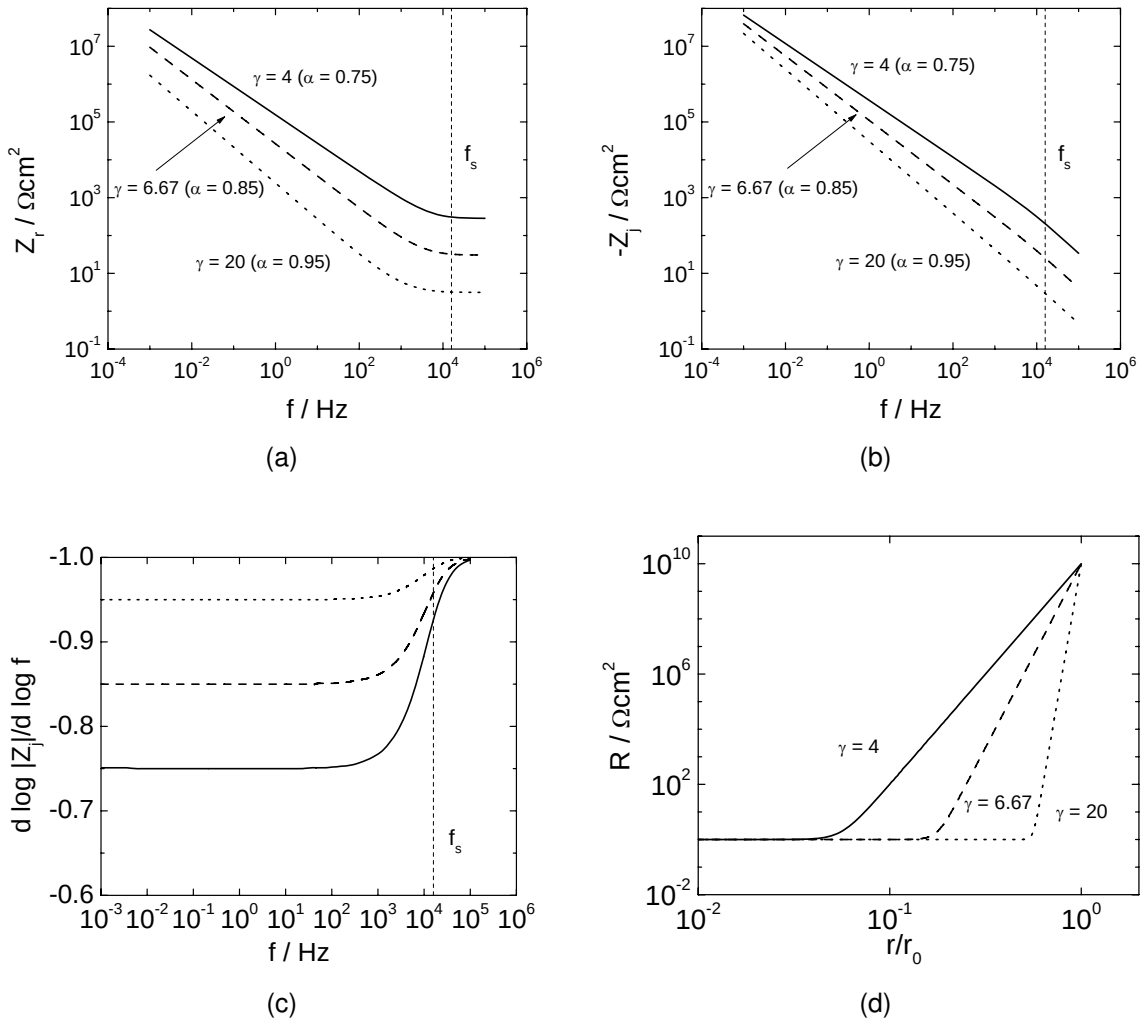

Figure 10-4. The simulation results following equation (10–20) with $R_b = 1 \times 10^{10}\ \Omega\mathrm{cm}^2$, $R_s = 1\ \Omega\mathrm{cm}^2$, $C_0 = 10\ \mu F/\mathrm{cm}^2$, and γ as a parameter: a) the real component of impedance; b) the imaginary component of impedance; c) the graphically determined value of α; and d) the resistivity distributions following equation (10–6).

The numerical method requires dividing the disk into incremental rings. The admittance of the outer incremental area calculated from equation (10–6) is substituted as the value of admittance in the inner incremental area of the disk. This procedure is repeated for every incremental area. Therefore,

$$\hat{A}_{n-k} - \hat{A}_{n-(k+1)} = \pi r_{k+1}^2 - \pi r_k^2 \tag{10–21}$$

and

$$Y_k = \int_{\hat{A}_{n-(k+1)}}^{\hat{A}_{n-k}} \frac{d\hat{A}}{R_s + (R_b - Rs)\hat{A}^{\gamma}} = 2\pi \int_{r_k}^{r_{k+1}} y_k(r) r dr \tag{10–22}$$

where n is the total number of incremental boundaries including the disk center and edge and k represents the individual boundaries. The value of k is an integer that ranges between 0 and $n-1$. A linear approximation is assumed for the admittance between r_k and r_{k+1} as

$$y_k(r) = m_k r + c_k \tag{10–23}$$

where m_k and c_k are constants. The value of c_k is the inner boundary admittance, for instance, $c_0 = R_b^{-1}$. Substitution of equation (10–23) into equation (10–22) yields an expression with a single unknown m_k. The numerical procedure allows for the calculation of an admittance value at every ring boundary k. The corresponding resistance values, *i.e.,* $R_k = y_k(r_k)^{-1}$, yield a distribution that decreases with increasing radius. The numerically determined resistance distribution $R(r)$ can be used to obtain the global admittance of the disk as

$$Y(\omega) = \frac{2}{r_0^2} \int_0^{r_0} \frac{r dr}{R(r) + (j\omega C_0)^{-1}} \tag{10–24}$$

Details of the algorithm is provided in Appendix D.

The simulated results following equation (10–24) are presented in Figure 10-5. The impedance response shown in Figures 10-5(a) and 10-5(b) are identical to Figures 10-4(a) and 10-5(b), respectively. However, in this case, the resistance distribution that accounts for the impedance decreases with increasing radius, as shown in Figure

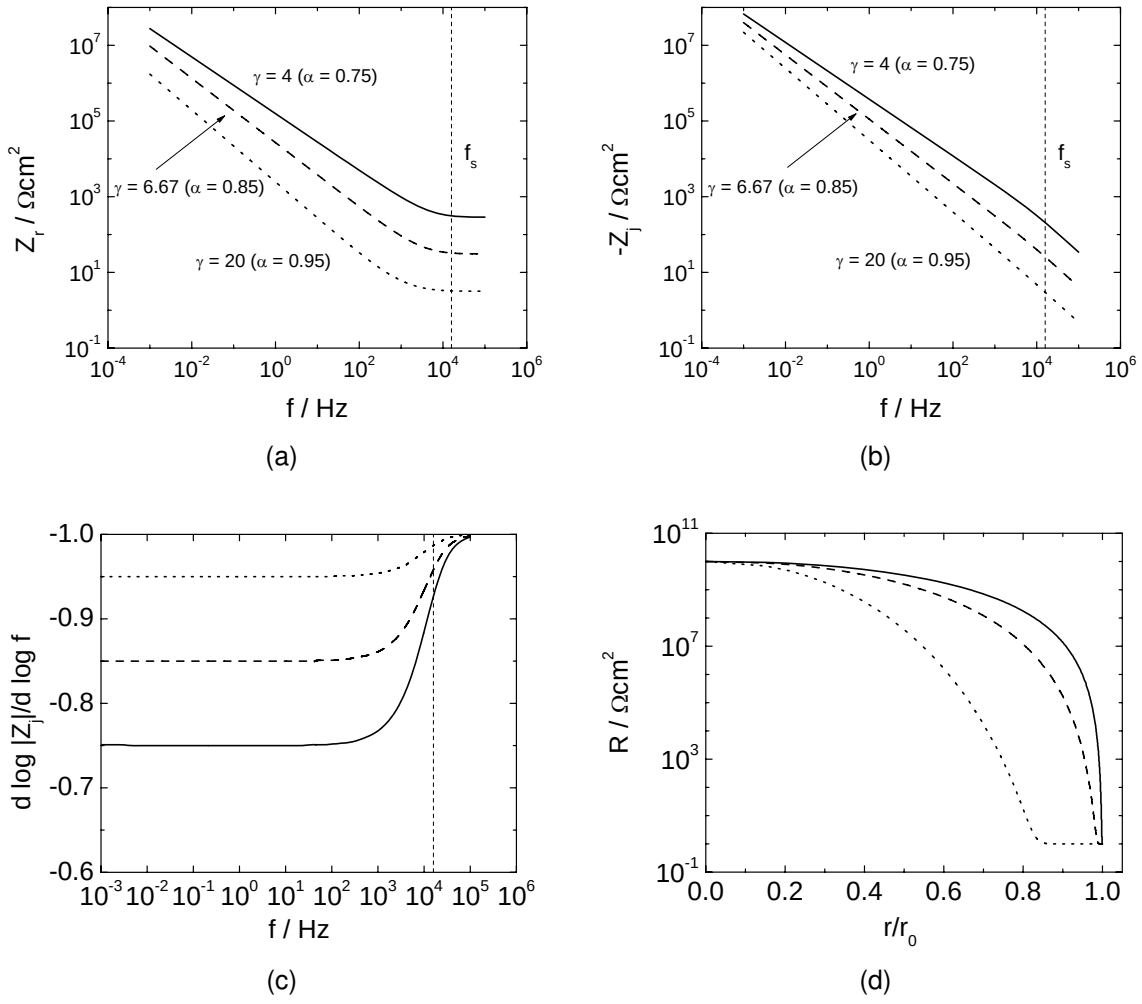

Figure 10-5. The simulation results following equation (10–24) with $R_b = 1 \times 10^{10}\ \Omega\mathrm{cm}^2$, $R_s = 1\ \Omega\mathrm{cm}^2$, $C_0 = 10\ \mu F/\mathrm{cm}^2$, and γ as a parameter: a) the real component of impedance; b) the imaginary component of impedance; c) the graphically determined value of α; and d) the numerically determined resistivity distributions $R(r)$.

10-5(d). The resistance approaches a finite resistance R_s at the outer area of the disk. A broad distribution of Ohmic resistance is necessary to account for the CPE over the frequency range of 1 mHz to 100 kHz.

10.3 Conclusions

The surface distributions of Ohmic resistance necessary to account for CPE behavior were derived for cases where the surface capacitance can assumed to be uniform. A broad distribution is required to account for the CPE over an extended frequency range. The distributions of Ohmic resistance due to geometrical effects of a disk electrode derived by Huang *et al.* are narrow in comparison.[18] For experimental systems, a broad distribution of Ohmic resistance is not expected. Therefore, it is unlikely that the CPE can be attributed to a distribution of Ohmic resistance alone. Nevertheless, the expression for Q given by equation (10–19) is found to be consistent with the general form of capacitance-CPE parameter relations, as is discussed in Chapter 11.

CHAPTER 11
OVERVIEW OF CAPACITANCE-CPE RELATIONS

In Chapter 6, an expression for calculating capacitance from CPE parameters following the work of Brug *et al.*[3] was derived as

$$C_{\mathrm{B}} = Q^{1/\alpha}\left(\frac{R_{\mathrm{e}}R_{\mathrm{t}}}{R_{\mathrm{e}}+R_{\mathrm{t}}}\right)^{(1-\alpha)/\alpha} \tag{11–1}$$

where R_{t} is the charge-transfer resistance, R_{e} is the Ohmic resistance, and Q and α are the CPE parameters. A different expression following the work of Hsu and Mansfeld[6] was derived as

$$C_{\mathrm{HM}} = Q^{1/\alpha}R_{\mathrm{f}}^{(1-\alpha)/\alpha} \tag{11–2}$$

where R_{f} represents the resistance of a film. As discussed earlier, these expressions were derived without consideration of a physical model. In Chapter 9, for a film with a power-law distribution of resistivity and uniform dielectric constant, the capacitance was related to physical properties by equation (9–2). Equation (9–2) can be written

$$C_{\mathrm{eff,f}} = Q^{1/\alpha}R_{\delta}^{(1-\alpha)/\alpha}g^{1/\alpha} \tag{11–3}$$

where $R_{\delta} = \rho_{\delta}\delta$ and g is a function dependent only on α that was expressed by equation (8–28). In Chapter 10, the CPE parameter Q was related to model parameters for a surface distribution of Ohmic resistance by equation (10–19). Equation (10–19) can be written

$$C_0 = Q^{1/\alpha}R_b^{(1-\alpha)/\alpha}g^{-1/\alpha} \tag{11–4}$$

where R_b is the largest value of resistance in the surface distribution of blocking elements.

Equations (11–1)-(11–4) all have the same form, but the resistance values used in the expressions have different meanings. Clearly, consideration of the physical origin of the CPE is required for determining capacitance from impedance spectra. By analog, it

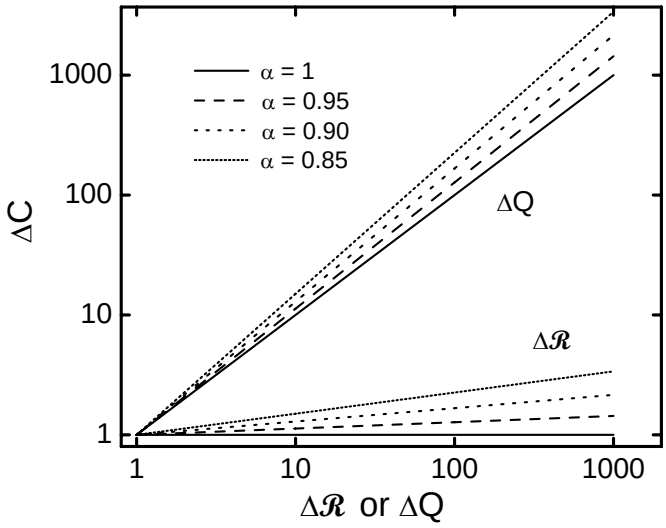

Figure 11-1. Change in capacitance as a function of a change in $\mathcal{R}$ with Q held constant following equation 11–5; and change in capacitance as a function of a change in Q with $\mathcal{R}$ held constant following equation 11–5. Units are arbitrary.

may be reasonable to suspect that the general form of the capacitance-CPE relation is

$$C = Q^{1/\alpha}\mathcal{R}^{(1-\alpha)/\alpha}\mathrm{g}^{1/\alpha} \tag{11–5}$$

where the meaning of $\mathcal{R}$ depends on the system under consideration and g is a system-dependent function that depends only on α. For α values close to unity, the $\mathcal{R}^{(1-\alpha)/\alpha}$ term is insensitive to changes in $\mathcal{R}$. As shown in Figure 11-1, a large change in $\mathcal{R}$ has little effect on the calculated capacitance, whereas, a change in Q has a significant effect on the calculated capacitance. Therefore, for α close to unity, changes in capacitance of a system can be determined approximately from changes of the measured CPE parameters as

$$\Delta C \approx \Delta(Q^{1/\alpha}) \tag{11–6}$$

Equation (11–6) may be useful in assessing changes in active surface area or layer thickness for changing systems. For instance, consider a system where equation (11–3) applies and $\alpha = 0.9$. If a dielectric layer doubles in thickness then R_δ doubles and $C_{\mathrm{eff,f}}$

is halved. Without a priori knowledge of the system, using equation (11–6) will result in an error of less than 8 percent in calculating the change in capacitance. This result is due to the insensitivity of the $R_{\delta}^{(1-\alpha)/\alpha}$ term. A change in system capacitance due to film growth manifests itself primarily in a change in the value of Q.

CHAPTER 12
CONCLUSIONS

The present work showed that the empirical constant-phase element, generally used for data-fitting, can be interpreted in terms of physical properties. Under assumption of a uniform dielectric constant, a normal power-law distribution of local resistivity is consistent with the CPE. Analytic expressions that relate the CPE fitting parameters, α and Q, to physical properties of a film were developed. For such diverse systems as aluminum oxides, oxides on stainless steel, and human skin, these expressions yielded physical properties, such as film thickness and resistivity, that were in good agreement with expected or independently measured values. The power-law impedance model may have extensive utility for characterizing a broad range of systems where a variation in properties is expected in the direction normal to the electrode.

The analytic expression developed in the present work relating CPE parameters to physical properties may also be used to predict dielectric constants of thin films. In the present work, layer thickness was predicted by using literature values of dielectric constant. Conversely, for systems with unknown values of permittivity, the dielectric constant may be calculated from independently measured values of film thickness using the developed model.

In the present work, a power-law distribution of Ohmic resistance along a blocking surface with uniform capacitance was shown to be consistent with the CPE. The broad distribution that is necessary to account for the CPE is not expected experimentally. Therefore, observation of CPE behavior cannot be considered to arise from a distribution of Ohmic resistance alone. Nevertheless, the developed relationship between capacitance and CPE parameters was shown to be in a general form that was consistent with other capacitance-CPE relations. However, the value of resistance that should be used in the relations depends on the source of the CPE. Therefore, consideration of the physical origin of the CPE is required for determining capacitance from impedance spectra.

Interpreting impedance spectra in terms of physical properties requires that experimental and data analysis techniques are properly implemented and fully optimized. In support of the mechanistic development of the CPE, an integrated approach was developed for identifying and minimizing nonlinear distortions in impedance spectra for increased confidence in model development and parameter estimation. A characteristic transition frequency was defined that can be used to tailor a frequency-dependent input signal to optimize signal-to-noise levels while maintaining a linear response. The Kramers-Kronig relations, used for detecting nonlinear responses, are not satisfied for measurements which include the characteristic transition frequency. Therefore, the transition frequency can be used as a tool for both optimizing experimental design and understanding the utility of the Kramers-Kronig relations when verifying impedance data for consistency.

CHAPTER 13
SUGGESTIONS FOR FUTURE WORK

Distributions of physical properties were developed that could account for the CPE behavior observed in the impedance responses of electrochemical systems. The distributions of resistivity and Ohmic resistance, presented in this work, represents only a small portion of the many possible property distributions that may be consistent with the CPE. Possibilities for additional investigation are presented below, including preliminary work for CPE behavior caused by surface distributions of reactivity.

13.1 CPE Behavior Caused by Surface Distributions of Reactivity

Brug *et al.*[3] developed surface distributions of time-constants that accounted for the CPE where capacitance was distributed and Ohmic and kinetic resistances were uniform. In the present work, surface distributions of blocking elements that accounted for the CPE were developed where the Ohmic resistance was distributed and the surface capacitance was uniform. Large distributions of surface capacitance or Ohmic resistance are not expected in real systems. However, for a reactive system a large distribution of kinetic resistances may be reasonable. A distribution of kinetic resistances that can account for the CPE was not considered in the present work. Developing such a distribution would be a significant contribution as it would provide important insight into the active regions of surfaces.

As shown in Chapter 6, in the absence of an Ohmic resistance a distribution of time-constants along a surface reduces to a single effective time-constant. Therefore, the Ohmic resistance must play a role in the observation of the CPE. However, the conditions under which the CPE will be observable for such systems were not examined and the distributions of surface properties necessary to account for the CPE were not developed. Preliminary work is provided here for developing a distribution of reactivity that can account for the appearance of the CPE and for developing the system conditions under which the CPE may be observable.

13.1.1 Mathematical Development

A surface distribution of time-constants is shown in Figure 6-1(a). The general expression for the admittance of a reactive surface over an incremental area can be written

$$Y_i(\omega) = \frac{dA}{R_\mathrm{e}} - \frac{dA}{R_\mathrm{e} + R_\mathrm{e}^2 R_\mathrm{t}^{-1} + j\omega R_\mathrm{e}^2 C_0} \tag{13–1}$$

where $R_\mathrm{t}(A)$ is a function of position with units of $\Omega\mathrm{cm}^2$, and R_e and C_0 are uniform with units of $\Omega\mathrm{cm}^2$ and F/cm^2, respectively. The sum of the admittance over the entire surface is expressed by the integral

$$Y_\mathrm{s}(\omega) = \int_0^{A_T} \frac{dA}{R_\mathrm{e}} - \int_0^{A_T} \frac{dA}{R_\mathrm{e} + R_\mathrm{e}^2 R_\mathrm{t}^{-1} + j\omega R_\mathrm{e}^2 C_0} \tag{13–2}$$

where A_T is the total surface area. The sum Y_s is the unscaled admittance and dividing by the surface area A_T is required to obtain scaled units of admittance. Equation (13–2) can be written in terms of a dimensionless parameter as

$$Y(\omega) = \int_0^1 \frac{d\hat{A}}{R_\mathrm{e}} - \int_0^1 \frac{d\hat{A}}{R_\mathrm{e} + R_\mathrm{e}^2 R_\mathrm{t}^{-1} + j\omega R_\mathrm{e}^2 C_0} \tag{13–3}$$

where $\hat{A} = A/A_T$ and $Y = Y_\mathrm{s}/A_T$ such that the admittance is scaled. A distribution of resistance is proposed to be

$$R_\mathrm{t} = R_\mathrm{t,m} \hat{A}^{-\gamma} \tag{13–4}$$

where $R_\mathrm{t,m}$ represents the minimum value of charge-transfer resistance along the surface. Equation (13–4) is unbounded because it is envisioned that there could be portions of the surface that are inactive and therefore have an infinite charge-transfer resistance. Introduction of equation (13–4) into equation (13–3) yields

$$Y(\omega) = \frac{1}{R_\mathrm{e}} - \int_0^1 \frac{1}{a(\omega) + b\hat{A}^\gamma} d\hat{A} \tag{13–5}$$

where

$$a(\omega) = R_\mathrm{e} + j\omega R_\mathrm{e}^2 C_0 \tag{13–6}$$

and

$$b = \frac{R_{\mathrm{e}}^2}{R_{\mathrm{t,m}}} \tag{13–7}$$

An analytic solution to equation (13–5) is possible for some integer values of γ. For example, when $\gamma = 3$

$$Y(\omega) = \frac{1}{R_{\mathrm{e}}} - \frac{k}{3a}\left[\frac{1}{2}\log\frac{(k+1)^3}{1+k^3} + \sqrt{3}\arctan\frac{2-k}{k\sqrt{3}} + \frac{\pi\sqrt{3}}{6}\right] \tag{13–8}$$

where $k = (a(\omega)/b)^{1/3}$. Under the condition that $R_{\mathrm{t,m}}/R_{\mathrm{e}}$ is small, k is less than 1 for $\omega < (R_{\mathrm{t,m}}C_0)^{-1}$ and equation (13–8) reduces to

$$Y(\omega) = \frac{1}{R_{\mathrm{e}}} - \frac{2\pi}{3\sqrt{3}b^{1/3}a(\omega)^{2/3}} = \frac{1}{R_{\mathrm{e}}} - \frac{2\pi}{3\sqrt{3}}(R_{\mathrm{e}}^2/R_{\mathrm{t,m}})^{-1/3}R_{\mathrm{e}}^{-2/3}(1+j\omega R_{\mathrm{e}}C_0)^{-2/3} \tag{13–9}$$

For frequencies $\omega > (R_{\mathrm{e}}C_0)^{-1}$, the impedance of the system $Z(\omega) = Y(\omega)^{-1}$ is

$$Z(\omega) = \frac{1}{\frac{1}{R_{\mathrm{e}}} - \frac{1}{T(j\omega)^{2/3}}} \tag{13–10}$$

where $T = \frac{3\sqrt{3}R_{\mathrm{e}}^2C_0^{2/3}}{2\pi R_{\mathrm{t,m}}^{1/3}}$. Equation (13–10) can be written

$$Z(\omega) = \frac{1}{c - jd} \tag{13–11}$$

where $c = \frac{1}{R_{\mathrm{e}}} - \frac{\omega^{-2/3}}{T}\cos(-\frac{2}{3}\frac{\pi}{2})$ and $d = \frac{\omega^{-2/3}}{T}\sin(-\frac{2}{3}\frac{\pi}{2})$. Multiplication of equation (13–11) by its complex conjugate yields

$$Z(\omega) = \frac{1}{R_{\mathrm{e}}D} - \frac{\omega^{-2/3}}{TD}\cos(-\frac{2}{3}\frac{\pi}{2}) + j\frac{\omega^{-2/3}}{TD}\sin(-\frac{2}{3}\frac{\pi}{2}) \tag{13–12}$$

where

$$D = \frac{1}{R_{\mathrm{e}}^2} - \frac{2\omega^{-2/3}}{R_{\mathrm{e}}T}\cos(-\frac{2}{3}\frac{\pi}{2}) + \frac{\omega^{-4/3}}{T^2} \tag{13–13}$$

For large frequencies, *i.e.,* in the range $\omega > (R_{\mathrm{e}}C_0)^{-1}$, the second and third terms in equation (13–13) are negligible and the imaginary component of equation (13–12) reduces to

$$Z_j(\omega) = \frac{\omega^{-2/3}}{Q_s}\sin(-\frac{2}{3}\frac{\pi}{2}) \tag{13–14}$$

where $Q_s = \frac{3\sqrt{3}C_0^{2/3}}{2\pi R_{\mathrm{t,m}}^{1/3}}$. Equation (13–14) is in the form of the imaginary component of the CPE with $\alpha = 2/3$. The real component of equation (13–12) does not appear to be in the same form as the real component of the CPE. However, the CPE is consistent with the Kramers-Kronig relations, therefore, the fact that $Z_j = Z_{j,\mathrm{CPE}}$ requires that $Z_r = Z_{r,\mathrm{CPE}}$.

Equation (13–10) is derived for the special case $\gamma = 3$. A general expression of the impedance, in the frequency range $(2\pi R_{\mathrm{e}}C_0)^{-1} < f < (2\pi R_{\mathrm{t,m}}C_0)^{-1}$, can be proposed in the same form as

$$Z(\omega) - R_{\mathrm{e}} = \frac{1}{(j\omega)^{\alpha}Q} \tag{13–15}$$

with

$$\alpha = \frac{\gamma - 1}{\gamma} \tag{13–16}$$

and

$$Q = \frac{C_0^{\alpha}}{gR_{\mathrm{t,m}}^{1-\alpha}} \tag{13–17}$$

where g is a function of γ and, in the case of $\gamma = 3$, $g = \frac{2\pi}{3\sqrt{3}}$. An interpolation formula

$$g = 1 + 2.88\gamma^{-2.375} \tag{13–18}$$

could be obtained that adequately represents the function in the range $0 \leq 1/\gamma \leq 0.5$. A comparison of the impedance response generated by numerical integration of equation (13–5) and the analytical expression provided by equation (13–15) is provided in Figure 13-1.

13.1.2 Interpretation

As shown in Chapter 6, the presence of an Ohmic resistance is required to observe CPE behavior caused by a distribution of properties along an electrode. A power-law distribution of charge-transfer resistance is consistent with the CPE only for frequencies greater than

$$f_{R_{\mathrm{e}}C_0} = (2\pi R_{\mathrm{e}}C_0)^{-1} \tag{13–19}$$

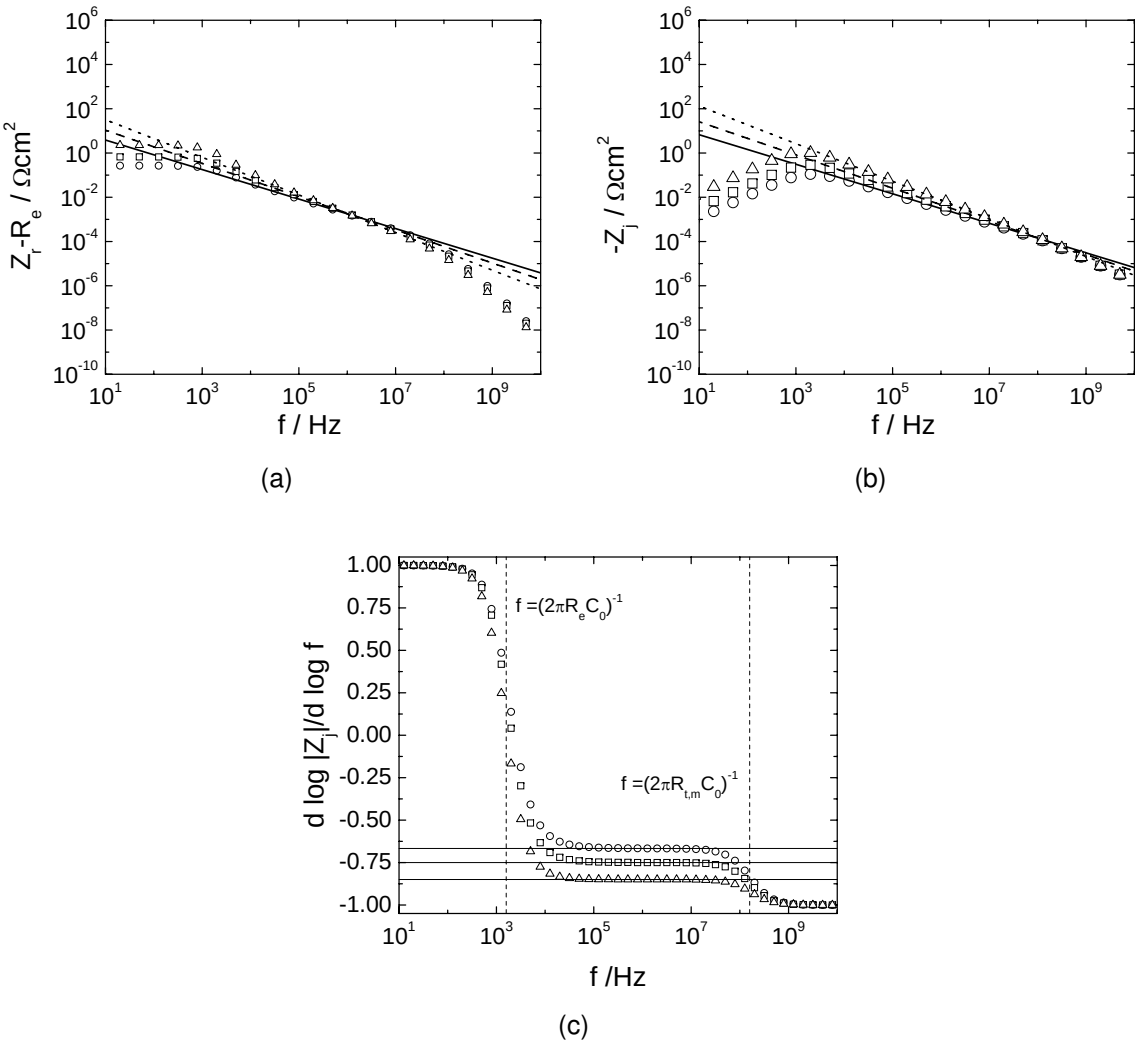

Figure 13-1. A comparison of the impedance response generated by numerical integration of equation (13–5) (symbols) and the analytical expression provided by equation (13–15) (lines) with $R_{\mathrm{t,m}} = 1 \times 10^{-4}\ \Omega\mathrm{cm}^2$, $C_0 = 10\ \mu F/\mathrm{cm}^2$, $R_{\mathrm{e}} = 10\ \Omega\mathrm{cm}^2$, and γ as a parameter: a) the real component of impedance; b) the imaginary component of impedance; and c) the graphically determined value of α. The symbols represent calculations performed for $\bigcirc\ \gamma = 3$, $\square\ \gamma = 4$, and $\triangle\ \gamma = 6.67$.

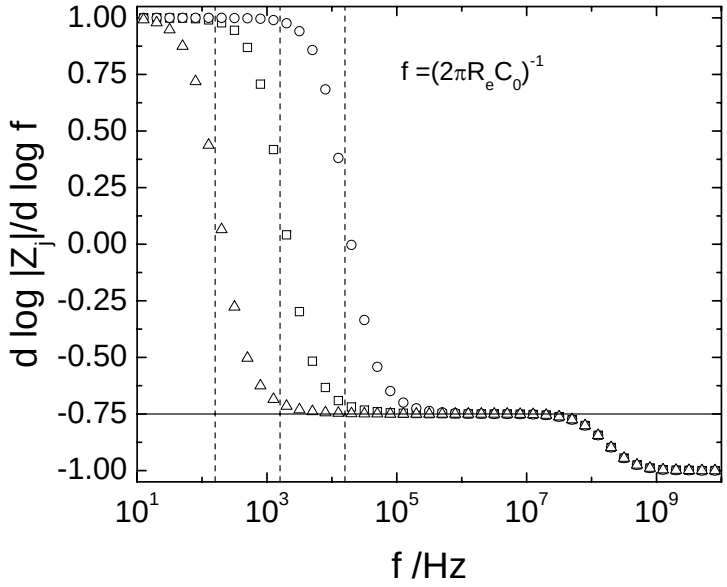

Figure 13-2. The graphically determined value of α for an impedance response generated by numerical integration of equation (13–5) with $R_{\mathrm{t,m}} = 1 \times 10^{-4}\ \Omega\mathrm{cm}^2$, $C_0 = 10\ \mu F/\mathrm{cm}^2$, $\gamma = 4$, and R_{e} as a parameter. The symbols represent calculations performed for ◯ $R_{\mathrm{e}} = 1\ \Omega\mathrm{cm}^2$, □ $R_{\mathrm{e}} = 10\ \Omega\mathrm{cm}^2$, △ $R_{\mathrm{e}} = 100\ \Omega\mathrm{cm}^2$.

The effect of Ohmic resistance on the frequency range where the CPE is observable is shown in Figure 13-2. As shown in Figure 13-2, the CPE becomes observable at approximately one frequency decade greater than $f_{R_{\mathrm{e}}C_0}$. Single time-constant behavior is observed at frequencies less than $f_{R_{\mathrm{e}}C_0}$.

Typically, the experimentally assessable frequency range is less than 100 kHz. Therefore, $f_{R_{\mathrm{e}}C_0}$ must have a value of less than 10 kHz for CPE caused by a distribution of reactivity to be observable in the assessable frequency range. For a typical value of the double layer, *i.e.,* $C_0 = 10\ \mu F/\mathrm{cm}^2$, the Ohmic resistance of the system must be at least $R_{\mathrm{e}} = 1.6\ \Omega\mathrm{cm}^2$ to observe the CPE. Observation of the CPE at frequencies less than $f_{R_{\mathrm{e}}C_0}$ must be attributed to a physical source other than a distribution of reactivity. One such source is a distribution of resistivity within a film provided in Chapter 8.

13.2 CPE Behavior Caused by Normal Distributions of Properties

In the present work, a power-law distribution of local resistivity within a film was shown to be consistent with the CPE under the condition that the dielectric constant is independent of position. However, for an inhomogeneous layer, it may also be expected that the dielectric constant varies with position. For instance, for human skin, it may be expected that that the outer fatty layer has a dielectric constant consistent with lipids, *i.e.,* $\epsilon \approx 2$, and the layer adjacent to body fluids has a dielectric constant consistent with saline solution, *i.e.,* $\epsilon \approx 50$. A non-uniform distribution of dielectric constant will cause the resistivity distribution necessary to account for the CPE to differ from that of the power-law. A non-uniform dielectric constant was not considered in the present work and the influence of a specified distribution of permittivity on the interpretation of the CPE offers an area for additional investigation.

APPENDIX A
PROGRAM CODE FOR LARGE AMPLITUDE PERTURBATIONS

The MATLAB algorithm used for the numerical solution of the nonlinear circuit models discussed in Section 3.2 is presented below.

```
function large perturbation
ZR=0;
ZJ=0;
wM=0;
Vamp=0;
Rtmean=0;
for x=-1:.2:5
deltaU=.1; [input potential amplitude: V]
Cd=100e-6;[capacitance: F/cm^2]
Re=1; [Ohmic resistance: Ωcm^2]
ba=19; [anodic coefficient: V^-1]
bc=19; [cathodic coefficient: V^-1]
Vbar=0; [steady-state interfacial potential: V]
io=1e-3; [exchange current density: A/cm^2]
w = 10^x;
f=w/2/pi; [frequency: Hz]
cyclet=1/f;
scale=2000;
unittime=cyclet/scale;
segfac=1;
numdatapercycle=cyclet/unittime;
Rt1=1/(io*(ba*exp(ba*Vbar)+bc*exp(-bc*Vbar)));
t=[0:unittime:segfac*unittime]'; [time: s]
Rt1final=1/(io*(ba*exp(ba*Vbar)+bc*exp(-bc*Vbar)));
```

```
ifardifffinal=2;
while abs(ifardifffinal)¿1e-14
Afinal = deltaU * (Rt1final + Re)/
(Rt1final * (Cd * Re)^2) * (1/(((Rt1final + Re)^2/(Rt1final * Cd * Re)^2) + w^2));
Vfinal=Afinal*(sin(w*t)+(w*Cd*Re*Rt1final/(Rt1final+Re))*cos(w*t));
ifar1final=Vfinal/Rt1final;
Vfinal=Vfinal(1,1);
ifar1final=ifar1final(1,1);
ifarexpfinal=io*(exp(ba*Vfinal)-exp(-bc*Vfinal));
Rt2final=Vfinal/ifarexpfinal;
Rt1final=Rt2final;
ifardifffinal=ifar1final-ifarexpfinal;
end
tfinal=0;
factor=round(numdatapercycle/segfac);
for loop1=1:2*factor
ifardiff=2;
while abs(ifardiff)¿1e-14
A = deltaU * (Rt1 + Re)/(Rt1 * (Cd * Re)^2) * (1/(((Rt1 + Re)^2/(Rt1 * Cd * Re)^2) + w^2));
V=A*(sin(w*t)+(w*Cd*Re*Rt1/(Rt1+Re))*cos(w*t));
ifar1=V/Rt1;
V=V(length(V),1);
ifar1=ifar1(length(ifar1),1);
ifarexp=io*(exp(ba*V)-exp(-bc*V));
Rt2=V/ifarexp;
Rt1=Rt2;
ifardiff=ifar1-ifarexp;
```

```
end
t(1,:)=[];
tfinal=[tfinal;t];
tnext=[t(length(t),1):unittime:t(length(t),1)+segfac*unittime]';
Vbar=V(length(V),1);
Rt1=1/(io*(ba*exp(ba*Vbar)+bc*exp(-bc*Vbar)));
t=tnext;
Vnext=V;
Vfinal=[Vfinal;Vnext];
ifar1next=ifar1;
ifarexpnext=ifarexp;
ifar1final=[ifar1final;ifar1next];
ifarexpfinal=[ifarexpfinal;ifarexpnext];
end
assignin('base','tfinal',tfinal)
Rtmatrix=Vfinal./ifar1final;
assignin('base','Rtmatrix',Rtmatrix)
RtM=mean(Rtmatrix);
Rtmean=[Rtmean;RtM];
V=deltaU*sin(w*tfinal);
ic=(V-Vfinal-ifar1final*Re)/Re;
iT=ifar1final+ic;
ifarcheck=io*(exp(ba*Vfinal)-exp(-bc*Vfinal));
assignin('base','iT',iT)
assignin('base','V',V)
iTmax=max(iT);
Vmax=max(V);
```

```
LissM=[iT/iTmax,V/Vmax];
assignin('base','LissM',LissM)
MiT=[tfinal,iT];
length(MiT);
l=round(numdatapercycle);
go=20;
MV=[tfinal,V];
[CV1, IV1] = max(MV(1 : round(numdatapercycle), 2));
[CV2, IV2] = max(MV(IV1 + go : 2 * round(numdatapercycle), 2));
index11=IV1;
index22=IV1+IV2+go-1;
sine=sin(w*tfinal);
cose=cos(w*tfinal);
integrandVr=V(index11:index22).*sine(index11:index22);
integrandVj=V(index11:index22).*cose(index11:index22);
integrandIr=iT(index11:index22).*sine(index11:index22);
integrandIj=iT(index11:index22).*cose(index11:index22);
AVr=cumtrapz(tfinal(index11:index22),integrandVr);
Vr=AVr(length(AVr));
AVj=cumtrapz(tfinal(index11:index22),integrandVj);
Vj=AVj(length(AVj));
AIr=cumtrapz(tfinal(index11:index22),integrandIr);
Ir=AIr(length(AIr));
AIj=cumtrapz(tfinal(index11:index22),integrandIj);
Ij=AIj(length(AIj));
assignin('base','Ij',Ij);
assignin('base','Ir',Ir);
```

```
j=sqrt(-1);
Zr=real((Vr+j*Vj)/(Ir+j*Ij));
Zj=imag((Vr+j*Vj)/(Ir+j*Ij));
ZR=[ZR;Zr]; [impedance: Ωcm^2]
ZJ=[ZJ;Zj]; [impedance: Ωcm^2]
wM=[wM;w];
Vmax=max(Vfinal);
Vamp=[Vamp;Vmax];
end
Vamp(1,:)=[];
ZR(1,:)=[];
ZJ(1,:)=[];
wM(1,:)=[];
Rtmean(1,:)=[]
w=wM;
fdet=w/2/pi;
assignin('base','w',w)
assignin('base','ZR',ZR);
assignin('base','ZJ',ZJ);
assignin('base','fdet',fdet)
assignin('base','Vamp',Vamp)
assignin('base','Rtmean',Rtmean)
figure;plot(ZR,ZJ,'o');axis equal;
figure;loglog(fdet,ZJ,'o');
figure;loglog(fdet,ZR,'o');
end
```

APPENDIX B
PROGRAM CODE FOR NORMAL DISTRIBUTIONS

The MATLAB code used for simulating the impedance resulting from a normal power-law distribution of resistivity as discussed in Chapter 8 is presented below. The program numerically integrates equation (8–17) and compares the result with equation (8–22).

```
function powerlaw
e=10; [dielectric constant]
e0=8.8542e-14; [permittivity of vacuum: F/cm]
delta=100e-7; [film thickness: cm]
alphai=0.667; [CPE parameter]
gamma=1/(1-alphai); [power-law exponent]
rhodelta=1e5; [interfacial resistivity: Ωcm]
rho0=1e18; [interfacial resistivity: Ωcm]
start=1e-12;
finish=1;
startlog10=log10(start);
finishlog10=log10(finish);
inc=.025;
dlog10=[startlog10:inc:finishlog10]';
xxN = 10.^dlog10;[normalized position: cm]
xx=xxN*delta;[position: cm]
res = rhodelta * xxN.^-gamma;
resMMM=res/rhodelta;
res=1./(1/rho0+(1/rhodelta-1/rho0)*1./resMMM);[resistivity: Ωcm]
fdet=0;
ZM=0;
for x=-3:.1:5
```

$\mathrm{f} = 10^{\mathrm{x}}$; [frequency: Hz]

w=2*pi*f;

integrand=1./((1./res)+j*w*e*e0);

AT=cumtrapz(xx,integrand);

Aint=AT(length(AT));

Zi=Aint;

ZM=[ZM;Zi];

fdet=[fdet;f];

end

fdet(1,:)=[];

ZM(1,:)=[];[impedance: $\Omega\mathrm{cm}^2$]

wdet=2*pi*fdet;

Zr=real(ZM);

Zj=imag(ZM);

alphaM=0;

QM=0;

for x=1:1:length(fdet)-1

alpha1=(log10(-Zj(x+1,1))-log10(-Zj(x,1)))/(log10(fdet(x+1,1))-log10(fdet(x,1)));

alphaM=[alphaM;alpha1];

$\mathrm{Q1} = \mathrm{wdet}(\mathrm{x}, 1)^{\mathrm{alpha1}}/\mathrm{Zj}(\mathrm{x}, 1) * \sin(\mathrm{alpha1} * \mathrm{pi}/2)$;

QM=[QM;Q1];

end

$\mathrm{g} = 1 + 2.88261 * (1 - \mathrm{alphai})^{2.37476}$;

$\mathrm{Zcalc} = \mathrm{g} * \mathrm{delta} * \mathrm{rhodelta}^{(1/\mathrm{gamma})}./(\mathrm{rho0}^{-1} + \mathrm{j} * \mathrm{wdet} * \mathrm{e} * \mathrm{e0}).^{((\mathrm{gamma}-1)/\mathrm{gamma})}$;

Zcalcr=real(Zcalc);

Zcalcj=imag(Zcalc);

figure;semilogx(fdet,alphaM,'o')

```
figure;semilogx(fdet,QM,'o')
figure;plot(Zr,-Zj,'o',Zcalcr,-Zcalcj);axis equal
figure;loglog(fdet,Zr,'o',fdet,Zcalcr)
figure;loglog(fdet,-Zj,'o',fdet,-Zcalcj)
figure;loglog(xx,res,'o')
end
```

APPENDIX C
PROGRAM CODE FOR SURFACE DISTRIBUTIONS

The MATLAB code used for simulating the impedance resulting from a surface distribution of Ohmic resistance as discussed in Section 10.1 is presented below. The program numerically integrates equation (10–7).

function surface distribution general area Rb=1e7;[boundary resistance: [$\Omega\mathrm{cm}^2$]

Rs=1e-3;[boundary resistance: [$\Omega\mathrm{cm}^2$]

alpha=0.85;[CPE parameter]

gamma=1/(1-alpha); [power-law exponent]

C0=10e-6; [surface capacitance: F/cm^2]

inc=.01;

start=-7;

logA=[start:inc:0]';

$\mathrm{A} = 10.^{\mathrm{l}}\mathrm{ogA}$;

Ahat=[0;A]; [normalized area: cm^2]

$\mathrm{R} = \mathrm{Rs} + (\mathrm{Rb} - \mathrm{Rs}) * \mathrm{Ahat}.^{\mathrm{g}}\mathrm{amma}$; [local resistance: $\Omega\mathrm{cm}^2$]

fdet=0;

YM=0;

for x=-3:.1:8

$\mathrm{f} = 10^{\mathrm{x}}$;[frequency: Hz]

w=2*pi*f;

$\mathrm{integrand} = 1./(\mathrm{R} + (\mathrm{j} * \mathrm{w} * \mathrm{C0})^{-}1)$;

AT=cumtrapz(Ahat,integrand);

Aint=AT(length(AT));

Yi=Aint;

YM=[YM;Yi];

fdet=[fdet;f];

end

```
fdet(1,:)=[];
YM(1,:)=[];
wdet=2*pi*fdet;
ZM=1./YM;[impedance:Ωcm^2]
Zr=real(ZM);
Zj=imag(ZM);
alphaM=0;
QM=0;
for x=1:1:length(fdet)-1
alpha1=(log10(-Zj(x+1,1))-log10(-Zj(x,1)))/(log10(fdet(x+1,1))-log10(fdet(x,1)));
alphaM=[alphaM;alpha1];
Q1 = wdet(x, 1)^alpha1/Zj(x, 1) * sin(alpha1 * pi/2);
QM=[QM;Q1];
end
figure;semilogx(fdet,alphaM,'o')
figure;loglog(Ahat,R,'o')
fb=1/(2*pi*Rb*C0);
fs=1/(2*pi*Rs*C0);
gs = Zr(length(Zr), 1)/(Rb^(1/gamma) * Rs^(gamma - 1)/gamma));
Zmod = gs * Rb^(1/gamma)./(Rs + (j * wdet * C0).^-1).^( - (gamma - 1)/gamma);
Zmodr=real(Zmod);
Zmodj=imag(Zmod);
figure;loglog(fdet,Zr,'o',fdet,Zmodr);
figure;loglog(fdet,-Zj,'o',fdet,-Zmodj);
g=1/gs;
2*pi/3/sqrt(3);
end
```

APPENDIX D
PROGRAM CODE FOR DISK ELECTRODE DISTRIBUTION

The MATLAB code used for the numerical method outlined in Section 10.2.2 is presented below.

function disk distribution Rb=1e10;[$\Omega\mathrm{cm}^2$]

Rs=1e0;[$\Omega\mathrm{cm}^2$]

alpha=0.85;[CPE parameter]

gamma=1/(1-alpha);[power-law exponent]

C0=10e-6;[surface capacitance: F/cm^2]

inc=.01;

start=-3;

logA=[start:inc:0]';

$\mathrm{A} = 10.^{\mathrm{l}}\mathrm{ogA}$;

Ahat=[0;A]; [normalized area: cm^2]

$\mathrm{R} = \mathrm{Rs} + (\mathrm{Rb} - \mathrm{Rs}) * \mathrm{Ahat}.^{\mathrm{g}}\mathrm{amma}$; [local resistance: $\Omega\mathrm{cm}^2$]

figure;loglog(Ahat,R,'o')

integrand=1./R;

YM=cumtrapz(Ahat,integrand);

integrandA=ones(length(Ahat),1);

AM=cumtrapz(Ahat,integrandA);

YunitM=0;

AunitM=0;

for x=1:1:length(YM)-1

Yunit=YM(x+1,1)-YM(x,1);

YunitM=[YunitM;Yunit];

A=AM(x+1,1)-AM(x,1);

AunitM=[AunitM;A];

end

YunitM(1,:)=[];

AunitM(1,:)=[];

sum(AunitM)

sum(YunitM)

M=[AunitM,YunitM];

Aunitflip=flipud(AunitM);

Yunitflip=flipud(YunitM);

r=0;

rnext=0;

for x=1:1:length(Aunitflip)

$\mathrm{rnext} = \mathrm{sqrt}((\mathrm{Aunitflip}(\mathrm{x}, 1) + \mathrm{pi} * \mathrm{rnext}^2)/\mathrm{pi})$;

r=[r;rnext];

end

r; [radius: cm]

length(r);

length(Yunitflip);

Yb=1/Rb;

bnext=Yb;

YMM=Yb;

for x=1:1:length(Yunitflip)

b=bnext;

YT=Yunitflip(x,1);

ri=r(x,1);

rf=r(x+1,1);

$\mathrm{m} = (\mathrm{YT} - \mathrm{pi} * \mathrm{b} * (\mathrm{rf}^2 - \mathrm{ri}^2))/(2/3 * \mathrm{pi} * (\mathrm{rf}^3 - \mathrm{ri}^3))$;

Yf=m*rf+b;

bnext=Yf;

YMM=[YMM;Yf];

end

RM=1./YMM;

L=[r,RM];

figure;semilogy(r,RM,'o')

r0=r(length(r),1);

$\mathrm{Ahat2} = \mathrm{r.}^2/\mathrm{r0}^2$;

trapz(Ahat,YM)

trapz(Ahat2,YMM)

R=RM;

fdet=0;

YM=0;

for x=-3:.1:5

$\mathrm{f} = 10^{\mathrm{x}}$; [frequency: Hz]

w=2*pi*f;

$\mathrm{integrand} = \mathrm{r.}/(\mathrm{R} + (\mathrm{j} * \mathrm{w} * \mathrm{C0})^{-}1)$

AT=cumtrapz(r,integrand);

Aint=AT(length(AT));

Yi=Aint;

YM=[YM;Yi];

fdet=[fdet;f];

end

fdet(1,:)=[];

YM(1,:)=[];

wdet=2*pi*fdet;

$\mathrm{YM} = \mathrm{YM} * 2/\mathrm{r0}^2$;

ZM=1./YM; [impedance: $\Omega\mathrm{cm}^2$]

```
Zr=real(ZM);
Zj=imag(ZM);
alphaM=0;
QM=0;
for x=1:1:length(fdet)-1
alpha1=(log10(-Zj(x+1,1))-log10(-Zj(x,1)))/(log10(fdet(x+1,1))-log10(fdet(x,1)));
alphaM=[alphaM;alpha1];
Q1 = wdet(x, 1)^alpha1/Zj(x, 1) * sin(alpha1 * pi/2);
QM=[QM;Q1];
end
rhat=r/r0;
figure;semilogx(fdet,alphaM,'o')
figure;semilogy(r,R,'o')
figure;loglog(fdet,Zr,'o');
figure;loglog(fdet,-Zj,'o');
end
```

REFERENCES

[1] M. A. Membrino, Transdermal delivery of therapeutic drugs by iontophoresis, Ph.D. thesis, University of Florida, Gainesville, FL (December 2001).

[2] V. M.-W. Huang, V. Vivier, M. E. Orazem, N. Pébère, B. Tribollet, The apparent CPE behavior of a disk electrode with faradaic reactions, J. Electrochem. Soc. 154 (2007) C99–C107.

[3] G. J. Brug, A. L. G. van den Eeden, M. Sluyters-Rehbach, J. H. Sluyters, The analysis of electrode impedances complicated by the presence of a constant phase element, J. Electroanal. Chem. 176 (1984) 275–295.

[4] S. Cattarin, M. Musiani, B. Tribollet, Nb electrodissolution in acid fluoride medium, J. Electrochem. Soc. 149 (10) (2002) B457–B464.

[5] J.-B. Jorcin, M. E. Orazem, N. Pébère, B. Tribollet, Cpe analysis by local electrochemical impedance spectroscopy, Electrochim. Acta 51 (2006) 1473–1479.

[6] C. H. Hsu, F. Mansfeld, Technical note: Concerning the conversion of the constant phase element parameter Y_0 into a capacitance, Corros. 57 (2001) 747–748.

[7] M. E. Orazem, B. Tribollet, Electrochemical Impedance Spectroscopy, John Wiley & Sons, Hoboken, NJ, 2008.

[8] K. S. Cole, R. H. Cole, Dispersion and absorption in dielectrics 1: Alternating current characteristics, J. Chem. Phys. 9 (4) (1941) 341–351.

[9] R. M. Fuoss, J. Kirkwood, Electrical properties of solids. viii. dipole moments in polyvinyl chorlide-diphenyl systems, J. Am. Chem. Soc. 63 (1941) 385–394.

[10] R. de Levie, On porous electrodes in electrolyte solutions. IV, Electrochim. Acta 9 (1964) 1231–1245.

[11] R. de Levie, Electrochemical responses of porous and rough electrodes, in: P. Delahay (Ed.), Advances in Electrochemistry and Electrochemical Engineering, Vol. 6, Interscience, New York, 1967, pp. 329–397.

[12] C. Cachet, R. Wiart, The pore texture of zinc electrodes characterized by impedance measurements, Electrochim. Acta 29 (2) (1984) 145–149.

[13] I. Frateur, C. Deslouis, M. E. Orazem, B. Tribollet, Modeling of the cast iron/drinking water system by electrochemical impedance spectroscopy, Electrochim. Acta 44 (1999) 4345–4356.

[14] R. de Levie, The influence of surface roughness of solid electrodes on electrochemical measurements, Electrochim. Acta 10 (2) (1965) 113–130.

[15] W. Scheider, Theory of the frequency dispersion of electrode polarization. topology of networs with fractional power frequency dependence, J. Phys. Chem. 79 (2) (1975) 127–136.

[16] A. L. Mehaute, G. Crepy, Introduction to transfer and motion in fractal media: The geometry of kinetics, Solid State Ionics 9-10 (1983) 17–30.

[17] L. Nyikos, T. Pajkossy, fractal dimension and fractional power frequency-dependent impedance of blocking electrodes, Electrochim. Acta 30 (11) (1985) 1533–1540.

[18] V. M.-W. Huang, V. Vivier, M. E. Orazem, N. Pébère, B. Tribollet, The apparent CPE behavior of an ideally polarized disk electrode: A global and local impedance analysis, J. Electrochem. Soc. 154 (2007) C81–C88.

[19] V. M.-W. Huang, V. Vivier, I. Frateur, M. E. Orazem, B. Tribollet, The global and local impedance response of a blocking disk electrode with local cpe behavior, J. Electrochem. Soc. 154 (2007) C89–C98.

[20] M. Keddam, H. Takenouti, Frequency-dependence of complex transfer functions at fractal interfaces- an approach based on the von koch model, Comptes Rendus De L Academie des Sciences Serie II 302 (6) (1986) 281–284.

[21] J. C. Wang, Impedance of a fractal electrolyte-electrode interface, Electrochim. Acta 33 (5) (1988) 707–711.

[22] J. B. Bates, Y. Chu, W. Stribling, Surface topography and the impedance of metal-electrolyte interfaces, Phys. Rev. Lett. 60 (7) (1988) 627–630.

[23] T. Pajkossy, Impedance of rough capacitive electrodes, J. Electroanal. Chem. 364 (1994) 111–125.

[24] R. de Levie, Fractals and rough electrodes, J. Electroanal. Chem. 281 (1990) 1–21.

[25] T. Yamamoto, Y. Yamamoto, Dielectric constant and resistivity of epidermal stratum corneum, Med. Biol. Eng. 14 (1976) 494–500.

[26] L. Young, Anodic oxide films 4: The interpretation of impedance measurements on oxide coated electrodes on niobium, Trans. Faraday Soc. 51 (1955) 1250–1260.

[27] T. Yamamoto, Y. Yamamoto, Electrical properties of the epidermal stratum corneum, Med. Biol. Eng. 14 (1976) 151–158.

[28] C. Poon, T. Choy, Frequency dispersions of human skin dielectrics, Biophys. J. 34 (1981) 135–147.

[29] M. Bojinov, G. Fabricius, T. Laitinen, T. Saario, G. Sundholm, Conduction mechanism of the anodic film on chromium in acidic sulphate solutions, Electrochim. Acta 44 (1998) 247–261.

[30] C. A. Schiller, W. Strunz, The evaluation of experimental dielectric data of barrier coatings by means of different models, Electrochim. Acta 46 (2001) 3619–3625.

[31] M. Bojinov, G. Fabricius, T. Laitinen, K. Makela, T. Saario, G. Sundhom, Coupling between ionic defect structure and electronic conduction in passive films on iron, chromium, and iron-chromium alloys, Electrochim. Acta 45 (13) (2000) 2029–2048.

[32] W. G. Pell, A. Zolfaghari, B. E. Conway, Capacitance of the double layer at polycrystalline Pt electrodes bearing a surface-oxide film, J. Electroanal. Chem. 532 (1-2) (2002) 13–23.

[33] V. D. Jović, B. M. Jović, EIS and differential capacitance measurements onto single crystal faces in different solutions: Part 1 - Ag(111) in .01 M NaCl, J. Electroanal. Chem. 541 (2003) 1–11.

[34] V. D. Jović, B. M. Jović, EIS and differential capacitance measurements onto single crystal faces in different solutions: Part 2 - Cu(111) and Cu(100) in .1 M NaOH, J. Electroanal. Chem. 541 (2003) 13–21.

[35] P. S. Germain, W. G. Pell, B. E. Conway, Evaluation and origins of the difference between double-layer capacitance behaviour at Au-metal and oxidized Au surfaces, Electrochim. Acta 49 (11) (2004) 1775–1788.

[36] M. Figueiredo, C. Gomes, R. Costa, A. Martins, C. M. Pereira, F. Silva, Differential capacity of a deep eutectic solvent based on choline chloride and glycerol on solid electrodes, Electrochim. Acta 54 (9) (2009) 2630–2634.

[37] C. Gabrielli, P. P. Grand, A. Lasia, H. Perrot, Investigation of hydrogen adsorption and absorption in palladium thin films 3: Impedance spectroscopy, J. Electrochem. Soc. 151 (11) (2004) A1943–A1949.

[38] M. H. Martin, A. Lasia, Hydrogen sorption in Pd monolayers in alkaline solution, Electrochim. Acta 54 (22) (2009) 5292–5299.

[39] L. L. Chen, A. Lasia, Study of the kinetics of hydrogen evolution reaction on nickel-zinc alloy electrodes, J. Electrochem. Soc. 138 (1991) 3321–3328.

[40] H. Dumont, P. Los, L. Brossard, A. Lasia, H. Ménard, Lanthanum phosphate-bonded composite nickel-rhodium electrodes for alkaline water electrolysis, J. Electrochem. Soc. 139 (8) (1992) 2143–2148.

[41] H. J. Miao, D. L. Piron, Composite-coating electrodes for hydrogen evolution reaction, Electrochim. Acta 38 (8) (1993) 1079–1085.

[42] N. R. Elezović, V. D. Jović, N. V. Krstajić, Kinetics of the hydrogen evolution reaction on Fe-Mo film deposited on mild steel support in alkaline solution, Electrochim. Acta 50 (28) (2005) 5594–5601.

[43] L. Vázquez-Gómez, S. Cattarin, P. Guerriero, M. Musiani, Preparation and electrochemical characterization of Ni + RuO_2 composite cathodes of large effective area, Electrochim. Acta 52 (2007) 8055–8063.

[44] S. M. A. Shibli, V. S. Dilimon, Development of TiO_2-supported nano-RuO_2-incorporated catalytic nickel coating for hydrogen evolution reaction, Int. J. Hydrogen Energy 33 (4) (2008) 1104–1111.

[45] V. A. Alves, L. A. da Silva, J. F. C. Boodts, Surface characterisation of $IrO_2/TiO_2/CeO_2$ oxide electrodes and faradaic impedance investigation of the oxygen evolution reaction from alkaline solution, Electrochim. Acta 44 (8-9) (1998) 1525–1534.

[46] R. Jurczakowski, C. Hitz, A. Lasia, Impedance of porous Au-based electrodes, J. Electroanal. Chem. 572 (2004) 355–366.

[47] J. M. Campiña, A. Martins, F. Silva, Selective permeation of a liquid-like self-assembled monolayer of 11-amino-1-undecanethiol on polycrystalline gold by highly charged electroactive probes, J. Phys. Chem. C 111 (14) (2007) 5351–5362.

[48] J. M. Campiña, A. Martins, F. Silva, Probing the organization of charged self-assembled monolayers by using the effects of pH, time, electrolyte anion, and temperature on the charge transfer of electroactive probes, J. Phys. Chem. C 113 (6) (2009) 2405–2416.

[49] T. Zalewska, A. Lisowska-Oleksiak, S. Biallozor, V. Jasulaitiene, Polypyrrole films polymerized on a nickel substrate, Electrochim. Acta 45 (24) (2000) 4031–4040.

[50] S. P. Harrington, T. M. Devine, Analysis of electrodes displaying frequency dispersion in Mott-Schottky tests, J. Electrochem. Soc. 155 (2008) C381–C386.

[51] S. P. Harrington, T. M. Devine, Relation between the semiconducting properties of a passive film and reduction reaction rates, J. Electrochem. Soc. 156 (4) (2009) C154–C159.

[52] V. D. Jović, B. M. Jović, The influence of the conditions of the ZrO_2 passive film formation on its properties in 1M NaOH, Corros. Sci. 50 (2008) 3063–3069.

[53] T. Van Schaftinghen, C. Le Pen, H. Terryn, F. Hrzenberger, Investigation of the barrier properties of silanes on cold rolled steel, Electrochim. Acta 49 (17-18) (2004) 2997–3004.

[54] M. L. Zheludkevich, R. Serra, M. F. Montemor, K. A. Yasakau, I. M. M. Salvado, M. G. S. Ferreira, Nanostructured sol-gel coatings doped with cerium nitrate as pre-treatments for AA2024-T3: Corrosion protection performance, Electrochim. Acta 51 (2) (2005) 208–217.

[55] T. Van Schaftinghen, C. Deslouis, A. Hubin, H. Terryn, Influence of the surface pre-treatment prior to the film synthesis: On the corrosion protection of iron with polypyrrole films, Electrochim. Acta 51 (8-9) (2006) 1695–1703.

[56] K. A. Yasakau, M. L. Zheludkevich, O. V. Karavai, M. G. S. Ferreira, Influence of inhibitor addition on the corrosion protection performance of solgel coatings on AA2024, Prog. Org. Coat. 63 (2008) 352–361.

[57] M. L. Zheludkevich, K. A. Yasakau, S. K. Poznyak, M. G. S. Ferreira, Triazole and thiazole derivatives as corrosion inhibitors for AA2024 aluminium alloy, Corros. Sci. 47 (2005) 3368–3383.

[58] P. Agarwal, M. E. Orazem, L. H. García-Rubio, Measurement models for electrochemical impedance spectroscopy: I. demonstration of applicability, J. Electrochem. Soc. 139 (7) (1992) 1917–1927.

[59] P. Agarwal, O. D. Crisalle, M. E. Orazem, L. H. García-Rubio, Measurement models for electrochemical impedance spectroscopy: 2. determination of the stochastic contribution to the error structure, J. Electrochem. Soc. 142 (1995) 4149–4158.

[60] P. Agarwal, M. E. Orazem, L. H. García-Rubio, Measurement models for electrochemical impedance spectroscopy: 3. evaluation of consistency with the kramers-kronig relations, J. Electrochem. Soc. 142 (1995) 4159–4168.

[61] M. E. Orazem, A systematic approach toward error structure identification for impedance spectroscopy, J. Electroanal. Chem. 572 (2004) 317–327.

[62] K. Darowicki, The amplitude analysis of impedance spectra, Electrochim. Acta 40 (4) (1995) 439–445.

[63] J. Diard, B. LeGorrec, C. Montella, Reexamination of the validity-conditions of the redox systems impedance measurements .1. reversible electron transfer, J. Chim. Phys. Phys.-Chim. Biol. 89 (1992) 2153–2167.

[64] K. Darowicki, Linearization in impedance measurments, Electrochim. Acta 42 (12) (1997) 1781–1788.

[65] G. Popkirov, R. Schindler, Effect of sample nonlinearity on the performance of time domain electrochemical impedance spectroscopy, Electrochim. Acta 40 (15) (1995) 2511–2517.

[66] J. Diard, B. LeGorrec, C. Montella, Deviation from the polarization resistance due to non-linearity i- theoretical formulation, J. Electroanal. Chem. 432 (1997) 27–39.

[67] J. Diard, B. L. Gorrec, C. Montella, Deviation of the polarization resistance due to non-linearity-i. application to electrochemical reactions, J. Electroanal. Chem. 432 (1997) 41–52.

[68] J. Diard, B. LeGorrec, C. Montella, Deviation of the polarization resistance due to non-linearity. iii-polarization resistance determination from non-linear impedance measurments, J. Electroanal. Chem. 432 (1997) 53–62.

[69] J. Diard, B. LeGorrec, C. Montella, Non-linear impedance for a two-step electrode reaction with an intermediate adsorbed species, Electrochim. Acta 42 (7) (1997) 1053–1072.

[70] R. Milocco, Electrochemical impedance spectroscopy using discrete-time model formulation, Electrochim. Acta 44 (1999) 4147–4154.

[71] E. V. Gheem, R. Pintelon, J. Vereecken, J. Schoukens, A. Hubin, P. Verboven, O. Blajiev, Electrochemical impedance spectroscopy in the presense of non-linear distortions and non-stationary behavior part i: theory and validation, Electrochim. Acta 49 (2004) 4753–4762.

[72] O. Blajiev, R. Pintelon, A. Hubin, Detection and evaluation of measurment noise and stochastic non-linear distortions in electrochemical impedance measurments by a model based on a broadband periodic excitation, J. Electroanal. Chem. 576 (2005) 65–72.

[73] D. D. Macdonald, Reflections on the history of electrochemical impedance spectroscopy, Electrochim. Acta 51 (2006) 1376–1388.

[74] M. Urquidi-Macdonald, S. Real, D. Macdonald, Applications of the kramers-kronig transforms in the analysis of electrochemical impedance data-iii. stability and linearity, Electrochim. Acta 35 (10) (1990) 1559–1566.

[75] B. Hirschorn, B. Tribollet, M. E. Orazem, On selection of the perturbation amplitude required to avoid nonlinear effects in impedance measurements, Isr. J. Chem. 48 (2008) 133–142.

[76] E. V. Gheem, R. Pintelon, J. Vereecken, J. Schoukens, A. Hubin, P. Verboven, O. Blajiev, Electrochemical impedance spectroscopy in the presence of non-linear distortions and non-stationary behavior: I. theory and validation, Electrochim. Acta 49 (2006) 4753–4762.

[77] O. Blajiev, T. Breugelmans, R. Pintelon, A. Hubin, Improvement of the impedance measurement reliability by some new experimental and data treatment procedures applied to the behavior of copper in neutral chloride solutions containing small heterocycle molecules, Electrochim. Acta 51 (8-9) (2006) 1403–1412.

[78] E. V. Gheem, R. Pintelon, A. Hubin, J. Schoukens, P. Verboven, O. Blajiev, J. Vereecken, Electrochemical impedance spectroscopy in the presence of non-linear distortions and non-stationary behavior: Ii. application to crystallographic pitting corrosion of aluminum, Electrochim. Acta 51 (2006) 1443–1452.

[79] H. Xiao, S. Lalvani, A linear model of alternating voltage-induced corrosion, J. Electrochem. Soc. 155 (2) (2008) C69–C74.

[80] C. R. Wylie, Advanced Engineering Mathematics, 3rd Edition, McGraw-Hill, New York, 1966.

[81] C. Gabrielli, M. Keddam, H. Takenouti, Electrochemical methods in corrosion research vol. 8, in: Materials Science Forum Trans. Tech Publications Switzerland, 1986, pp. 417–427.

[82] D. Kooyman, M. Sluyters-Rehbach, J. Sluyters, Linearization of the current/voltage characteristic of an electrode process. application to relaxation methods, Electrochim. Acta 11 (1966) 1197–1204.

[83] K. Darowicki, Corrosion rate measurements by non-linear electrochemical impedance spectroscopy, Corros. Sci. 37 (6) (1995) 913–925.

[84] P. Shukla, M. Orazem, O. Crisalle, Validation of the measurment model concept for error structure identification, Electrochim. Acta 49 (2004) 2881–2889.

[85] M. E. Orazem, T. E. Moustafid, C. Deslouis, B. Tribollet, The error structure of impedance spectroscopy measurements for systems with a large ohmic resistance with respect to the polarization impedance, J. Electrochem. Soc. 143 (1996) 3880–3890.

[86] M. E. Orazem, M. Durbha, C. Deslouis, H. Takenouti, B. Tribollet, Influence of surface phenomena on the impedance response of a rotating disk electrode, Electrochim. Acta 44 (1999) 4403–4412.

[87] M. E. Orazem, N. Pébère, B. Tribollet, A new look at graphical representation of impedance data, J. Electrochem. Soc. 153 (2006) B129–B136.

[88] J. S. Newman, K. E. Thomas-Alyea, Electrochemical Systems, 3rd Edition, John Wiley & Sons, New York, 2004.

[89] E. Chassaing, B. Sapoval, G. Daccord, R. Lenormand, Experimental study of the impedance of blocking quasi-fractal and rough electrodes, J. Electroanal. Chem. 279 (1-2) (1990) 67–78.

[90] E. D. Bidóia, L. O. S. Bulhões, R. C. Rocha-Filho, Pt/$HClO_4$ interface CPE: influence of surface roughness and electrolyte concentration, Electrochim. Acta 39 (5) (1994) 763–769.

[91] M. Bojinov, The ability of a surface charge approach to describe barrier film growth on tungsten in acidic solutions, Electrochim. Acta 42 (23-24) (1997) 3489–3498.

[92] M. Bojinov, Modelling the formation and growth of anodic passive films on metals in concentrated acid solutions, J. Solid State Electrochem. 1 (1997) 161–171.

[93] I. Frateur, Characterization of oxide films by electrochemical impedance, ECS Trans. 13 (13) (2008) 115–128.

[94] J. J. Randall, W. J. Bernard, R. R. Wilkinson, A radiotracer study of the composition and properties of anodic oxide films on tantalum and niobium, Electrochim. Acta 10 (2) (1965) 183–201.

[95] F. Di Quarto, S. Piazza, C. Sunseri, Amorphous semiconductor–electrolyte junction: Impedance study on the a-Nb_2O_5–electrolyte junction, Electrochim. Acta 35 (1) (1990) 99–107.

[96] M. M. Lohrengel, Thin anodic oxide layers on aluminium and other valve metals: High field regime, Mater. Sci. Eng. R11 (1993) 243–294.

[97] I. Arsova, L. Arsov, N. Hebestreit, A. Anders, W. Plieth, Electrochemical formation of anodic oxide films on nb surfaces: Ellipsometric and raman spectroscopical studies, J. Solid State Electrochem. 11 (2007) 209–214.

[98] H. Habazaki, T. Ogasawara, H. Konno, K. Shimizu, K. Asamic, K. Saito, S. Nagata, P. Skeldon, G. E. Thompson, Growth of anodic oxide films on oxygen-containing niobium, Electrochim. Acta 50 (2005) 5334–5339.

[99] A. Heidelberg, C. Rozenkranz, J. W. Schultze, T. Schäpers, G. Staikov, Localized electrochemical oxidation of thin Nb films in microscopic and nanoscopic dimensions, Surf. Sci. 597 (2005) 173–180.

[100] L. L. Langley, I. Telford, J. B. Christensen, Dynamic Anatomy and Physiology, 4th Edition, McGraw-Hill, New York, 1974.

[101] P. T. Wojcik, P. Agarwal, M. E. Orazem, A method for maintaining a constant potential variation during galvanostatic regulation of electrochemical impedance measurements, Electrochim. Acta 41 (7/8) (1996) 977–983.

[102] P. T. Wojcik, M. E. Orazem, Variable-amplitude galvanostatically modulated impedance spectroscopy as a tool for assessing reactivity at the corrosion potential without distorting the temporal evolution of the system, Corros. 54 (1998) 289–298.

[103] G. F. Odland, Structure of the skin, in: L. A. Goldsmith (Ed.), Biochemistry and Physiology of the Skin, Oxford University Press, New York, 1991, Ch. 1, pp. 3–62.

[104] L. Young, Anodic Oxide Films, Academic Press, New York, 1961.

[105] Y. N. Kalia, F. Pirot, R. H. Guy, Homogeneous transport in a heterogeneous membrane: Water diffusion across human stratum corneum in vivo, Biophys. J. 71 (1996) 2692–2700.

[106] H. Göhr, Contributions of single electrode processes to the impedance, Ber. Bunsen Ges. Phys. Chem. 85 (1981) 274–280.

[107] H. Göhr, J. Schaller, C. A. Schiller, Impedance studies of the oxide layer on zircaloy after previous oxidation in water vapor at 400°C, Electrochim. Acta 38 (14) (1993) 1961–1964.

[108] U. Pliquett, R. Langer, J. C. Weaver, Changes in the passive electrical properties of human stratum corneum due to electroporation, Biochim. Biophys. Acta 1239 (2) (1995) 111 – 121.

[109] S. Y. Oh, L. Lyung, D. Bommannan, R. H. Guy, R. O. Potts, Effect of current, ionic strength and temperature on the electrical properties of skin, J. Controlled Release 27 (27) (1993) 115–125.

[110] M. E. Orazem, P. K. Shukla, M. A. Membrino, Extension of the measurement model approach for deconvolution of underlying distributions for impedance measurements, Electrochim. Acta 47 (2002) 2027–2034.

[111] B. Hirschorn, M. E. Orazem, B. Tribollet, V. Vivier, I. Frateur, M. Musiani, Determination of effective capacitance and film thickness from cpe parameters, Electrochim. Acta (2010) in press.

[112] I. Frateur, L. Lartundo-Rojas, C. Methivier, A. Galtayries, P. Marus, Influence of bovine serum albumin in sulphuric acid aqueous solution on the corrosion and the passivation of an iron-chromium alloy, Electrochim. Acta 51 (2006) 1550–1557.

[113] M. E. Orazem, P. T. Wojcik, M. Durbha, I. Frateur, L. H. García-Rubio, Application of measurement models for interpretation of impedance spectra for corrosion, Mater. Sci. Forum 289-292 (1998) 813–828.

BIOGRAPHICAL SKETCH

Bryan Hirschorn was born in 1981 in Rockville, Connecticut. He grew up in Storrs, Connecticut and graduated from E.O. High School in 1999. He earned his B.S. in chemical engineering from the University of Connecticut in 2003. Upon his graduation, he worked as a research and development engineer for Saint-Gobain Corporation in Northboro, Massachusetts. In 2006, Bryan enrolled at the University of Florida to pursue his doctorate in chemical engineering. During his time at the University of Florida, Bryan was married to Erin Weeden in 2007, whom he met at Squam Lake. In 2008, they welcomed their first child, Sienna Catherine Hirschorn, into the world. Bryan's hobbies include basketball, soccer, golf, boating, and water-sports.